

WL-TR-94-4039



**CONTROL OF POLYIMIDE CONDENSATION
COMPOSITE PROCESSING**

John L. Kardos
Milorad P. Dudukovic
Babu Joseph
Jiri L. Vasat
D.H. Kim
F. Wang-Hanratty

Washington University
Department of Chemical Engineering and
Materials Research Laboratory
One Brookings Dr
St Louis MO 63130

March 1994

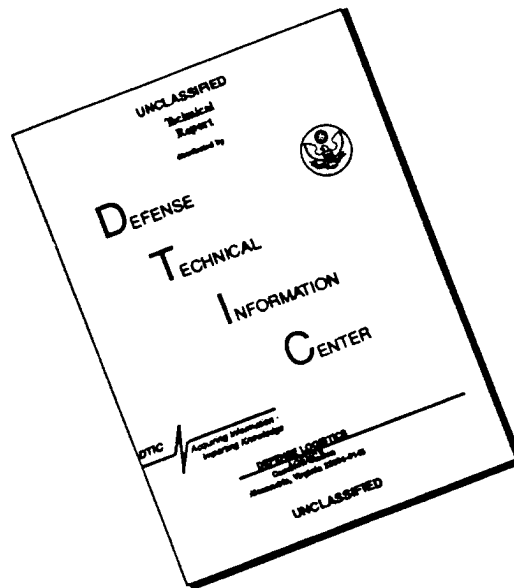
Final Report for Period 1 February 1989 to 30 September 1993

Approved for public release; distribution is unlimited.

MATERIALS DIRECTORATE
WRIGHT LABORATORY
AIR FORCE MATERIEL COMMAND
WRIGHT-PATTERSON AIR FORCE BASE OHIO 45433-7734

19960415 105

DISCLAIMER NOTICE

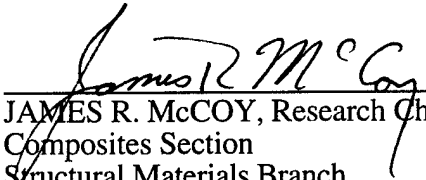


THIS DOCUMENT IS BEST QUALITY AVAILABLE. THE COPY FURNISHED TO DTIC CONTAINED A SIGNIFICANT NUMBER OF PAGES WHICH DO NOT REPRODUCE LEGIBLY.

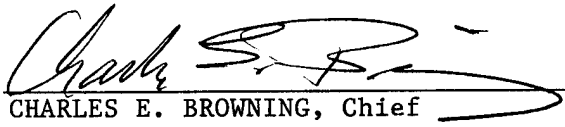
NOTICE

When government drawings, specifications, or other data are used for any purpose other than in connection with a definitely related government procurement operation, the United States Government thereby incurs no responsibility nor any obligation whatsoever; and the fact that the government may have formulated, furnished, or in any way supplied the said drawings, specifications, or other data, is not to be regarded by implication or otherwise as in any manner licensing the holder or any other person or corporation, or conveying any rights or permission to manufacture, use, or sell any patented invention that may in any way be related thereto.

This technical report has been reviewed and is approved for publication.


JAMES R. McCOY, Research Chemist
Composites Section
Structural Materials Branch


L. SCOTT THEIBERT, Chief
Structural Materials Branch
Nonmetallic Materials Division


CHARLES E. BROWNING, Chief
Nonmetallic Materials Division
Materials Directorate

If your address has changed, if you wish to be removed from our mailing list, or if the addressee is no longer employed by your organization, please notify WL/MLBC, Bldg 654, 2941 P St, Ste 1, Wright-Patterson AFB OH 45433-7750 to help maintain a current mailing list.

Copies of this report should not be returned unless return is required by security considerations, contractual obligations, or notice on a specific document.

REPORT DOCUMENTATION PAGE			Form Approved OMB No. 0704-0188	
Public reporting burden for this collection of information is estimated to average 1 hour per response, including the time for reviewing instructions, searching existing data sources, gathering and maintaining the data needed, and completing and reviewing the collection of information. Send comments regarding this burden estimate or any other aspect of this collection of information, including suggestions for reducing this burden, to Washington Headquarters Services, Directorate for Information Operations and Reports, 1215 Jefferson Davis Highway, Suite 1204, Arlington, VA 22202-4302, and to the Office of Management and Budget, Paperwork Reduction Project (0704-0188), Washington, DC 20503.				
1. AGENCY USE ONLY (Leave blank)	2. REPORT DATE March 1994	3. REPORT TYPE AND DATES COVERED Final Report for 1 February 1989 to 30 September 1993		
4. TITLE AND SUBTITLE Control of Polyimide Condensation Composite Processing		5. FUNDING NUMBERS Contract: F33615-88-C-5455 PE: 78011F PR: 2865 TA: 10 WU: 11		
6. AUTHOR(S) John L. Kardos, Milorad P. Dudukovic, Babu Joseph, Jiri L. Vasat, D.H. Kim, F. Wang-Hanratty		8. PERFORMING ORGANIZATION REPORT NUMBER		
7. PERFORMING ORGANIZATION NAME(S) AND ADDRESS(ES) Washington University Department of Chemical engineering and materials Research Laboratory One Brookings Dr St Louis MO 63130		10. SPONSORING / MONITORING AGENCY REPORT NUMBER WL-TR-94-4039		
9. SPONSORING / MONITORING AGENCY NAME(S) AND ADDRESS(ES) Materials Directorate Wright Laboratory Air Force Materiel Command Wright-Patterson AFB OH 45433-7734		11. SUPPLEMENTARY NOTES This report is Volume 2; WL-TR-94-4020 is Volume 1		
12a. DISTRIBUTION / AVAILABILITY STATEMENT Approved for public release; distribution is unlimited.		12b. DISTRIBUTION CODE		
13. ABSTRACT (Maximum 200 words) AFR700B is a high temperature polyimide resin having the advantages of a high glass transition temperature (750°F) and superior thermo-oxidative stability, but the disadvantage of a volatile management problem. This study explored a new process simulation model, new sensing technology, and new concepts in process control in order to advance the state of processing science and to make the processing of AFR700B composite parts cost effective. The new devolatilization model was experimentally verified by comparing its predictions for pressure and temperature distribution through the laminate thickness with experimentally measured pressure and temperature profiles. The verified model was used to successfully predict the concentration and rate of removal of volatiles during composite cure for several heating rates and vacuum bag pressures. Comparison of measured dielectric ionic viscosity and devolatilization model prediction for volatile mass fluxes during processing shows that microdielectrometry can indicate (a) the start of polycondensation reaction, (b) the temperature-time window in which maximum devolatilization occurs and voids develop between laminate plies, (c) the end of the polycondensation reaction, and (d) the effects of water absorbed during freezer storage on the polyimidization reaction and devolatilization process. Artificial neural network models proved superior to classical graduiatic regression approaches in capturing the non-linear relationships that exist between product quality and processing variables. Intermediate secondary measurements, taken while the cure cycle is in progress, can be used to detect unmeasured disturbances; hence, providing some feedback correction to the on-line model used.				
14. SUBJECT TERMS AFR700B, polyimide, composite processing, expert system, process control, process monitoring, sensors, intelligent processing, QPA		15. NUMBER OF PAGES 110		
17. SECURITY CLASSIFICATION OF REPORT UNCLASSIFIED		16. PRICE CODE		
18. SECURITY CLASSIFICATION OF THIS PAGE UNCLASSIFIED	19. SECURITY CLASSIFICATION OF ABSTRACT UNCLASSIFIED	20. LIMITATION OF ABSTRACT SAR		

TABLE OF CONTENTS

1.0	INTRODUCTION AND TECHNICAL APPROACH.....	1-1
2.0	BACKGROUND.....	2-1
2.1	Polyimide Chemistry and Prepreg Rheology.....	2-1
2.2	Model Development History.....	2-6
2.3	Devolatilization Model.....	2-7
2.3.1	Energy Equation.....	2-8
2.3.2	Mass Balance on the Liquid Phase.....	2-9
2.3.3	Gas Phase Mass Balance.....	2-10
2.3.4	Mass Balance on Active Groups in the Liquid.....	2-10
2.3.5	Mass Balance on Side Products ($i = 1, 2$).....	2-10
2.3.6	Mass Balance on Solvent ($i = 3$).....	2-11
2.3.7	Gas Molar Fraction Equations ($i = 1, 2, 3$).....	2-11
3.0	SENSOR SELECTION.....	3-1
3.1	Types of Sensors.....	3-1
3.1.1	Pressure.....	3-1
3.1.2	Temperature.....	3-1
3.1.3	Resin State Sensor.....	3-1
3.2	Miniclave Apparatus.....	3-2
4.0	DETERMINATION OF MODEL INPUT PARAMETERS.....	4-1
4.1	Resin Characterization.....	4-1
4.1.1	DSC Measurements.....	4-1
4.1.2	Thermogravimetric Measurements.....	4-5
4.1.3	Optical Microscopy Study of Neat Resin.....	4-5
4.1.4	Optical Microscopy Study of Laminate Surfaces.....	4-8
4.2	Polymer Reaction Kinetics Model.....	4-11
4.3	Mass Transfer Rates of Volatiles between Liquid and Gas Phases.....	4-15
4.4	Gas Phase Permeability Characterization.....	4-21
5.0	MODEL VERIFICATION.....	5-1
5.1	Gas Pressure Measurements.....	5-1
5.2	Temperature Measurements.....	5-6
6.0	EFFECT OF PROCESS VARIABLES ON DEVOLATILIZATION.....	6-1
6.1	Ionic Viscosity as a Measure of Devolatilization.....	6-1
6.1.1	Imidization Reaction Characterization.....	6-4
6.1.2	Bubble Formation During Devolatilization.....	6-5

6.2	Effect of Process Parameters on Ionic Viscosity	6-6
6.3	Moisture Effects on Ionic Viscosity	6-10
7.0	SIMULATION OF PROPOSED INDUSTRIAL CYCLES	7-1
7.1	Comparison of Process Simulations and Real-Time Dielectric Sensor Data.....	7-1
8.0	CONTROL RULES AND STRATEGIES	8-1
8.1	Model-Based Control of Voids and Laminate Thickness During Autoclave Curing of Carbon/Epoxy Composite Laminates	8-1
8.1.1	Background	8-1
8.1.2	Data Driven Models for Process Control	8-4
8.1.3	On-Line ANN Models	8-10
8.1.4	Control Using ANN Models: Neurocontrol	8-12
8.1.5	Some Results.....	8-14
8.1.5.1	Performance with Measured Disturbances	8-14
8.1.5.2	Performance in the Presence of Unmeasured Disturbances	8-18
9.0	SUMMARY AND CONCLUSIONS	9-1
10.0	ACKNOWLEDGEMENT	10-1
11.0	REFERENCES	11-1
12.0	APPENDIX: MODEL INPUT FILE	12-1

LIST OF FIGURES

- Figure 1.1 Program Schedule
- Figure 2.1a. AFR-700B Polyimide Resin Chemistry.
- Figure 2.1b. PMR-15 Polyimide Resin Chemistry.
- Figure 2.2. Dynamic Modulus Measurement of AFR-700B/S-2 Glass Fiber Prepreg.
- Figure 2.3. Schematic Depiction of the Devolatilization Process in Composite Laminates.
- Figure 3.1. Schematic of Miniclave Apparatus.
- Figure 4.1. DSC Measurement at 2°C/min. Heating Rate for AFR-700B Neat Resin.
- Figure 4.2. DSC Measurement at 5°C/min. Heating Rate for AFR-700B Neat Resin.
- Figure 4.3. DSC Measurement at 10°C/min. Heating Rate for AFR-700B Neat Resin.
- Figure 4.4. DSC Measurement at 2°C/min. Heating Rate for AFR-700B Dry Neat Resin.
- Figure 4.5. DSC Measurement at 2°C/min. Heating Rate for AFR-700B Polyimide Oligomer.
- Figure 4.6. Experimental Results for the Weight Loss from a 3-ply, Unidirectional Laminate of AFR-700B/S-2 Glass Fiber as a Function of Temperature at 2°C/min. Heating Rate and Pressures of 760 and 20 Torr.
- Figure 4.7. Optical Micrograph of the AFR-700B Neat Resin at 50°C (320 times Magnification, Transmitted Polarized Light).
- Figure 4.8. Optical Micrograph of the AFR-700B Neat Resin at 90°C (320 times Magnification, Transmitted Polarized Light).
- Figure 4.9. Optical Micrograph of the AFR-700B Neat Resin at 200°C (320 times Magnification, Transmitted Polarized Light).

- Figure 4.10. Optical Micrograph of the AFR-700B Neat Resin at 250°C (320 times Magnification, Transmitted Polarized Light).
- Figure 4.11. Optical Micrograph of the AFR-700B/S-2 Glass Laminate at Room Temperature (35 times Magnification, Incident Light).
- Figure 4.12. Optical Micrograph of Bubbles Developing on Laminate Sample Surface at 90°C (35 times Magnification, Incident Light).
- Figure 4.13. Optical Micrograph of Bubbles Growing on Laminate Sample Surface at 110°C (35 times Magnification, Incident Light).
- Figure 4.14. Optical Micrograph of the Dry Laminate Resin at 170°C (35 times Magnification, Incident Light).
- Figure 4.15. Magnified Endothermic Peak from DSC Measurement at 2°C/min. Heating Rate for AFR-700B Dry Neat Resin.
- Figure 4.16. Regression Analysis of Experimental DSC Data for Heating Rates of 2°C, 5°C and 10°C/min. at Atmospheric Pressure.
- Figure 4.17. Sample Preparation Technique for Weight Loss Experiments.
- Figure 4.18. Experimental and Calculated Results for Cumulative Mass Fluxes from a 3-ply, Unidirectional AFR-700B/S-2 Laminate as a Function of Time (Temperature) at 0.5°C/min. Heating Rate and 20 Torr Pressure.
- Figure 4.19. Experimental and Calculated Results for Cumulative Mass Fluxes from a 3-ply, Unidirectional AFR-700B/S-2 Laminate as a Function of Time (Temperature) at 0.5°C/min. Heating Rate and 50 Torr Pressure.
- Figure 4.20. Experimental and Calculated Results for Cumulative Mass Fluxes from a 3-ply, Unidirectional AFR-700B/S-2 Laminate as a Function of Time (Temperature) at 2°C/min. Heating Rate and 20 Torr Pressure.
- Figure 4.21. Experimental and Calculated Results for Cumulative Mass Fluxes from a 3-ply, Unidirectional AFR-700B/S-2 Laminate as a Function of Time (Temperature) at 2°C/min. Heating Rate and 50 Torr Torr Pressure.

- Figure 4.22. Experimental and Calculated Results for Cumulative Mass Fluxes from a 3-ply, Unidirectional AFR-700B/S-2 Laminate as a Function of Time (Temperature) at 4°C/min. Heating Rate and 20 Torr Pressure.
- Figure 4.23. Experimental and Calculated Results for Cumulative Mass Fluxes from a 3-ply, Unidirectional AFR-700B/S-2 Laminate as a Function of Time (Temperature) at 4°C/min. Heating Rate and 50 Torr Pressure.
- Figure 4.24. Experimental and Calculated Results for Cumulative Mass Fluxes from a 3-ply, Unidirectional AFR-700B/S-2 Laminate as a Function of Time at 2°C/min. Heating Rate, 50 Torr Pressure and Steel Wool Bleeder on the Top.
- Figure 4.25. Experimental and Calculated Results for Cumulative Mass Fluxes from a 3-ply, Unidirectional AFR-700B/S-2 Laminate as a Function of Time at 4°C/min. Heating Rate, 20 Torr Pressure and Steel Wool Bleeder on the Top.
- Figure 4.26. Schematic of the Mounting of Pressure Sensor and Laminate in Miniclave. Pressure Sensor is Shown Mounted at the Bleeder Side (Top) of the Laminate.
- Figure 4.27. Measured Pressure Profiles as a Function of Temperature at a Point Midway Between the Tool Surface and the Laminate Thickness Midpoint at the Laminate Center for a 15-ply, Unidirectional AFR-700B/S-2 Laminate at 0.5°C/min. Heating Rate and Pressures of 20 and 50 Torr.
- Figure 4.28. Measured Pressure Profiles as a Function of Temperature (Time) at a Point Midway Between the Tool Surface and the Laminate Thickness Midpoint for a 15-ply, Unidirectional AFR-700B/S-2 Laminate at 1°C/min. Heating Rate and Pressures of 20 and 50 Torr.
- Figure 4.29. Measured Pressure Profiles as a Function of Temperature at a Point Midway Between the Tool Surface and the Laminate Thickness Midpoint at the Laminate Center for a 15-ply, Unidirectional AFR-700B/S-2 Laminate at 2°C/min. Heating Rate and Pressures of 20 and 50 Torr.
- Figure 4.30. Calculated Pressure Profiles as a Function of Temperature (Time) at a Point Midway Between the Tool Surface and the Laminate Thickness Midpoint

for a 15-ply, Unidirectional AFR-700B/S-2 Laminate at 0.5°C/min. Heating Rate and Pressures of 20 and 50 Torr.

Figure 4.31. Calculated Pressure Profiles as a Function of Temperature (Time) at a Point Midway Between the Tool Surface and the Laminate Thickness Midpoint for a 15-ply, Unidirectional AFR-700B/S-2 Laminate at 1°C/min. Heating Rate and Pressures of 20 and 50 Torr.

Figure 4.32. Calculated Pressure Profiles as a Function of Temperature (Time) for a 15-ply, Unidirectional AFR-700B/S-2 Laminate at a Point Midway Between the Tool Surface and the Laminate Thickness Midpoint at 2°C/min. Heating Rate and Pressures of 20 and 50 Torr.

Figure 5.1. Calculated Pressure Distribution Profiles Through the Laminate Thickness as a Function of Time (Temperature) for a 15-ply, Unidirectional AFR-700B/S-2 Laminate at 1°C/min. Heating Rate and Pressure of 20 Torr.

Figure 5.2. Calculated Pressure Distribution Profiles Through the Laminate Thickness as a Function of Time (Temperature) for a 15-ply, Unidirectional AFR-700B/S-2 Laminate at 2°C/min. Heating Rate and Pressure of 20 Torr.

Figure 5.3. Calculated Pressure Distribution Profiles Through the Laminate Thickness as a Function of Time (Temperature) for a 29-ply, Unidirectional AFR-700B/S-2 Laminate at 1°C/min. Heating Rate and Pressure of 20 Torr.

Figure 5.4. Calculated Pressure Distribution Profiles Through the Laminate Thickness as a Function of Temperature for a 29-ply, Unidirectional AFR-700B/S-2 Laminate at 2°C/min. Heating Rate and Pressure of 20 Torr.

Figure 5.5. Measured Pressure Distribution Profiles Through the Laminate Thickness as a Function of Temperature for a 15-ply, Unidirectional AFR-700B/S-2 Laminate at 1°C/min. Heating Rate and Pressure of 20 Torr.

Figure 5.6. Measured Pressure Distribution Profiles Through the Laminate Thickness as a Function of Temperature for a 15-ply, Unidirectional AFR-700B/S-2 Laminate at 2°C/min. Heating Rate and Pressure of 20 Torr.

- Figure 5.7. Measured Pressure Distribution Profiles Through the Laminate Thickness as a Function of Temperature for a 29-ply, Unidirectional AFR-700B/S-2 Laminate at 1°C/min. Heating Rate and Pressure of 20 Torr.
- Figure 5.8. Measured Pressure Distribution Profiles Through the Laminate Thickness as a Function of Temperature for a 29-ply, Unidirectional AFR-700B/S-2 Laminate at 2°C/min. Heating Rate and Pressure of 20 Torr.
- Figure 5.9. Measured Temperature Distribution Profiles Through the Laminate Thickness as a Function of Time for a 15-ply, Unidirectional AFR-700B/S-2 Laminate at 1°C/min. Heating Rate and Pressure of 20 Torr.
- Figure 5.10. Measured Temperature Distribution Profiles Through the Laminate Thickness as a Function of Time for a 15-ply, Unidirectional AFR-700B/S-2 Laminate at 2°C/min. Heating Rate and Pressure of 20 Torr.
- Figure 5.11. Measured Temperature Distribution Profiles Through the Laminate Thickness as a Function of Time for a 29-ply, Unidirectional AFR-700B/S-2 Laminate at 1°C/min. Heating Rate and Pressure of 20 Torr.
- Figure 5.12. Measured Temperature Distribution Profiles Through the Laminate Thickness as a Function of Time for a 29-ply, Unidirectional AFR-700B/S-2 Laminate at 2°C/min. Heating Rate and Pressure of 20 Torr.
- Figure 5.13. Calculated Temperature Distribution Profiles Through the Laminate Thickness as a Function of Time for a 15-ply, Unidirectional AFR-700B/S-2 Laminate at 1°C/min. Heating Rate and Pressure of 20 Torr.
- Figure 5.14. Calculated Temperature Distribution Profiles Through the Laminate Thickness as a Function of Time for a 15-ply, Unidirectional AFR-700B/S-2 Laminate at 2°C/min. Heating Rate and Pressure of 20 Torr.
- Figure 5.15. Calculated Temperature Distribution Profiles Through the Laminate Thickness as a Function of Time for a 29-ply, Unidirectional AFR-700B/S-2 Laminate at 1°C/min. Heating Rate and Pressure of 20 Torr.
- Figure 5.16. Calculated Temperature Distribution Profiles Through the Laminate Thickness as a Function of Time for a 29-ply, Unidirectional AFR-700B/S-2 Laminate at 2°C/min. Heating Rate and Pressure of 20 Torr.

- Figure 6.1. Measured Effect of Pressure (20, 50 and 760 Torr) on the Ionic Viscosity-Time (Temperature) Profiles for a 6-ply, Unidirectional AFR-700B/S-2 Laminate at 1°C/min Heating Rate.
- Figure 6.2. Calculated Effect of Pressure (20, 50 and 760 Torr) on the Concentrations of Volatile Species in the Liquid Phase as a Function of Time (Temperature) for a 6-ply, Unidirectional AFR-700B/S-2 Laminate at 1°C/min Heating Rate.
- Figure 6.3. Calculated Effect of Pressure (20, 50 and 760 Torr) on the Individual Instantaneous Volatile Mass Fluxes as a Function of Time (Temperature) for a 6-ply, Unidirectional AFR-700B/S-2 Laminate at 1°C/min Heating Rate.
- Figure 6.4. Measured Effect of Pressure (20, 50 and 760 Torr) on the Ionic Viscosity-Time (Temperature) Profiles for a 6-ply, Unidirectional AFR-700B/S-2 Laminate at 2°C/min Heating Rate.
- Figure 6.5. Measured Effect of Pressure (20, 50 and 760 Torr) on the Ionic Viscosity-Time (Temperature) Profiles for a 6-ply, Unidirectional AFR-700B/S-2 Laminate at 4°C/min Heating Rate..
- Figure 6.6. Calculated Effect of Pressure (20, 50 and 760 Torr) on the Individual Instantaneous Volatile Mass Fluxes as a Function of Time (Temperature) for a 6-ply, Unidirectional AFR-700B/S-2 Laminate at 2°C/min Heating Rate.
- Figure 6.7. Calculated Effect of Pressure (20, 50 and 760 Torr) on the Individual Instantaneous Volatile Mass Fluxes as a Function of Time (Temperature) for a 6-ply, Unidirectional AFR-700B/S-2 Laminate at 4°C/min Heating Rate.
- Figure 6.8. Calculated Effect of Pressure (20, 50 and 760 Torr) on the Concentrations of Volatile Species in the Liquid Phase as a Function of Time (Temperature) for a 6-ply, Unidirectional AFR-700B/S-2 Laminate at 2°C/min Heating Rate.
- Figure 6.9. Calculated Effect of Pressure (20, 50 and 760 Torr) on the Concentrations of Volatile Species in the Liquid Phase as a Function of Time (Temperature) for a 6-ply, Unidirectional AFR-700B/S-2 Laminate at 4°C/min Heating Rate.

- Figure 6.10. Measured Effect of Pressure (20 and 760 Torr) and Absorbed Water on the Ionic Viscosity-Time (Temperature) Profiles for a 6-ply, Unidirectional AFR-700B/S-2 Laminate at 1°C/min Heating Rate.
- Figure 6.11. Calculated Effect of 0.5 wt% of Absorbed Water on the Concentration of Volatile Species in the Liquid Phase as a Function of Time (Temperature) for a 6-ply, Unidirectional AFR-700B/S-2 Laminate at 1°C/min. Heating Rate and Pressures of 20 and 760 Torr.
- Figure 6.12. Calculated Effect of 0.5 wt% of Absorbed Water on the Individual Instantaneous Volatile Mass Fluxes as a Function of Time (Temperature) for a 6-ply, Unidirectional AFR-700B/S-2 Laminate at 1°C/min. Heating Rate and Pressures of 20 and 760 Torr.
- Figure 6.13. Measured Effect of Pressure (20 and 60 Torr) and Absorbed Water on the Ionic Viscosity-Time (Temperature) Profiles for a 6-ply, Unidirectional AFR-700B/S-2 Laminate at 2°C/min Heating Rate.
- Figure 6.14. Measured Effect of Pressure (20 and 60 Torr) and Absorbed Water on the Ionic Viscosity-Time (Temperature) Profiles for a 6-ply, Unidirectional AFR-700B/S-2 Laminate at 4°C/min Heating Rate.
- Figure 6.15. Calculated Effect of 0.5 wt% of Absorbed Water on the Individual Instantaneous Volatile Mass Fluxes as a Function of Time (Temperature) for a 6-ply, Unidirectional AFR-700B/S-2 Laminate at 2°C/min. Heating Rate and Pressures of 20 and 760 Torr.
- Figure 6.16. Calculated Effect of 0.5 wt% of Absorbed Water on the Individual Instantaneous Volatile Mass fluxes as a Function of Time (Temperature) for a 6-ply, Unidirectional AFR-700B/S-2 Laminate at 4°C/min. Heating Rate and Pressures of 20 and 760 Torr.
- Figure 7.1. Measured Dielectric, Temperature and Pressure Sensor Responses Together with Model Calculations for Individual Volatile Mass Fluxes for an 8-ply, Unidirectional AFR-700B/T650-42 Carbon Laminate Cured by Air Force Extended Cure Cycle [53].
- Figure 7.2. Measured Dielectric, Temperature and Pressure Responses Together with Model Calculation for Individual Volatile Mass Fluxes for a 16-ply,

Unidirectional AFR/T650-42 Carbon Laminate Cured by QPA Controlled Cure Cycle [52].

- Figure 8.1. A Typical Cure Cycle.
- Figure 8.2. A Perceptron Which is the Building Block of a Neural Network.
- Figure 8.3. A Three Layer Perceptron.
- Figure 8.4. The On-line Neural Network Model.
- Figure 8.5. Schematic of the On-line Neurocontroller.
- Figure 8.6. Comparison of Product Thickness for Process Cycles With and Without the Neurocontroller.
- Figure 8.7. Comparison of Maximum Void Size With and Without the Neurocontroller.
- Figure 8.8. Comparison of Cure Cycles Used by the Standard Cure Cycle and the Neurocontroller.
- Figure 8.9. Comparison of Standard Cure Cycle with On-Line Neurocontroller for Void Size Minimization. Ten Runs are Shown for Which an Unmeasured Disturbance of 20% Additional Heat Input is Accommodated.
- Figure 8.10. Changes in Cure Cycle Made by the Neurocontroller as the Cure Progresses for Case 6 of the Ten Cases of Added Heat Input.

LIST OF TABLES

Table 8.1. Typical Data Record Used in Regression.

Table 8.2. Results of the Regression Study.

1.0 INTRODUCTION AND TECHNICAL APPROACH

The scope of the "Advanced Composite Processing Technology Development" program was expanded to include condensation curing polyimide composites on 22 April 1991. This work followed a development path similar to the epoxy and bismale imide materials; however, it included an extensive material characterization and process modeling effort for the AFR-700B resin system.

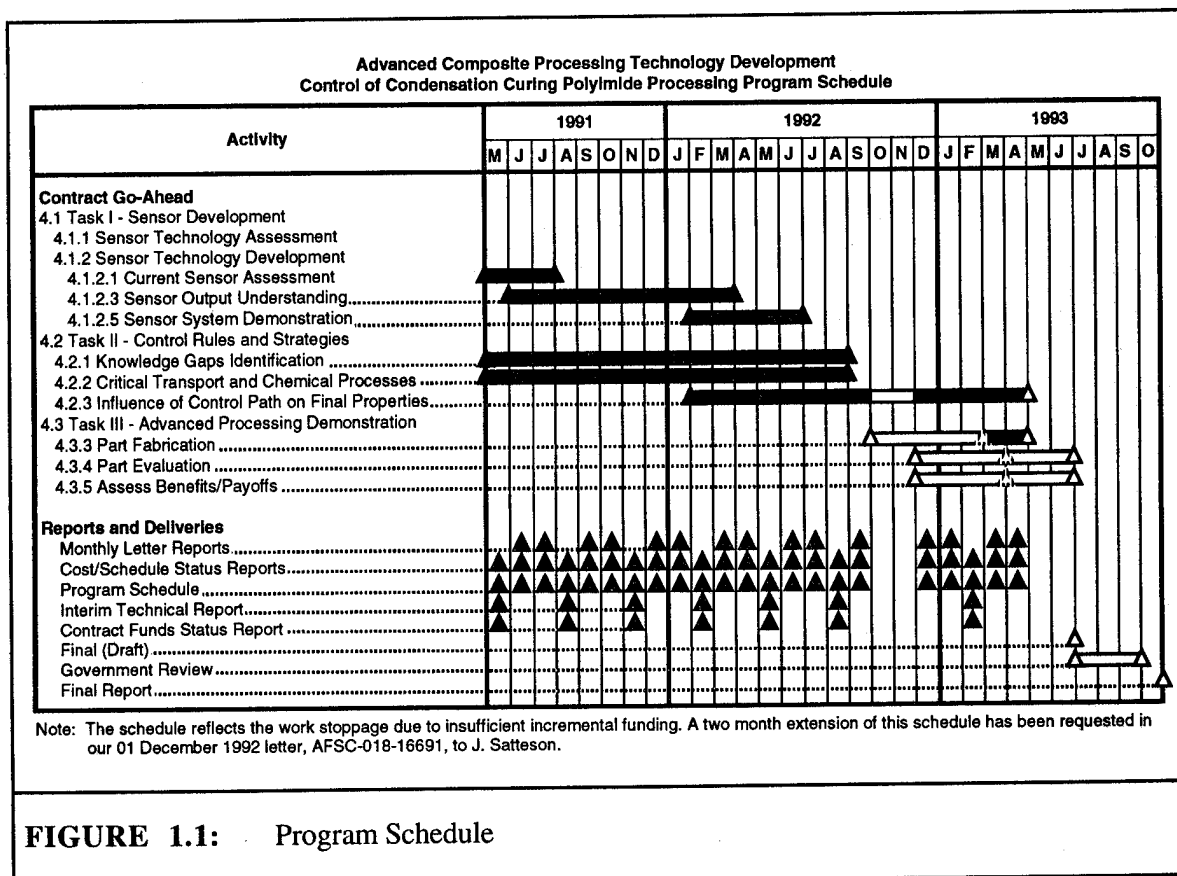
The effort was divided into three tasks. In Task I, appropriate available sensor systems were selected and evaluated for monitoring the polyimide polymerization process. These sensor systems were then combined with an experimental miniclave apparatus constructed to evaluate the sensors and verify both model input parameters and the model predictions. In Task II, the available data on the two new resin systems were gathered. Obvious gaps in the knowledge base, which are required for the control system, were identified and characterization undertaken to plug them. The modified knowledge base was incorporated into the current Washington University polyimide volatile management simulator, the simulation model was modified, and several potential processing cycles evaluated. A qualitative, rule-based strategy for control of condensation polyimide composite systems was evaluated. The critical variables to be controlled were identified and the process stages at which these variables were important were experimentally verified. In Task III, a qualitative process automation language was adapted and the technology developed in Tasks I and II verified by using it to control autoclave cycles which produced representative polyimide composite structural parts. In addition, an artificial neural net model-based controller methodology was developed, which was demonstrated on a standard epoxy/carbon system (because of time insufficiency) after the polyimide model was verified and shown to be sufficiently robust.

The Task I and Task II work, along with a small portion of Task III, was carried out by Washington University's Materials Research Laboratory. The principal investigator was Dr. J. L. Kardos with Dr. B. Joseph and Dr. M. P. Duduković as co-investigators. McDonnell Douglas Aerospace Company oversaw Washington University's efforts as well as performed most of Task III. The program schedule is shown in Figure 1-1.

It is no longer a question of whether advanced composites will be used, but rather how to manufacture them more cost-effectively so that they will be used in high volume. While simulation models are a great help in developing proper processing cycles and reducing manufacturing cost, they cannot by themselves reduce manufacturing variability. These models must be streamlined to the point where they can be used to control and optimize the process on line. This requires

adequate sensing technology as well as new concepts in artificial intelligence and knowledge-based control [1].

Continuous fiber thermoset composites made mainly from epoxies have been used extensively for aerospace applications. But their limited toughness, sensitivity to moisture and solvent, led to development of high temperature polyimide composites such as PMR-15 and Avimid K-III. However, toxicity of one of the resin monomers in PMR-15 resin, the presence of a high boiling solvent and a toxic amine in the case of Avimid K-III, as well as the requirement of long term 700°F 100-hour temperature capability of the composite led to the development of AFR-700B high temperature polyimide resin. This relatively newly formulated polyimide methodology combines autoclave processability together with a high glass transition temperature ($T_g = 750^\circ F$) and superior thermo-oxidative stability [2].



2.0 BACKGROUND

2.1 Polyimide Chemistry and Prepreg Rheology

The chemistry of the AFR-700B polyimide system begins with conversion of hexafluorodianhydride (6-FDA) into 6-FDA dimethylester (6-FDE) and conversion of endcapping crosslinker norbornenedicarboxylic anhydride (NA) into norbornene-dicarboxylic acid monomethyl ester (NE). These conversions occur when the anhydrides are dissolved in a methanol-isopropanol solution, or more recently, only methanol. Para-phenylenediamine (PPDA) is then added to the solution (Figure 2.1). The alcohol solution of monomers (termed a "masking" solvent) prevents premature formation of polyamic acids at ambient temperature and yields a viscosity low enough for the impregnation of fibers during prepreg production. The mixture of the three monomeric reactants (6-FDE/NE/PPDA) contains a specific stoichiometric molar ratio (8:1:9). With increasing temperature the bifunctional monomers react to form polyamic acid oligomer followed by polyimide oligomer, releasing solvent and water respectively in their condensation reaction. Imidization yields an oligomer with formulated molecular weight of 4382, low enough to allow release of condensation by-product from the polymer. For every mole of 4382 molecular weight polyimide formed, 17 moles of methanol and 17 moles of water are produced. Figure 2.1b shows the PMR-15 resin chemistry for comparison.

A number of researchers reported the presence of anhydride intermediates during the polymerization of PMR-15 polyimide resin. All used infrared (IR) spectroscopy to monitor the imidization reaction. The interpretation of IR data is, however, far from straightforward. Both chemical and morphological effects interfere with quantitation of data obtained from observed changes in several imide bands [3]. The simplest explanation for anhydride intermediate formation is a reverse reaction of the acid esters to form cyclic anhydrides and solvent during the initial heating. Solvent appears to act as a masking agent of the highly reactive anhydrides, thus preventing premature formation of polyamic acids at ambient temperature [4-5]. Other work proposed scission of the polyamic acids already formed from acid esters to a smaller anhydride and amine end-capped chains [6]. The third proposed possibility, which is difficult to verify experimentally, is the formation of an open chain anhydride by condensation between the carboxylic acid groups of two different chains [7]. In addition to the anhydride formation a number of other possible side-products have been reported for PMR-15 polyimide resin. These include the formation of isoimides and open-chain (acyclic) imides [8]. The presence of the open chain imides is very difficult to verify experimentally and isoimides seem more likely to develop during chemical imidization. Due to these competing reactions, the ideal polyimidization

stoichiometry of the PMR-15 polyimide resin is not achieved, and variations in prepolymer molecular weight and molecular weight distribution are observed (9). The right prepolymer molecular weight and weight distribution seem to be critical for obtaining the flow necessary for successful autoclave processing of the PMR-15 laminates (9). This is because the decrease in prepolymer molecular weight and the broad molecular weight distribution reduce the resin viscosity and increase the width of the softening region during the polymerization [9]. The amidization and imidization of PMR-15 resin do not proceed in separate reaction steps during the cure but rather do overlap [8,10].

The next step in the processing of AFR-700B polyimide is crosslinking via the nadic endcap and amino moiety at elevated temperatures (Figure 2.1). Crosslinking due to the nadic endcap proceeds by reverse Diels-Alder reaction, yielding cyclopentadiene which recombines by an addition reaction with a maleimide segment to complete the reaction [11]. Unless sufficient pressure is maintained, the evolution of highly volatile cyclopentadiene can produce voids in the cured resin [12-13]. Crosslinking of amino moieties is due to a Michael addition reaction.

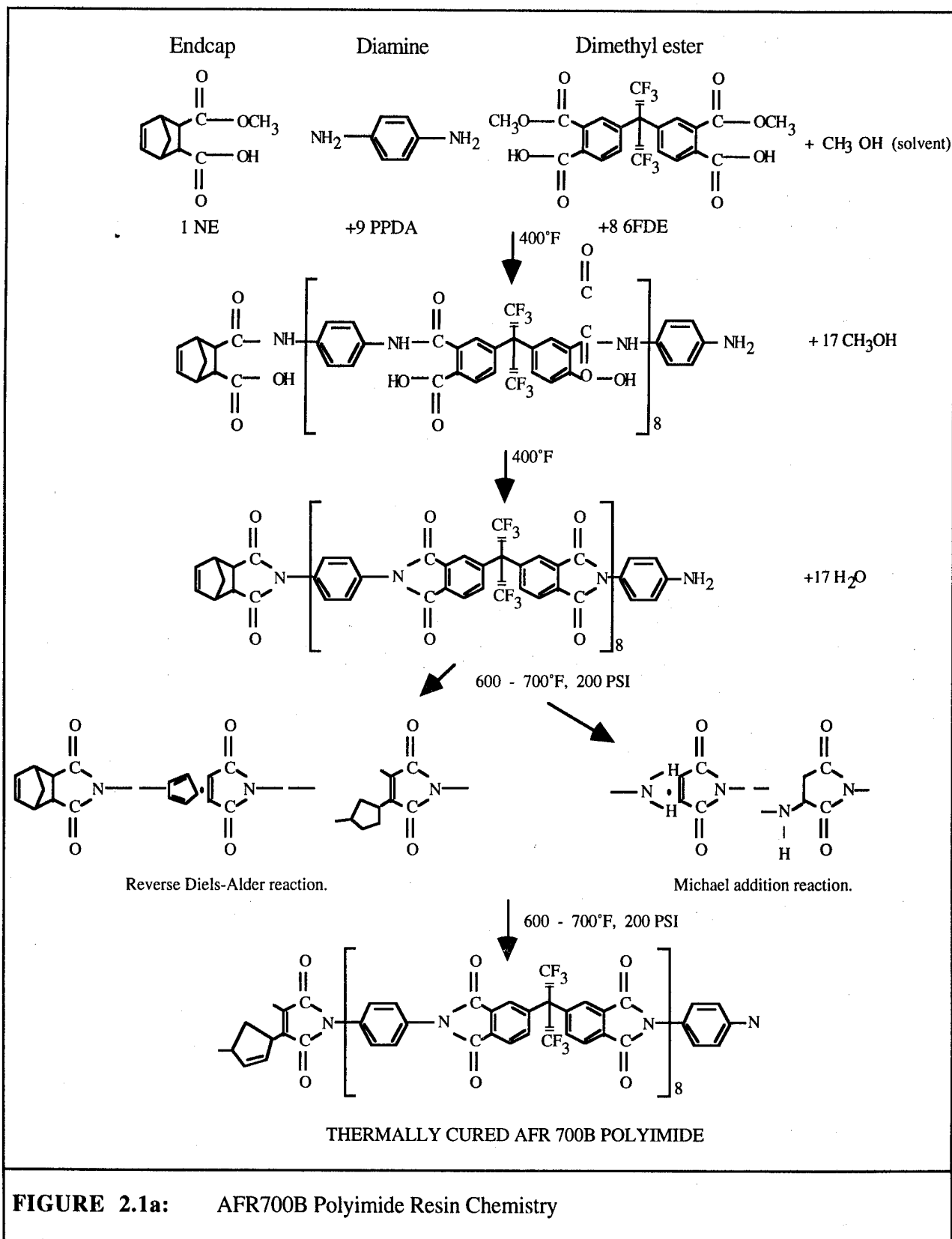
It appears that crosslinking through the amino moieties is more efficient than crosslinking through the nadic endcap in the sense that the former leads to a significantly higher glass transition temperature than does crosslinking only through the nadic endcap (case of PMR-15) [2]. Again, here it is important to emphasize that the high temperature crosslinking reaction is a very complex process and all the steps of the reaction sequence are still not understood.

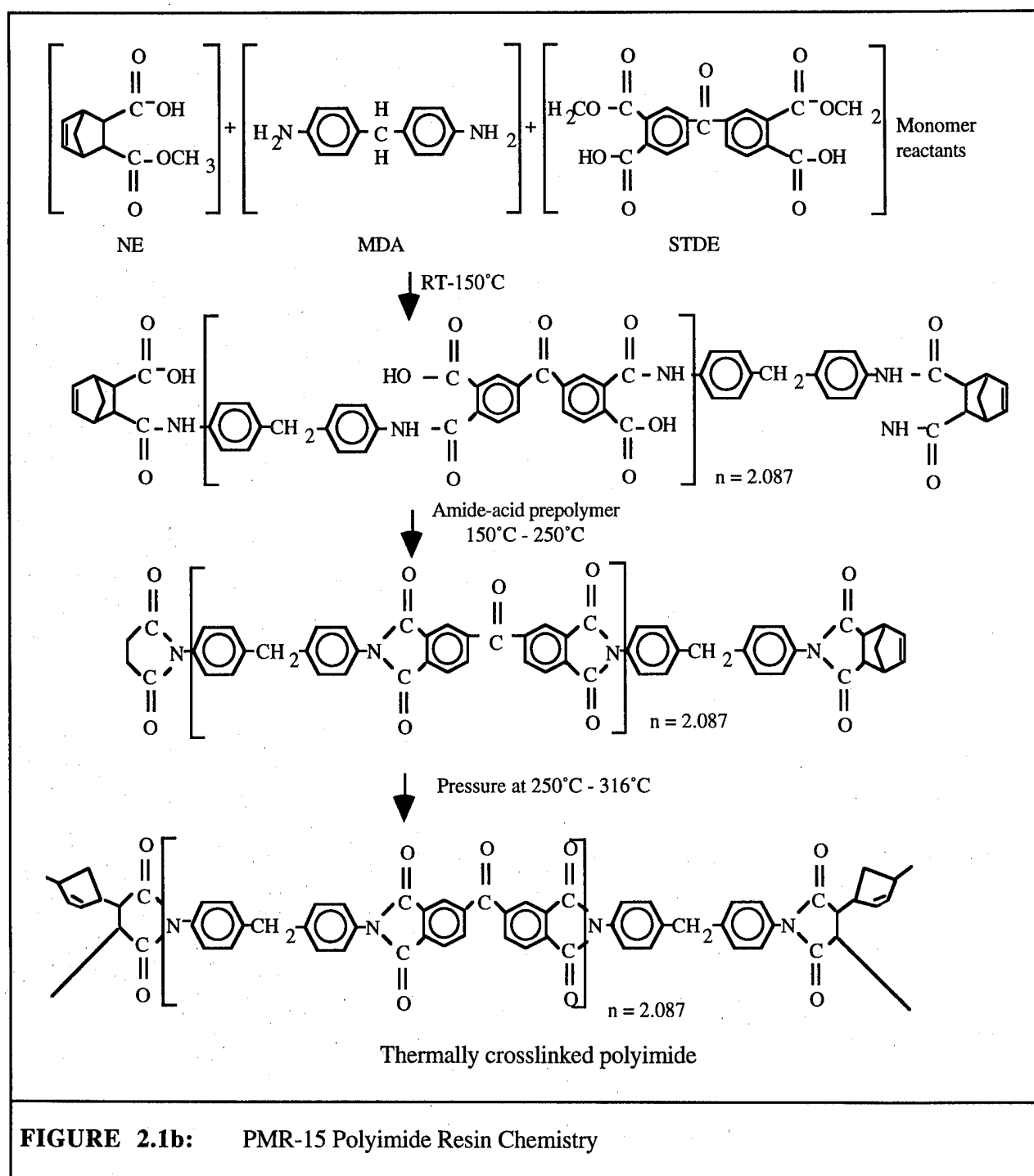
The presence of only one nadic endcap on each prepolymer chain in the AFR-700B polyimide resin tightens the molecular weight distribution and improves resin temperature capability, compared to the PMR-15 resin, without sacrificing autoclave processability [2]. The AFR-700B resin has a higher prepolymer formulated molecular weight (4382) compared to the PMR-15 resin (1500). It is reasonable to assume that because the AFR-700B polyimidization reaction is based on the classic PMR-15 approach, the influence of the competing reactions discussed above will occur to a lesser degree in the AFR-700B polyimide resin.

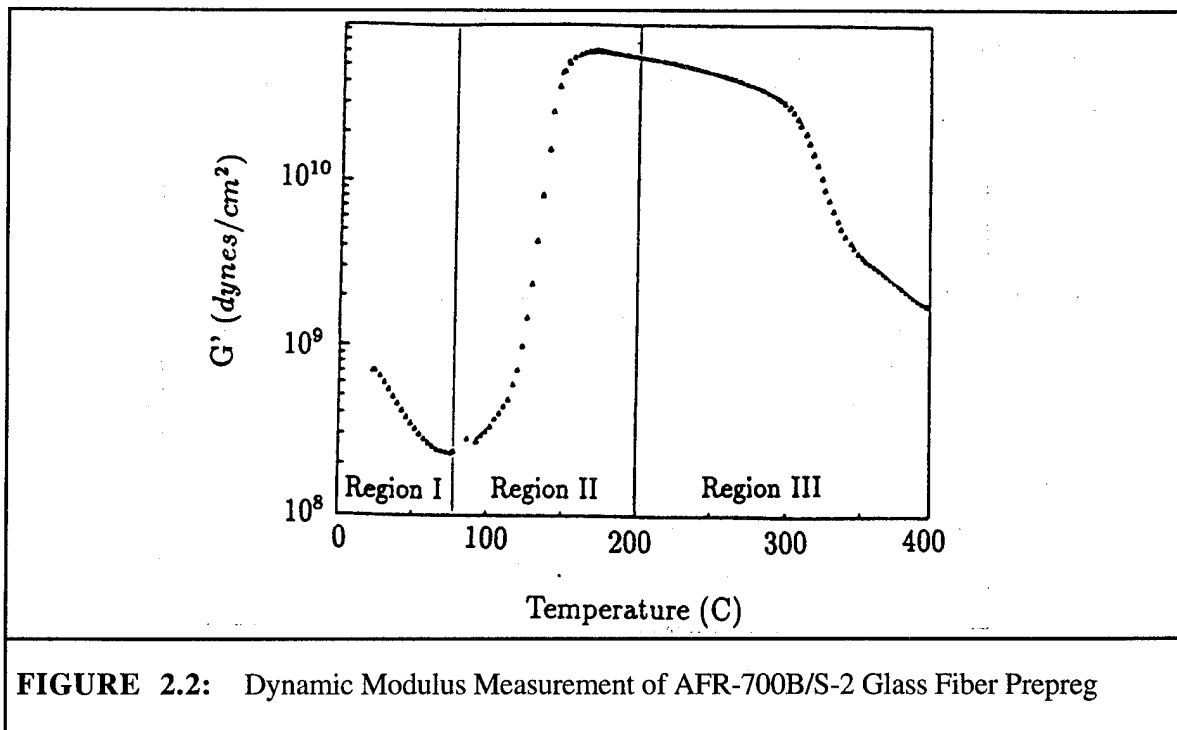
Figure 2.2 shows Rheometric dynamic spectrometer measurements for AFR-700B/S-2 glass fiber prepreg in the torsion mode for a heating rate of 2°C/min. [14]. One can divide this profile into three regions. In region I the initial lowering of system stiffness as indicated by the storage modulus, G' , is due to the melting and redissolving of the solid monomer into the solvent in the prepreg. Somewhere around 75°C reaction starts within the liquid phase of aromatic dianhydrides, aromatic diamines and solvent, causing the viscosity decrease to stop [5]. In region II a steep

increase is associated with increasing molecular weight through amidization and then imidization. In this region a relatively large volume of solvent and water vaporizes due to the polycondensation reaction. The modulus rises rapidly until 170°C. After this temperature the rate of polyimidization slows down. Region III is marked by a slightly decreasing modulus which drops after 310°C as formed polyimide oligomer passes its glass transition temperature [19]. Continued heating causes the stiffness to decrease further and leads to occurrence of a softening region. In this region the reverse Diels-Alder crosslinking reaction starts (cyclopentadiene is released prior to further participation in the crosslinking reaction), followed by the Michael addition crosslinking reaction with increasing temperature [15].

With an isothermal hold at 400°C, the resin continues to stiffen even after 18 hours [16], indicating a continuing slow crosslinking reaction which advances the glass transition temperature of the polyimide resin.







2.2 Model Development History

In order to fabricate a composite of high quality, a model describing the entire autoclave process (Master Model) is useful for understanding and controlling the polymerization process. The Master Model includes submodels for reaction kinetics, viscosity, devolatilization, heat transfer, resin flow (consolidation) and void formation.

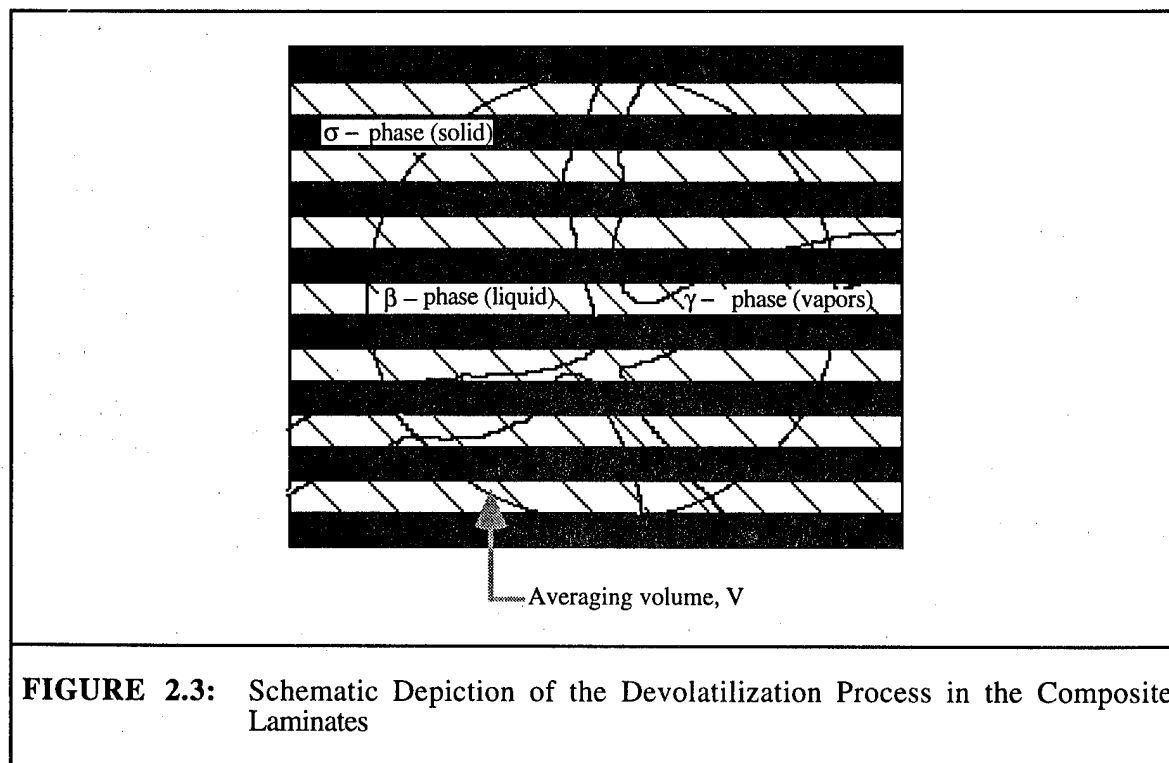
A submodel for describing the consolidation process (i.e., resin flow model) has been proposed using soil consolidation theory [17-18] and experimentally verified [19]. Also, a submodel describing the devolatilization of polyimide composites has been proposed [19]. The latter predicts the total and individual volatile mass fluxes, as well as the temperature and pressure profiles through the laminate as a function of the initial part thickness and the temperature - pressure - time cycle employed during autoclave processing [1]. This devolatilization submodel was partially verified for the case of Avimid K-III condensation polyimide resin by measuring the total and component volatile fluxes out of the laminate [20].

In this study the devolatilization submodel was streamlined and made more general so that it can accommodate additional condensation polyimide systems as they become available. We present the devolatilization submodel in some detail here for the sake of completeness.

2.3 Devolatilization Model

The system considered is a three phase porous media system (Figure 2.3). The solid phase σ (fiber) is considered as inert, the liquid phase β (monomer, polymer and solvent) is assumed to be stationary because of high viscosity and the gas phase γ (volatiles) is assumed to be continuous with transport occurring by convection.

In the devolatilization model the basic equations of mass, momentum, and energy transport are used as the governing equations. The complex geometry of the porous medium makes it difficult to solve these transport equations. A different set of governing equations will arise for each phase and there is no way of knowing a priori in which phase an arbitrary point lies and, therefore, which set of equations is appropriate. In order to achieve solvable governing equations which are valid throughout the composite, the volume-averaging method [21] is used to formulate tractable models of heat and mass transport in the composite system. Since the ratio of thickness/length is very small in the composite, a one-dimensional model can be employed.



In the model, it is assumed that [20]:

- i) the laminate thickness is constant during this initial part of the curing cycle and the solid phase is an inert body and is fixed in an inertial frame
- ii) polymerization occurs by step reaction in the liquid phase
- iii) transport of evolved gas dominates at least in the first two regions of the process shown in Figure 2.2. Diffusion may be important in Region III and toward the end of Region II, but it is not a major consideration in the overall volatile management problem
- iv) local thermal equilibrium exists at any point of the prepreg
- v) gas velocity can be related to pressure drop by Darcy's law

2.3.1 Energy Equation

$$\rho_m C_{p_m} \frac{\partial T}{\partial t} + \rho_\gamma C_{p_\gamma} V_\gamma \frac{\partial T}{\partial x} = - \sum_{i=1}^N (-\Delta H_{vap_i}) \frac{\dot{m}}{M_{w_i}} + k_{eff} \frac{\partial^2 T}{\partial x^2} + \Delta H_r R_A \quad (2.1)$$

$$I.C. \quad t = 0, T = T_0 \text{ for all } x \quad (2.2)$$

$$B.C. \quad x = 0, T = T_0(t) \quad (2.3)$$

$$B.C. \quad x = L, k_{eff} \frac{\partial T}{\partial x} = h(T - T_b) \quad (2.4)$$

The first term on the left-hand side of equation (2.1) is the rate of change of internal energy per unit volume and the second term accounts for the convective thermal transport of gases through the composite. The first term on the right side of equation (2.1) accounts for the energy loss due to the evaporation of the volatile species, the second term is the heat transport by thermal conduction, and the third term is the heat of the reaction.

Two boundary conditions are needed at the composite surfaces. Equation (2.3) represents the heating ramp at the tool surface and equation (2.4) is convective heat transfer from the composite top surface to the bleeder.

In equation (2.1), ρ_m and C_{p_m} are the overall average density and heat capacity for the three-phase mixture

$$\rho_m C_{p_m} = \epsilon_\sigma \rho_\sigma C_{p_\sigma} + \epsilon_\beta \rho_\beta C_{p_\beta} + \epsilon_\gamma \rho_\gamma C_{p_\gamma} \quad (2.5)$$

k_{eff} is the volume-average thermal conductivity for the three-phase mixture

$$k_{eff} = \left(\varepsilon_{\sigma} k_{\sigma}^r + \varepsilon_{\beta} k_{\beta}^r + \varepsilon_{\gamma} k_{\gamma}^r \right)^{1/r} \quad (2.6)$$

where σ, β , and γ represent solid, liquid, and gas phases and ε_{β} , ε_{γ} , and ε_{σ} are the volume fractions of the liquid, gas, and solid phase in the prepreg, respectively. The x is the coordinate perpendicular to the tool surface, L is composite thickness, ΔH_{vap_i} is the heat of evaporation of the i -th volatile component, ΔH_r is the heat of reaction, R_A is the reaction rate, \dot{m}_i is the local volatilization mass flux of the i -th component, M_{w_i} is the molecular weight of the i -th component, subscript m refers to the mixture and subscript γ to the gas phase, T is local temperature, T_b is the temperature of the bleeder, h is the heat transfer coefficient, r is a topological parameter, and V_{γ} is the gas phase velocity obtained by Darcy's law. The maximum Reynolds number for volatiles based on the pore size and volatile flow rate in the laminate is calculated to be around 0.1, which suggests that Darcy's law is applicable for such a system. The relation between the gas phase velocity V_{γ} and pressure drop is given by

$$V_{\gamma} = - \frac{K_{\gamma}}{\mu_{\gamma}} \frac{\partial P_{\gamma}}{\partial x} \quad (2.7)$$

$$B.C. \ x = 0, \ V_{\gamma} = 0 \quad (2.8)$$

The gas phase permeability, K_{γ} , is assumed to be a constant, and μ_{γ} is the gas phase viscosity.

2.3.2 Mass Balance on the Liquid Phase

$$\rho_{\beta} \frac{\partial \varepsilon_{\beta}}{\partial t} + \varepsilon_{\beta} \frac{\partial \rho_{\beta}}{\partial t} = - \sum_{i=1}^N \dot{m}_i \quad (2.9)$$

$$I.C. \ t = 0, \ \varepsilon_{\beta} = 1 - \varepsilon_{\sigma_0} - \varepsilon_{\gamma_0} \quad (2.10)$$

where ρ_{β} is the volume average liquid density which is a function of liquid composition

$$\rho_{\beta} = \sum_{i=1}^N \phi_i \rho_{\beta_i} \quad (2.11)$$

Here ϕ_i is the volume fraction of the i -th component and ρ_{β_i} is the density of the liquid species i .

The second term on the left-hand side of equation (2.9) can be shown to be unimportant compared with the first term.

2.3.3 Gas Phase Mass Balance

The gas diffusion is neglected in the early stage of devolatilization compared to the convective flux of gas driven by the pressure gradient

$$\frac{\partial}{\partial t} (\rho_\gamma \varepsilon_\gamma) + \frac{\partial}{\partial x} (\rho_\gamma V_\gamma) = \sum_{i=1}^N \frac{\dot{m}_i}{M_{w_i}} \quad (2.12)$$

$$I.C. \quad t = 0, \rho_{\gamma_i} = \rho_{\gamma_{i_0}} = \frac{P_{vac}}{RT} \quad (2.13)$$

$$B.C. \quad x = L, \rho_{\gamma_i} = Y_i \rho_{\gamma_{vac}} \quad (2.14)$$

2.3.4 Mass Balance on Active Groups in the Liquid

The mass balance on monomer is needed to monitor the degree of polymerization and the volatile generation rate. The diffusion term is neglected due to small diffusivities in the liquid

$$\varepsilon_\beta \frac{\partial C_A}{\partial t} = R_A - C_A \frac{\partial \varepsilon_\beta}{\partial t} \quad (2.15)$$

$$I.C. \quad t = 0, C_A = C_{A_0} \quad (2.16)$$

2.3.5 Mass Balance on Side Products ($i = 1, 2$)

$$\frac{\partial (\varepsilon_\beta C_i)}{\partial t} = 2R_A - \frac{\dot{m}_i}{M_{w_i}} \quad (2.17)$$

$$I.C. \quad t = 0, C_i = C_{i_0} = 0 \quad (2.18)$$

C_i is the molar concentration of species i , R_A is the rate of reaction, and C_A in equation (2.15) is the sum concentration of active groups in monomer and polymer.

2.3.6 Mass Balance on Solvent ($i = 3$)

$$\frac{\partial (\epsilon_\beta C_i)}{\partial t} = - \frac{\dot{m}_i}{M_{w_i}} \quad (2.19)$$

$$I.C. \quad t = 0, C_i = C_{i_0} = 0 \quad (2.20)$$

2.3.7 Gas Molar Fraction Equations ($i = 1, 2, 3$)

$$\frac{\partial Y_i}{\partial t} = \left(\frac{RT}{P\epsilon_\gamma} \right) \left[\frac{\dot{m}_i}{M_{w_i}} - Y_i \sum_{i=1}^N \frac{\dot{m}_i}{M_{w_i}} \right] + \frac{K_\gamma}{\epsilon_\gamma \mu_\gamma} \frac{\partial P}{\partial x} \frac{\partial Y_i}{\partial x} \quad (2.21)$$

$$I.C. \quad t = 0, Y_i = Y_{i_0} \quad (2.22)$$

$$B.C. \quad x = 0, \frac{\partial Y_i}{\partial x} = 0 \quad (2.23)$$

In order to solve the above set of equations, the evaporation rate of the i -th volatile component is calculated from the following constitutive equation. This equation is based on the assumption that there is a mass transfer resistance on the liquid side to the transport of volatile species from the liquid to the gas phase

$$\dot{m}_i = (K_m A_\beta) (\phi_i \gamma_i P_i^{sat} - Y_i P) \quad (2.24)$$

$K_m A_\beta$ is the volumetric mass transfer coefficient between liquid and gas, γ_i is the activity coefficient of the i -th volatile component, ϕ_i is the volume fraction of species i in the liquid phase, P_i^{sat} is the saturation vapor pressure of pure component i , and Y_i is the molar fraction of the i -th volatile component in the gas. In the beginning of the devolatilization P is constant and equal to P_{vac_0} , and the dominant term for \dot{m} is $\phi_i \gamma_i P_i^{sat}$. At elevated temperature P_i^{sat} increases much faster than P . Therefore \dot{m} for methanol, isopropanol and water is hardly affected by P (or P_{vac}) regardless of whether or not full vacuum is applied under the bag in the autoclave process. It should again be pointed out that isopropanol is included here because the prepreg used to verify

the model and supply the model inputs did contain isopropanol. Current AFR-700B prepreg does not contain isopropanol.

The activity coefficient γ_i (based on the volume fraction ϕ_i) needed in evaluating the saturation vapor pressure in the liquid mixture is obtained by equation

$$\gamma_i = \exp \left[\frac{V_i}{RT} (\delta_i - \bar{\delta})^2 \right] \quad (2.25)$$

where $\bar{\delta}$ is the volume average solubility parameter which is a function of liquid composition

$$\bar{\delta} = \sum_{i=1}^N \phi_i \delta_i \quad (2.26)$$

here δ_i is the solubility parameter of species i , and V_i in equation (2.25) is the specific volume of the liquid state for species i .

A finite element collocation method based on the method of lines was utilized to solve the coupled partial differential equations. Several packages have been tested and the DPDE subroutine in the IMSL package (International Mathematics and Statistics Library, 1983 version) was chosen for simulation due to its efficiency and accuracy. The entire program is described elsewhere [22]. A list of model input parameters appears in the Appendix.

3.0 SENSOR SELECTION

Gas evolution adds a difficult dimension to condensation processing. Appropriate available sensor systems were evaluated for monitoring the polyimide devolatilization process. Each sensor system was examined for its accuracy throughout the temperature and pressure ranges required. Based on this examination, the best sensor system was used in a miniclave apparatus which was designed and constructed to monitor the devolatilization process.

3.1 Types of Sensors

3.1.1 Pressure

Kulite miniature pressure transducers were used because gas pressure sensitively reflects gas evolution. In order to assure repeated use of a single sensor, a special design for mounting sensors inside the laminate was used. The sensor was hermetically mounted inside a surgical tube and the sensor diaphragm protected against any contact with the liquid resin by shielding it with steel wool and a fine wire mesh.

3.1.2 Temperature

J-type thermocouples were used to measure the temperature distribution inside the laminate lay-up for different heating rates and laminate thicknesses.

3.1.3 Resin State Sensor

During the polymerization process, the polymer ionic viscosity changes. The Numeric system II Microdielectrometer (Micromet Instruments Company) and a high temperature ceramic sensor were used to monitor the ionic viscosity of the AFR-700B prepreg during the polycondensation reaction. The dielectrometer generates an excitation energy at an alternating frequency of between 0.1 and 10,000 Hz.

The surface of the sensor contains electrodes which are placed between prepreg plies so that they become immersed in resin. A low level voltage is applied to one of these electrodes and causes a signal of the same frequency to be induced in the second electrode. The induced signal exhibits a reduction in amplitude and a phase angle shift relative to the applied voltage. The amplitude change and the phase angle shift are unique functions of the electrode configuration and the dielectric

properties of the resin. The dielectrometer measures the change in amplitude and phase angle and calculates the dielectric properties. The dielectric data, along with time and temperature data, are then stored and further data analysis can be performed by the controlling computer using software provided by the system manufacturer.

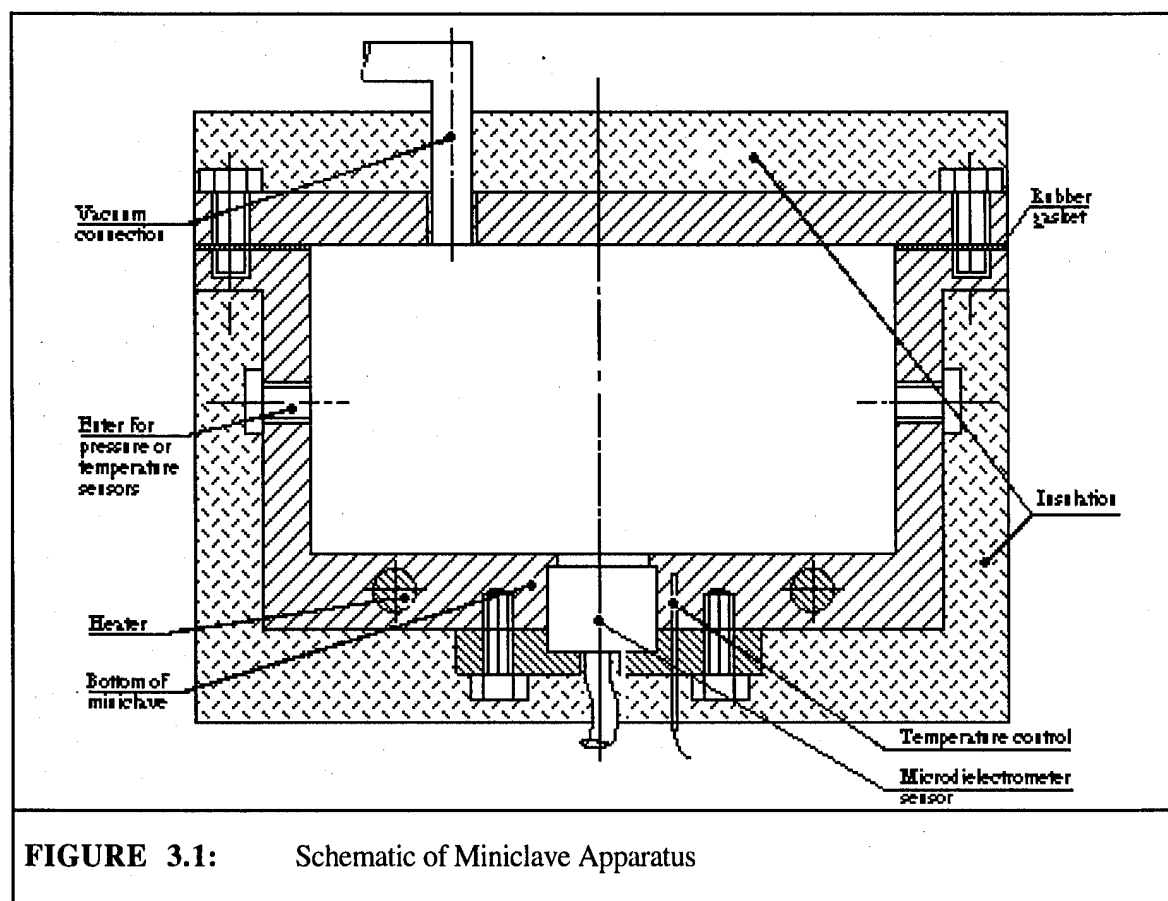
The sensor was flush-mounted in the bottom of the miniclave and connected to the Eumeric System II data acquisition system. This sensor consists of interdigitated silver-palladium electrodes embedded in a rugged, abrasion resistant, ceramic substrate 2 cm in diameter. The electrode pattern on the sensor covers an area of 1.8 cm by 1.8 cm. The substrate is 2 cm thick and can withstand pressures in excess of 3000 psi and temperatures up to 380°C. The sensor surface can be cleaned with sandpaper and cleaning solvent without damaging the electrodes.

To test the sensor, six individual prepreg plies (5 x 5 cm lateral dimension) were laid-up unidirectionally against the smooth tool surface containing the flush-mounted sensor and covered with a steel wool bleeder and an aluminum caul plate. Dielectric measurements have been previously used to study the imidization reaction in a PMR-15 polyimide resin [23].

3.2 Miniclave Apparatus

The miniclave is aluminum and was designed and built for this study (Figure 3.1). The top plate contains a pressure control line and a pressure sensor. The bottom contains a cast-in heater and a thermocouple control circuit connected to a programmable temperature controller, as well as the dielectric sensor. The miniclave can accept laminates up to 14 x 14 cm lateral dimension and up to 2 cm thick (50 plies). On each side of the miniclave is an entry port for thermocouple and pressure sensor connections. The unit can maintain pressure and temperature conditions required for polyimide experiments (temperature range 20°C to 370°C, pressure range 0.4 psi to 100 psi).

Computer simulations for pressure distribution along the thickness of the laminate indicate that the maximum gas pressure exists on the tool surface at the center of the laminate [20]. For this reason the pressure transducer was located at the tool side of the laminate. As heat is supplied from the bottom at a set rate and vacuum is applied to the bleeder side of the laminate, the gas pressure is measured as a function of time. The change in laminate resin state measured by the microdielectrometer is gathered at the same time as the pressure measurement using IBM-PC compatible software. The temperature distribution inside the laminate measured by the *J*-type thermocouples and the miniature pressure transducer data were collected by an Analog Device data acquisition system.



4.0 DETERMINATION OF MODEL INPUT PARAMETERS

4.1 Resin Characterization

The AFR-700B neat resin and the prepreg were manufactured by Ethyl Company and were used for the thermal analysis. The neat resin contained 8.3 wt% methanol and 7.5 wt% isopropanol as a solvent solution. The nadic endcap (NE) was 100% methyl ester; 90% methyl ester with the balance of isopropyl ester (10%) was used as the 6-FDE moiety. The presence of isopropanol in the solvent solution improves the prepreg processability. The Ethyl Company prepreg was prepared using a pseudo-hot-melt process and the same batch of the resin as described above; it contained 5.7 wt% methanol, 5.7 wt% isopropanol and 61 wt% of S-2 glass fiber. The AFR-700B neat resin was sealed in a plastic container and the prepreg roll in a polyethylene bag. The neat resin and prepreg were stored at -18°C until processed in order to prevent any premature chemical reaction.

Calorimetric and weight loss measurements were performed with the Perkin-Elmer DSC-4 and TGS-2 apparatus. Both systems were calibrated according to the procedure recommended by the manufacturer.

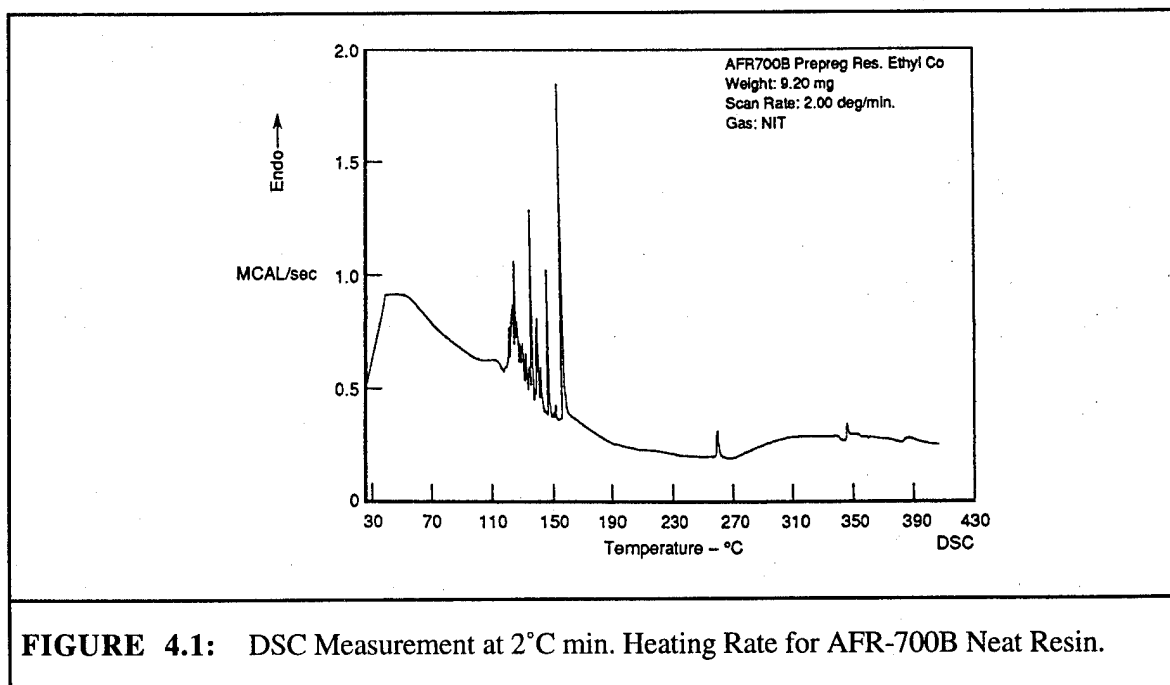
4.1.1 DSC Measurements

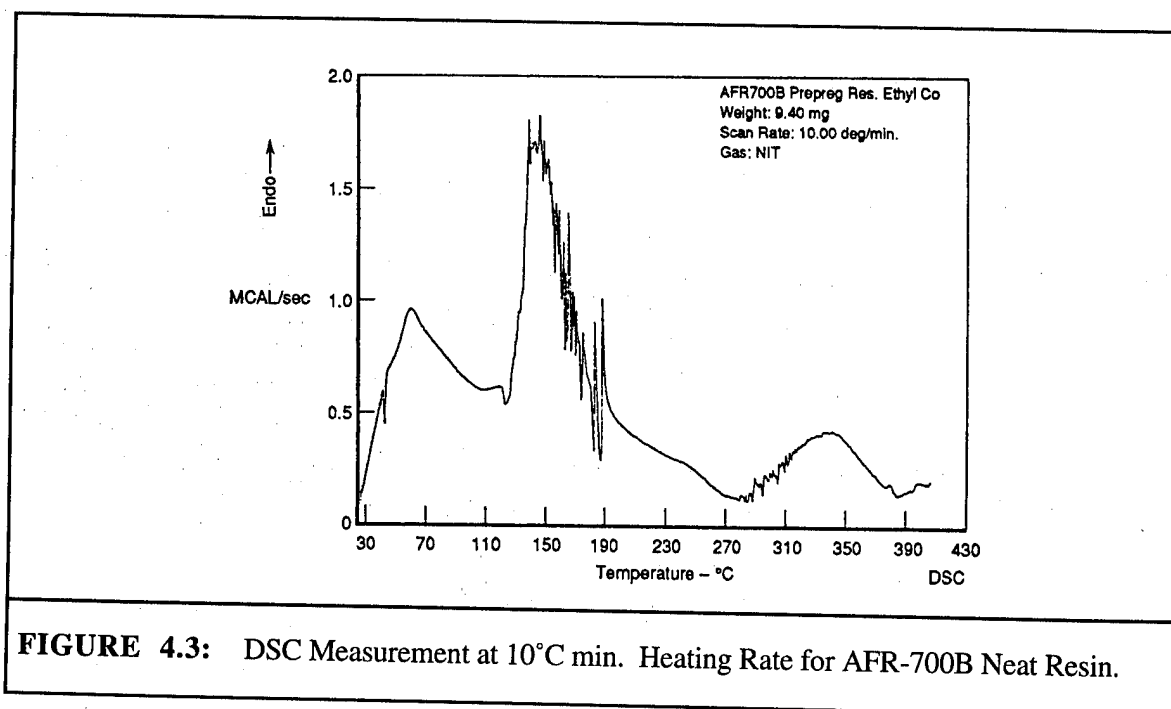
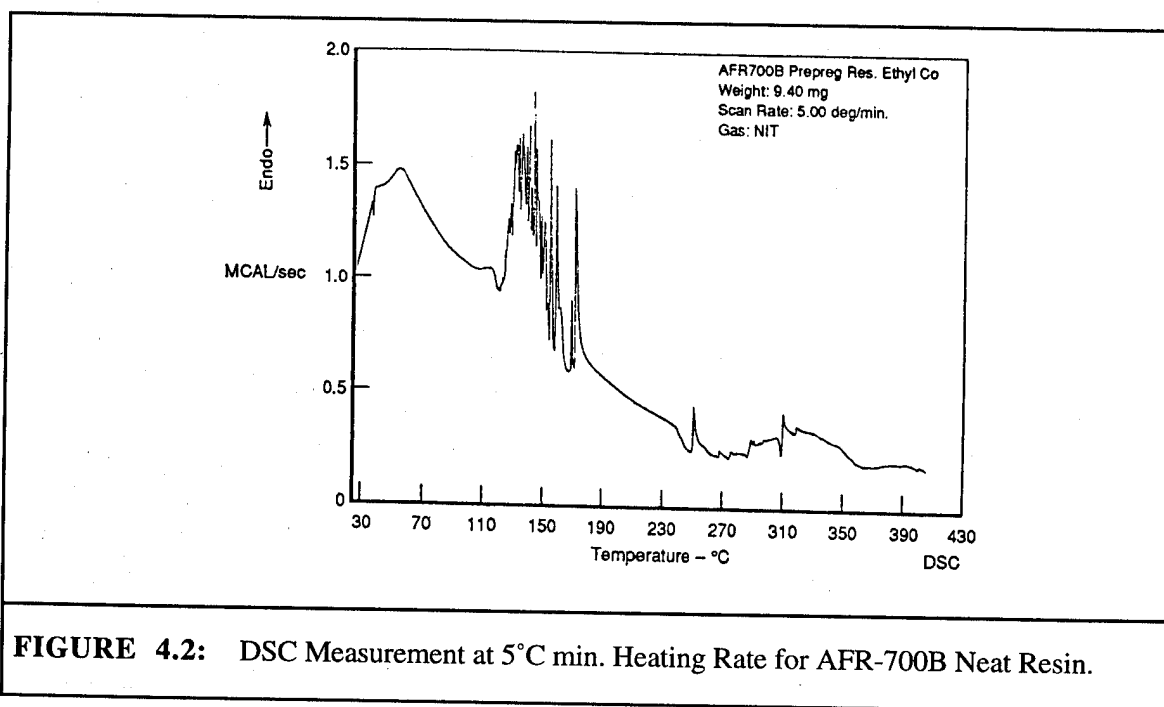
Differential scanning calorimetry (DSC) was performed with the Perkin-Elmer DSC-4 apparatus and Perkin-Elmer TADS thermal analysis data station. Nitrogen gas was used to continuously purge the furnace compartment. Aluminum pans and covers were used as sample and reference containers.

DSC scans for the AFR-700B neat resin manufactured by Ethyl Company were performed at three different heating rates (2, 5, and 10°C/min) and are shown in Figures 4.1 to 4.3. The small endotherm in the beginning of the scan is due to devolatilization of the original prepreg solvent (methanol and isopropanol). As the sample is heated up, somewhere around 80°C, exothermic amidization followed by imidization starts. However, this exotherm is very soon overlapped by an endotherm attributed to the devolatilization of methanol and water, which are side products of the polycondensation reaction. Small amounts of methanol, water and cyclopentadiene (which is a product of the reverse Diels-Alder crosslinking reaction) continue to evaporate in detectable amounts at 380°C. Above 380°C the scan is erratic, but some evaporation no doubt still continues. The effect of heating rate is dramatic. Increasing heating rate causes a large increase in the

sensitivity of the measurement as expected, but this is accompanied by a much more erratic scan caused by cavitation. Cavitation results in porosity at the sample pan surface due to violent outgassing [24]. The problem of violent outgassing was eliminated by drying the neat resin for 1 hour at 110°C and 2.4 psi. The DSC scan of the dry neat resin powder indicates again that an endotherm occurs due to evolution of polyimidization by-products (Figure 4.4). After holding the sample at 370°C for 2 hours, the sample was rescanned (Figure 4.5), showing that the polycondensation (polyimidization) reaction is completed, and polyimide oligomers were formed. The glass transition temperature, T_g , of the polyimide oligomer is about 310°C as determined by DSC. A broad exotherm after the glass transition point indicates the beginning of the crosslinking reaction.

The DSC scans of the high temperature polyimides are very difficult to analyze quantitatively, because of the noise caused by exiting volatiles and because of the overlap of the heat evolution by the exothermic polyimidization and the endothermic vaporization of the solvent and the polycondensation by-products. By raising the pressure to 800 psi during the calorimetric measurement, vaporization can be shifted out of the polyimidization cure region, and a two-stage curing exotherm is observed [25]. But, there is one potential drawback; the retention of the solvent volatiles and polycondensation by-products leads to different reaction kinetics than obtained in an industrial autoclave cure [24].





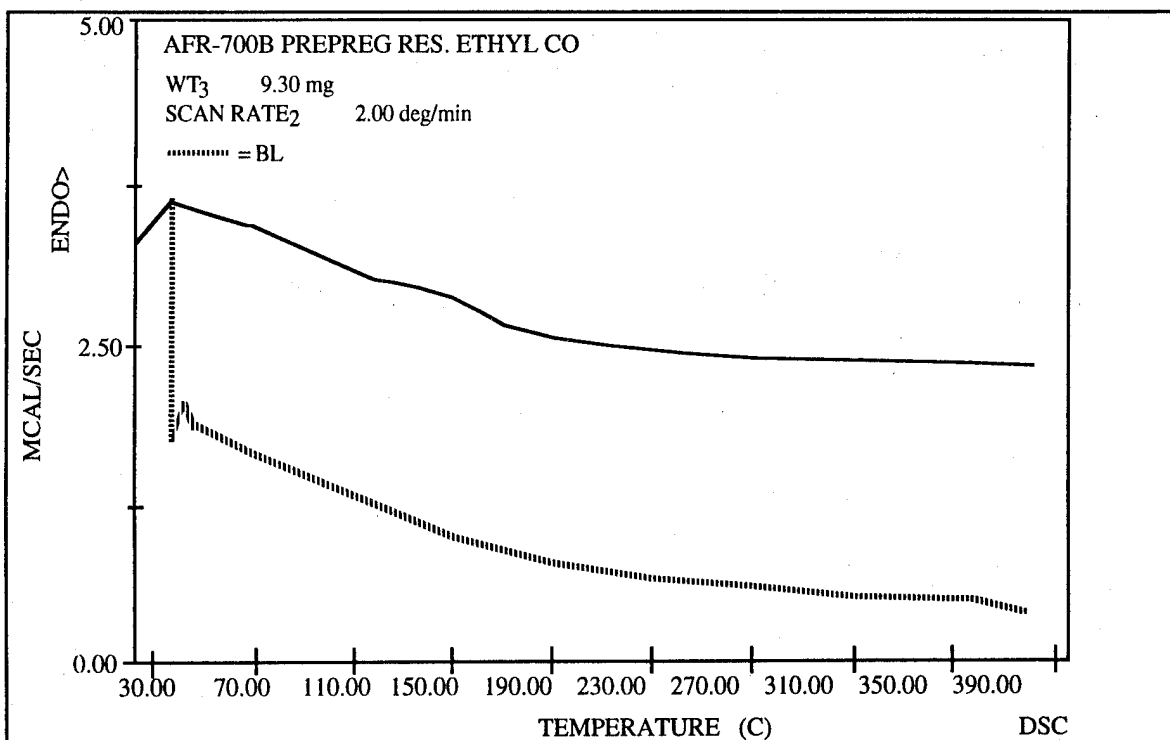


FIGURE 4.4: DSC Measurement at 2°C min. Heating Rate for AFR-700B Dry Neat Resin.

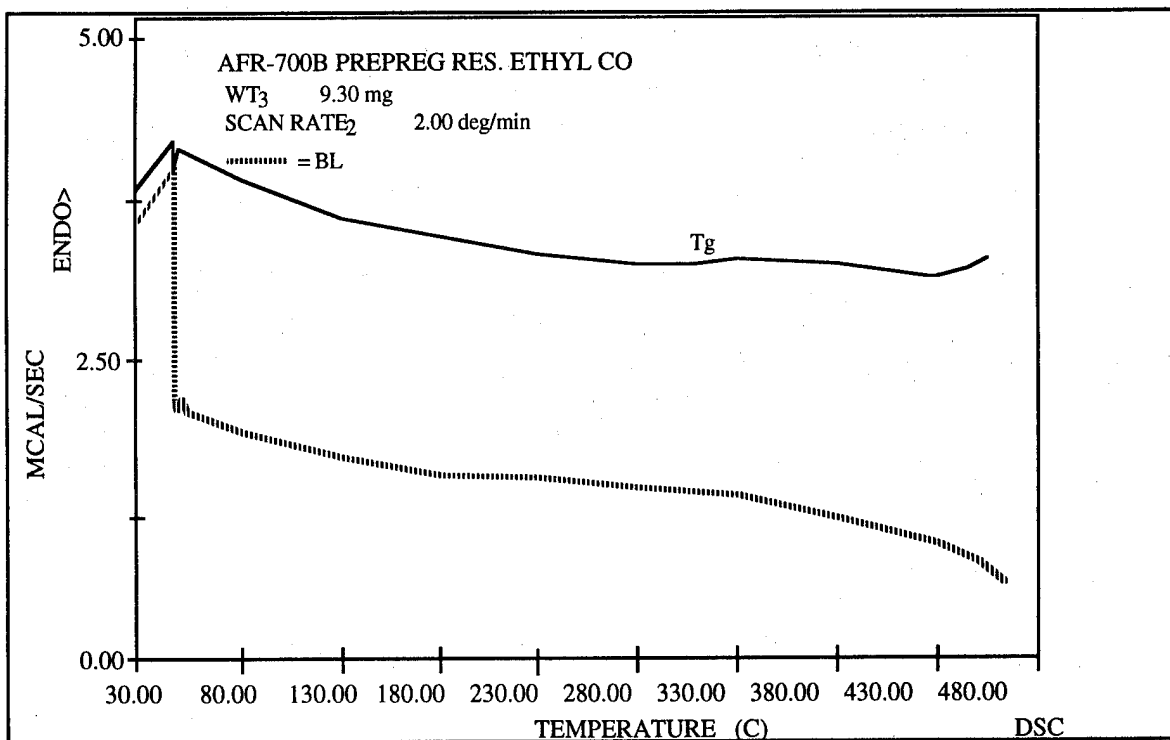


FIGURE 4.5: DSC Measurement at 2°C min. Heating Rate for AFR-700B Polyimide Oligomer

4.1.2 Thermogravimetric Measurements

The Perkin-Elmer TGS-2 thermobalance was used for weight loss measurements of the AFR-700B Ethyl Co. prepreg. Aluminum sample pans were used as sample and reference containers, and an accessory derivative unit permitted additional recording of the first derivative of the sample mass change. The prepreg sample preparation method was identical to the method described in section 4.3. Figure 4.6 shows weight loss measurements together with the derivatives at two different pressure environments (760 and 20 Torr) and a heating rate of 2°C/min. The scans indicate that weight loss during the polyimidization reaction occurs in two steps. The first weight loss is mainly due to devolatilization of original prepreg solvent, and the second step is due to polycondensation by-products.

The evolution of the products of polycondensation is completed at about 320°C. It is clear that vacuum influences the devolatilization process. The weight loss begins at lower temperatures when vacuum is applied, because the volatiles of the original prepreg solvent and by-products of polycondensation are removed more quickly from the prepreg sample under the vacuum driving force. The influence of the heating rate and bubble formation process on the mode of volatile evolution (weight loss) was measured and is reported in section 4.3.

4.1.3 Optical Microscopy Study of Neat Resin

The morphological changes during the polyimidization reaction for AFR-700B neat resin were studied using transmitted polarized light (Leitz optical microscope, magnification 320 times). The polarizer and analyzer have their electric vectors crossed at 90° to each other. The neat resin was placed between two glass slides and heated using a heating stage (Leitz 1350) with a heating rate of 2°C/min.

Figure 4.7 shows bubbles (black circles) which were formed as the evaporation of the volatiles started. The as-received AFR-700B neat resin is completely homogeneous. There is no indication of dispersed crystals (light spots). With the heating of the sample up to 90°C, bubbles continue to grow due to devolatilization of the solvent and by-products of the polycondensation reaction (Figure 4.8). The material continues to be optically inactive as the temperature of the sample reaches 200°C and 250°C (Figures 4.9 and 4.10). There is no indication of crystallite formation in the neat resin at these temperatures. These optical microscopy results are consistent with the interpretation of the DSC thermograms which were presented and discussed earlier.

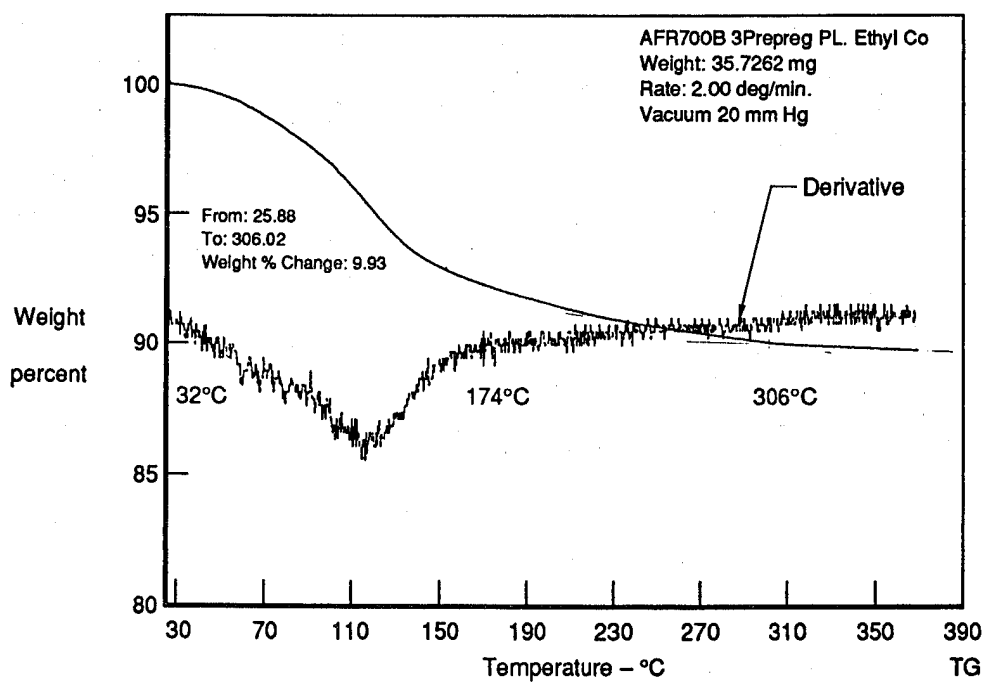
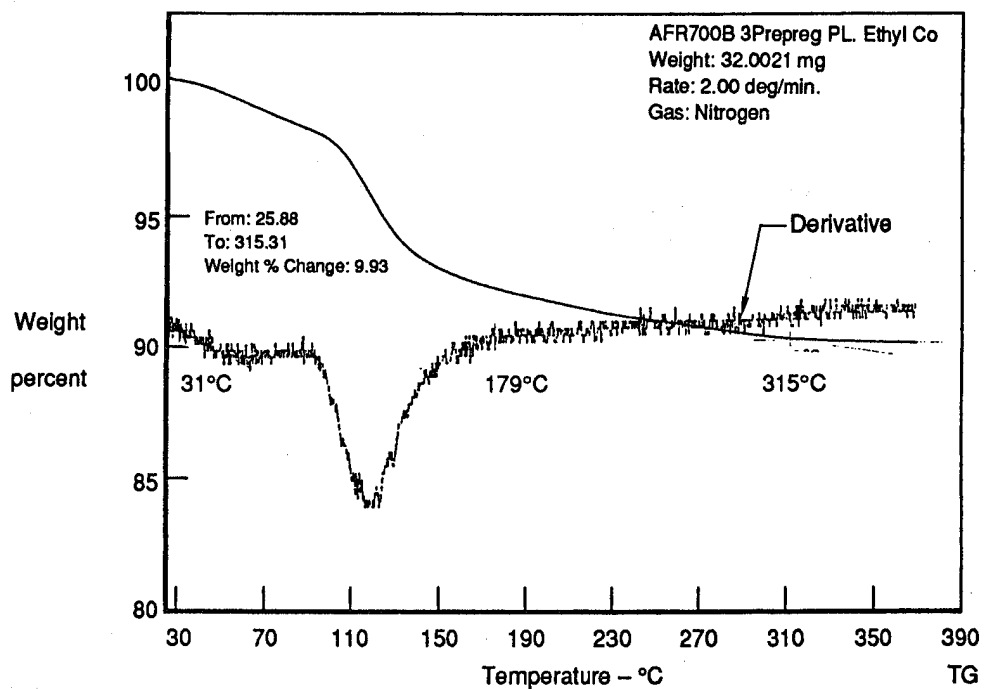


FIGURE 4.6: Experimental Results for the Weight Loss from a 3-Ply, Unidirectional Laminate of AFR-700B/S-2 Glass Fiber as a Function of Temperature at 2°C min. Heating Rate and Pressures of 760 and 20 Torr.

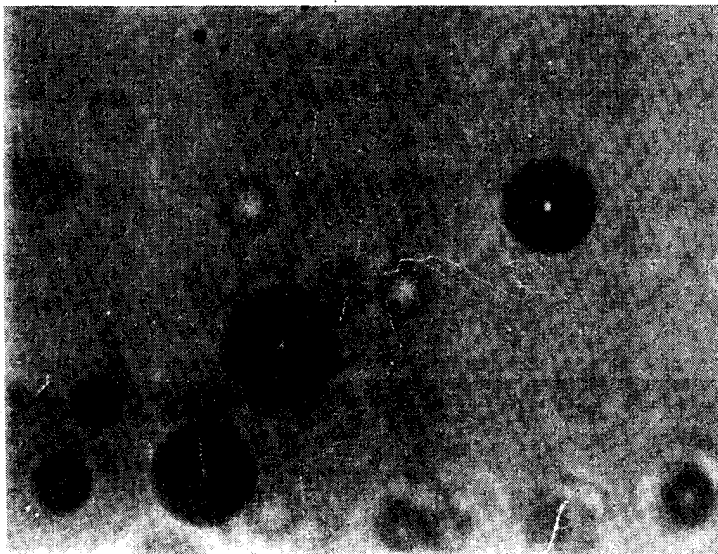


FIGURE 4.7: Optical Micrograph of the AFR-700B Neat Resin at 50°C (320 times Magnification, Transmitted Polarized Light).



FIGURE 4.8: Optical Micrograph of the AFR-700B Neat Resin at 90°C (320 times Magnification, Transmitted Polarized Light).

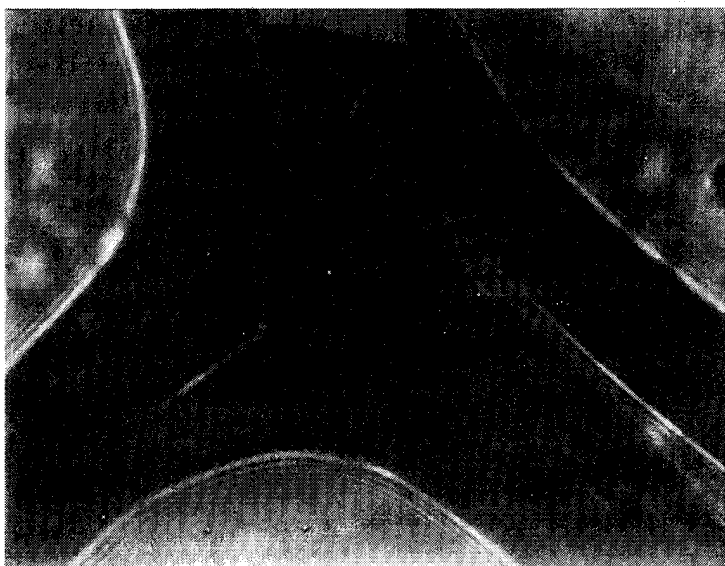


FIGURE 4.9: Optical Micrograph of the AFR-700B Neat Resin at 200°C (320 times Magnification, Transmitted Polarized Light).

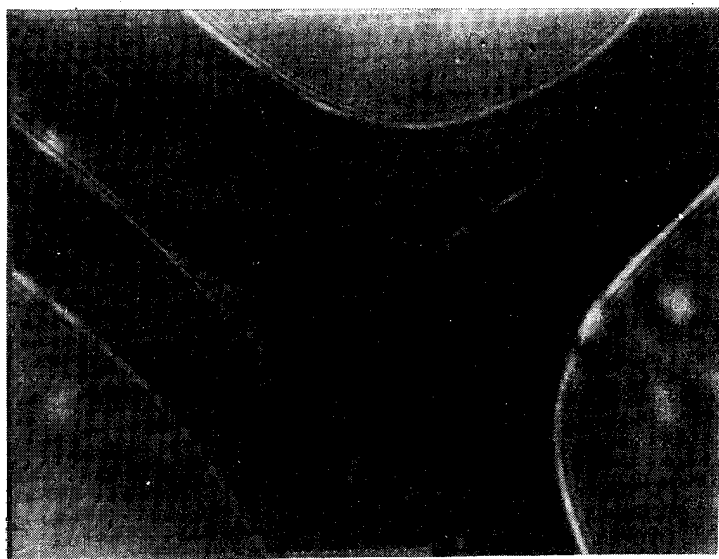


FIGURE 4.10: Optical Micrograph of the AFR-700B Neat Resin at 250°C (320 times Magnification, Transmitted Polarized Light).

4.1.4 Optical Microscopy Study of Laminate Surfaces

The phenomenon of volatile evolution during the polyimidization reaction was studied using incident light (magnification 35 times). The laminate was placed on a glass slide and heated at a rate of $2^{\circ}\text{C}/\text{min}$.

Figure 4.11 shows a photomicrograph of the laminate sample surface at room temperature. With increasing temperature, bubbles start to develop on the laminate sample surface as a large volume of the original solvent and products of the polycondensation reaction vaporize (Figures 4.12 and 4.13). With heating up to 170°C , the laminate resin dries to a powder consistency (Figure 4.14). Dry resin powder allows the remaining solvent and by-products of the polycondensation reaction to vaporize from the laminate at this stage of the cure process. These optical microscopy results are in agreement with dielectric resin state measurements which are presented later.



FIGURE 4.11: Optical Micrograph of the AFR-700B/S-2 Glass Laminate at Room Temperature (35 times Magnification, Incident Light).



FIGURE 4.12: Optical Micrograph of Bubbles Developing on Laminate Sample Surface at 90°C (35 times Magnification, Incident Light).



FIGURE 4.13: Optical Micrograph of Bubbles Growing on Laminate Sample Surface at 110°C (35 times Magnification, Incident Light).

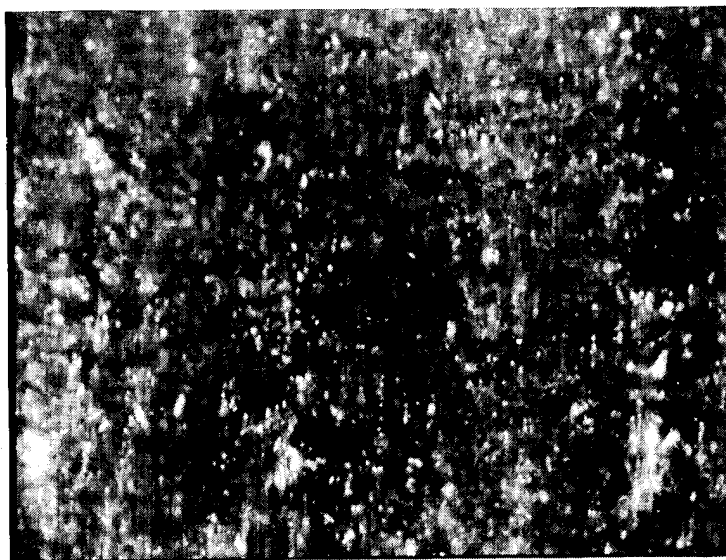


FIGURE 4.14: Optical Micrograph of the Dry Laminate Resin at 170°C (35 times Magnification, Incident Light).

4.2 Polymer Reaction Kinetics Model

The literature on the polyimidization reaction of PMR-15 resin was examined as a starting point in developing a kinetics model. Most studies used infrared (IR) spectroscopy to monitor the progress of reaction [5, 6, 10]. Attempts to characterize the kinetics of the imidization reaction of AFR-700B, which is related to the imidization reaction of PMR-15, must deal with the overlap of the heat evolution by the exothermic polyimidization and the endothermic vaporization of methanol and water, which are products of the polycondensation reaction.

One study [26] used the isothermal weight loss experiments for interpretation of the kinetics of the PMR-15 resin. The PMR-15 neat resin was dried under vacuum in order to remove the residual solvent, and the degree of conversion was determined by normalizing the weight loss as a function of time by the total weight loss. In another study isothermal differential scanning calorimetry (DSC) experiments, together with IR measurements, were used to examine the kinetics of the conversion of the polyamic acids into polyimides [27]. The net endothermal peak measured by isothermal DSC is a measure of the production of reaction products from imidization, and was used for quantitative estimation of the reaction enthalpy. The degree of conversion was determined

by normalizing the heat of reaction evolved up to a certain time by the total heat of reaction. This technique was shown to be more precise than other techniques, such as IR [27]. In other work, an analysis of the curing reaction of the polyimide formed from pyromellitic dianhydride (PMDA) and oxydianiline (ODA) by using Raman spectroscopy showed that there is a relationship between imidization rate and the solvent loss [28]. An Arrhenius-type relation was also used to describe the kinetics of solvent loss in the LARC-TPI polyimide system [29]; a strong relation was found between the imidization reaction and the solvent loss rates. Furthermore, a modified kinetics expression developed for the LARC-TPI system was used in the condensation model for the Avimid K-III polyimide composite [20].

In the absence of accurate kinetic information regarding the AFR-700B resin, it was assumed that the rate of disappearance of the active groups in the monomer and polymer, R_A , is proportional to the n -th power of the concentration of these groups in the resin, which in turn by mass balance is related to the time rate of change of the active groups in the resin by equation (4.1).

$$R_A = k (\varepsilon_b C_A)^n = -\frac{d(\varepsilon_b C_A)}{dt} \quad (4.1)$$

Here C_A is the concentration of the active groups in the monomer and polymer, ε_b is the volume fraction of the liquid phase in the prepreg, n is the reaction order, and k is the reaction rate constant described by the Arrhenius equation. By introducing the degree of polymerization, $p = 1 - (\varepsilon_b C_A) / (\varepsilon_{b0} C_{A0})$ the reaction can be expressed as an n -th order reaction

$$\frac{dp}{dt} = k_0 \exp\left(-\frac{E}{RT}\right) (1 - p)^n \quad (4.2)$$

where $k_0' = k_0 (\varepsilon_{b0} C_{A0})^{n-1}$. The degree of polymerization p was obtained from dynamic DSC measurements. The AFR-700B neat resin was dried at elevated temperature (110°C) and in vacuum (2.4 psi) in order to remove the residual solvent. The removal of the residual solvent from the resin before the dynamic DSC scans assures that the imidization of AFR-700B proceeds quickly and that the monomers react completely to form the imide. However, the dynamic DSC data cannot provide quantitative calorimetric data because the heat of reaction is offset by the heat of vaporization, since the evaporation of by-products of polycondensation (methanol and water) occurs simultaneously and is proportional to the extent of reaction. This proportionality allows one to determine reaction progress from the DSC data in the following manner.

Equation 4.2 can be rearranged to the form

$$\frac{dp}{dT} = \frac{k_0}{dT/dt} \exp\left(-\frac{E}{RT}\right) (1-p)^n \quad (4.3)$$

where dT/dt is the heating rate [30]. The degree of polymerization for three heating rates (2°C, 5°C, and 10°C) was plotted using the equation

$$\frac{dp}{dT} = \frac{dX_A}{dT} \quad (4.4)$$

where

$$X_A = \frac{A_t}{A_{Tot}} \quad (4.5)$$

Here A_t is the peak area evolved up to time t , and A_{Tot} represents overall peak area of reaction (Figure 4.15). Thus the net normalized heat as a function of temperature is directly related to the degree of polymerization. In the kinetic model, it was assumed that the heat of reaction, H_r , is much lower than the heat of devolatilization, H_D . The theoretical heat of imidization reaction is -28 kcal/mol, whereas the heat of water devolatilization alone is 162 kcal/mol based on each mole of polyimide oligomer formed [31].

During the dynamic DSC measurements, a thin layer of AFR-700B dry neat resin was placed at the bottom of the aluminum sample pan. It was assumed that there was not a conversion difference gradient through the thin layer of uniformly dispersed resin. Figure 4.15 represents the magnified overall reaction peak area of an experiment performed at 2°C/min heating rate and previously presented in section 4.1.2 (Figure 4.4). The temperature deviation from the perfectly linear temperature program during the dynamic DSC measurements was $\pm 1^\circ\text{C}$. The reproducibility of the dynamic DSC measurements was ± 0.2 mcal/sec. The analysis of the reaction peak area was performed with an accuracy of $\pm 2.5\%$.

The degree of polymerization p was obtained by Kim [30] from dynamic DSC scans by using the equation

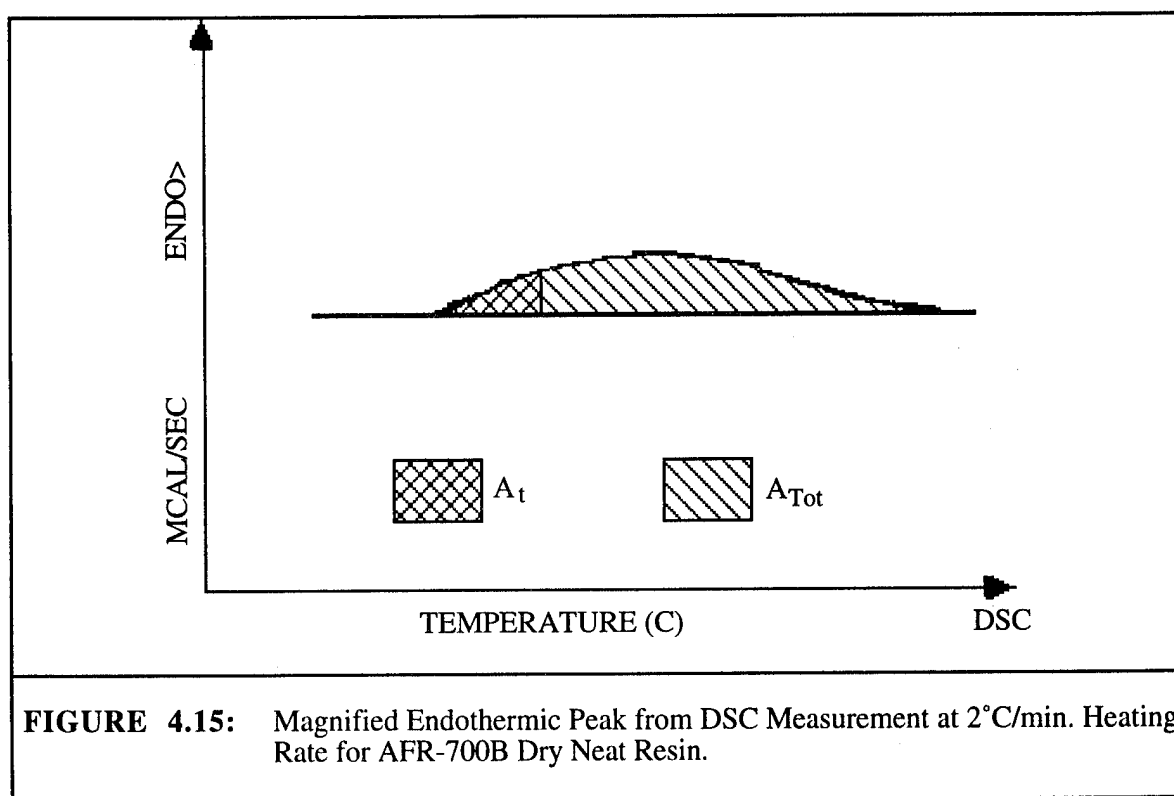
$$p = \frac{\Delta H_t}{\Delta H_r} \quad (4.6)$$

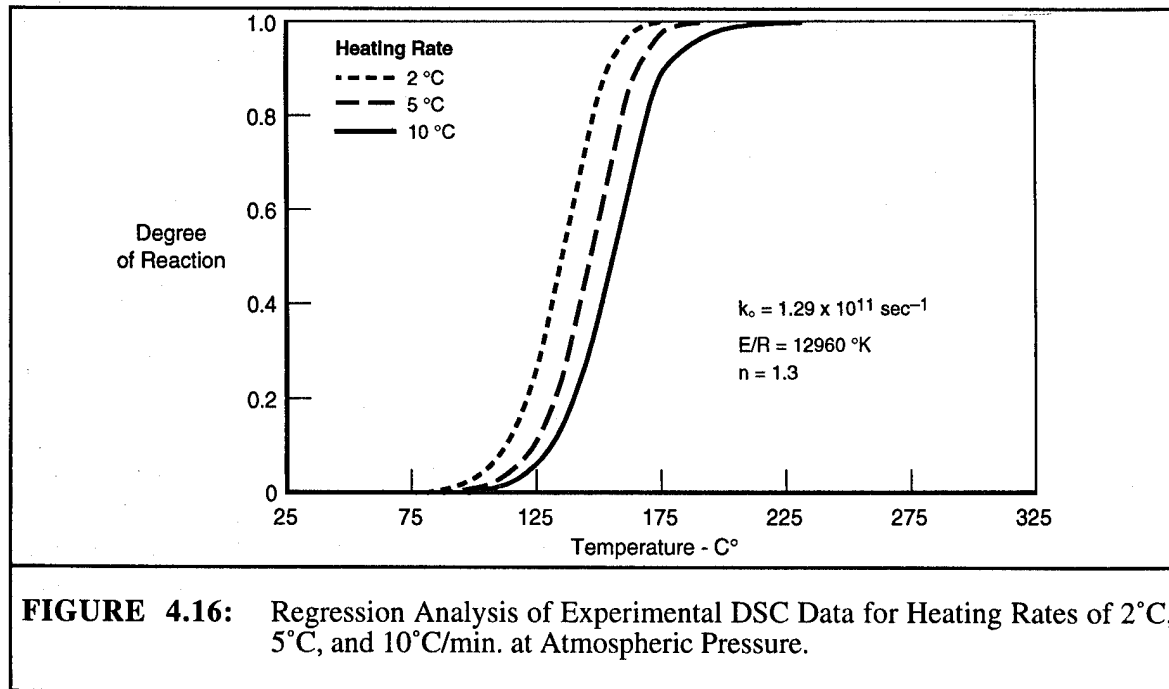
where ΔH_t is the peak area evolved up to time t , and ΔH_r represents the overall peak area of reaction. Thus the net normalized heat as a function of time is related to the reaction rate. The reaction kinetics parameters k_o , E , and n were obtained by Kim [30] from regression of the dynamic DSC measurements for different heating rates (Figure 4.16).

As a result of the best-fit of data at three different heating rates using equation (4.2) the reaction order was found to be 1.3, and an activation energy of 25.75 kcal/mol was obtained. The reaction kinetics can now be represented quantitatively by:

$$\frac{dp}{dt} = 1.29 \times 10^{11} \left(-\frac{12960}{T} \right) (1 - p^{1.3}) \text{ sec}^{-1} \quad (4.7)$$

This method incorporates the amidization reaction as well as the imidization reaction in the overall kinetics. A more representative measurement of the reaction kinetics might be accomplished by following the increase of an imide peak in the IR spectrum.





4.3 Mass Transfer Rates of Volatiles between Liquid and Gas Phases

The second major input variable to the devolatilization submodel is the volumetric mass transfer coefficient, $K_m A_\beta$. The experimental investigation of the devolatilization of the AFR-700B prepreg, by heating to various temperatures, indicated that the overall volumetric mass transfer coefficient $K_m A_\beta$ increases at first as devolatilization progresses, due to an increase in the interfacial area for mass transfer per unit volume of the composite, A_β . When polymerization takes place, the resin viscosity first decays and then builds up rapidly. The mass transfer coefficient, K_m , rises first and then abruptly decays in response to viscosity changes. The overall effect of polymerization is a decrease in the volumetric coefficient, $K_m A_\beta$, with further reaction progress. The following equation was developed for the overall volumetric mass transfer coefficient

$$K_m A_\beta = f_k [d + (1 - p)^m] \quad (4.8)$$

as a function of the degree of polymerization p in order to fit the thermogravimetric data [32]. In Equation (4.8) p is the degree of polymerization; f_k , d , and m are empirical parameters.

In order to characterize the overall volumetric mass transfer coefficient, thermogravimetric (TGA) weight loss experiments were designed and executed. When several layers of prepreg are laid up

and analyzed in vacuum using TGA, considerable lofting occurs in the aluminum sample pan. This change in thickness is caused by trapped bubbles, which are developing between the prepreg plies. Figure 4.17a illustrates a sample preparation method which eliminates this problem. The prepreg sample was punched out with a die whose diameter of 6.5 mm is almost exactly that of the pan. Three plies were unidirectionally laid in the sample pan and the edges crimped down to hold the plies down. Figures 4.18 to 4.24 represent the series of TGA experiments utilized to determine the mass transfer function. The idea was to adjust the mass transfer function to match the predicted total flux of volatiles with the comparable experimental TGA data for the total removal rate of volatiles throughout the heating rate and pressure ranges of interest. The pressure referred to here is that above the laminate during the measurements, which would be that under the vacuum bag in the autoclave.

At a heating rate of 0.5°C/min and pressures of 20 Torr and 50 Torr (Figures 4.18 and 4.19), the match between the model and experimental data is quite good after adjustment of the mass transfer coefficient. However, at 2°C/min (Figures 4.20 and 4.21) and 4°C/min (Figures 4.22 and 4.23), the predicted removed mass of volatiles is a little larger (10 and 16% respectively) than indicated by the experiment. The sum of the components appears to add up to a total greater than is measured experimentally. The cause of the problem was the sample preparation technique. With increasing heating rate in high vacuum, bubbles that do not disengage from the sample surface also retard subsequent evaporation of volatiles [33]. This causes the measured experimental weight loss to be lower than would be expected from the reaction stoichiometry. This problem was eliminated by placing a layer of fine steel wool as a bleeder on the surface of the prepreg sandwiches in the aluminum pans (Figure 4.17b). The sharp edges of the steel wool mechanically rupture the bubbles, allowing the gas to escape when it reaches the surface of the laminate. Agreement at the end of the devolatilization is now quite good for the higher heating rates (Figures 4.24 and 4.25), but the experimental data and model-predicted curve diverge during the earlier part of the cure cycle. The model calculations for total cumulative mass fluxes of volatiles always predict two inflection points and thus two separate maxima in individual instantaneous volatile mass fluxes. The cumulative experimental data for total volatile flux indicate two weak inflection points at measurements performed at low heating rates (0.5°C/min), but even then, the evidence is not conclusive. When taken as a whole, the experimental data can be fitted best by the following equation for the volumetric mass transfer coefficient as a function of the degree of polymerization:

$$K_m A_\beta = 1.6 \times 10^{-4} [0.02 + (1 - p)^{1.4}] \quad (4.9)$$

Here it is important to stress that this expression for overall volumetric mass transfer coefficient is entirely empirical.

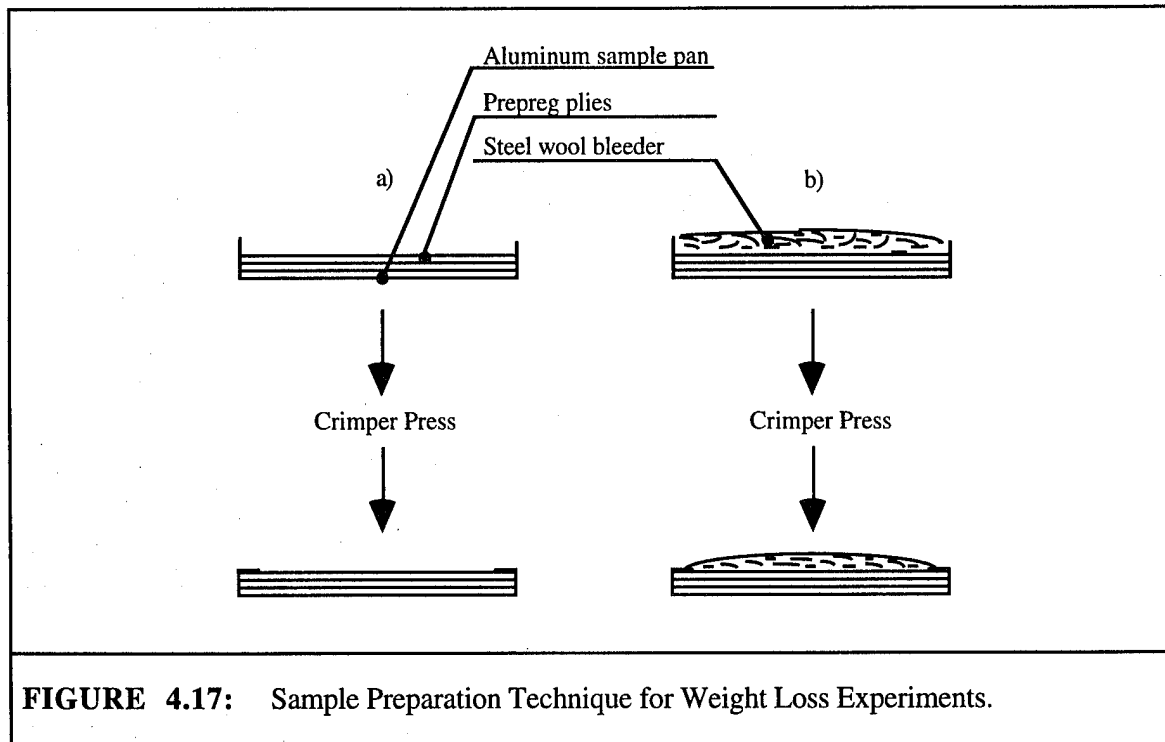


FIGURE 4.17: Sample Preparation Technique for Weight Loss Experiments.

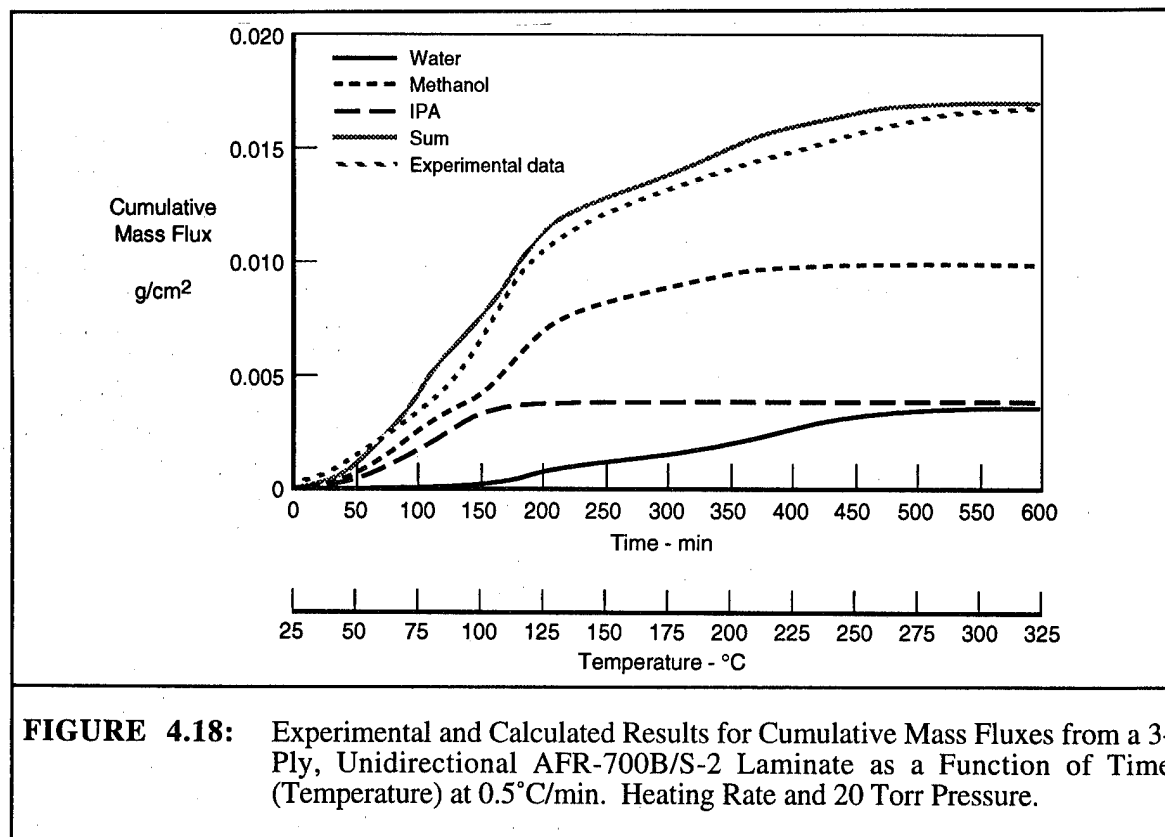


FIGURE 4.18: Experimental and Calculated Results for Cumulative Mass Fluxes from a 3-Ply, Unidirectional AFR-700B/S-2 Laminate as a Function of Time (Temperature) at 0.5°C/min. Heating Rate and 20 Torr Pressure.

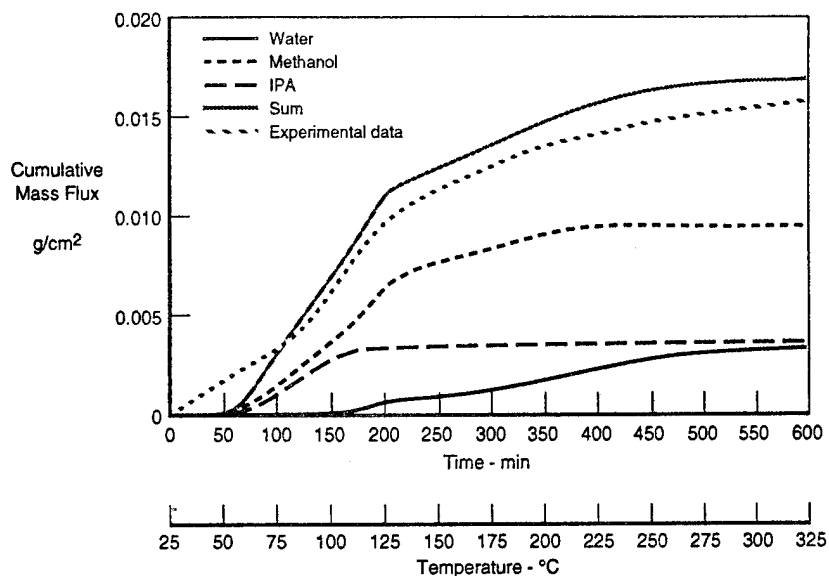


FIGURE 4.19: Experimental and Calculated Results for Cumulative Mass Fluxes from a 3-Ply, Unidirectional AFR-700B/S-2 Laminate as a Function of Time (Temperature) at 0.5°C/min. Heating Rate and 50 Torr Pressure.

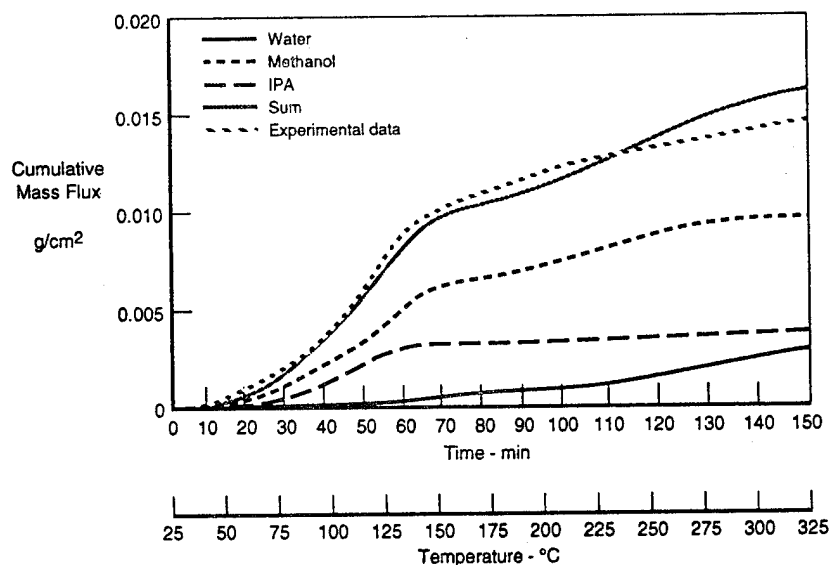


FIGURE 4.20: Experimental and Calculated Results for Cumulative Mass Fluxes from a 3-Ply, Unidirectional AFR-700B/S-2 Laminate as a Function of Time (Temperature) at 2°C/min. Heating Rate and 20 Torr Pressure.

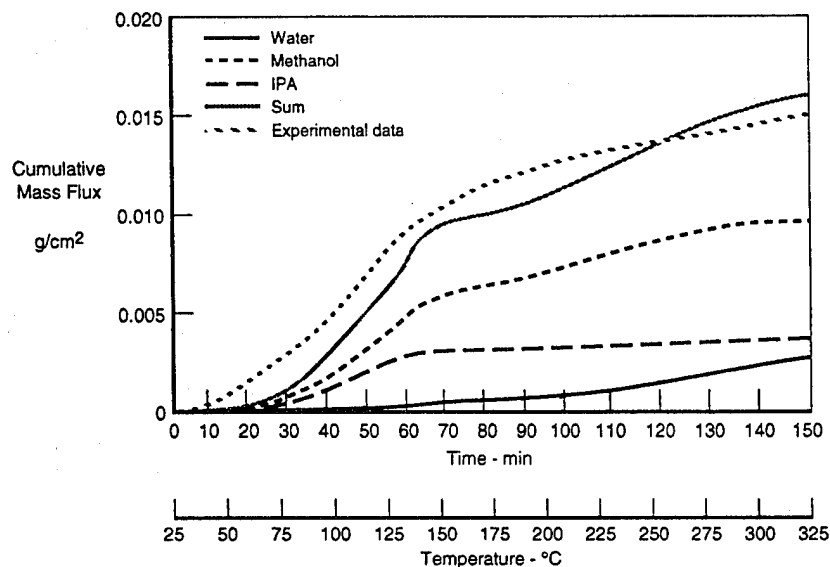


FIGURE 4.21: Experimental and Calculated Results for Cumulative Mass Fluxes from a 3-Ply, Unidirectional AFR-700B/S-2 Laminate as a Function of Time (Temperature) at 2°C/min. Heating Rate and 50 Torr Pressure.

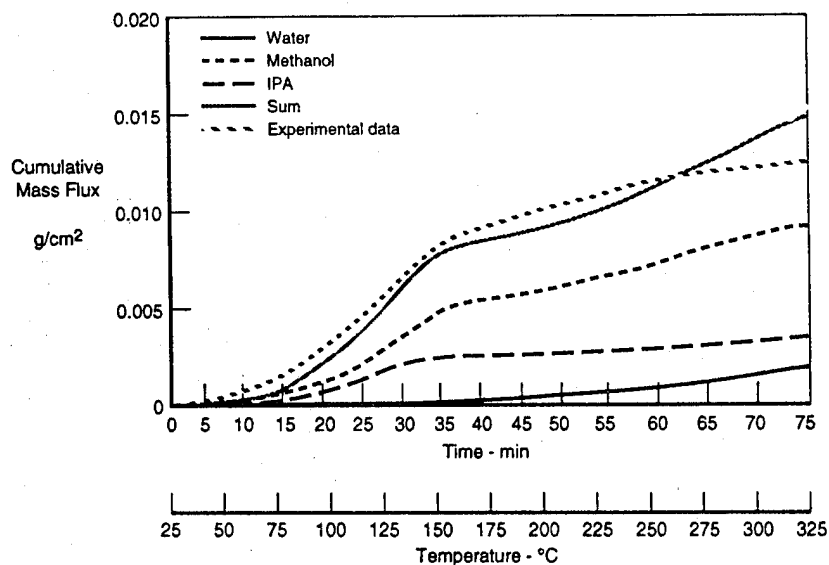


FIGURE 4.22: Experimental and Calculated Results for Cumulative Mass Fluxes from a 3-Ply, Unidirectional AFR-700B/S-2 Laminate as a Function of Time (Temperature) at 4°C/min. Heating Rate and 20 Torr Pressure.

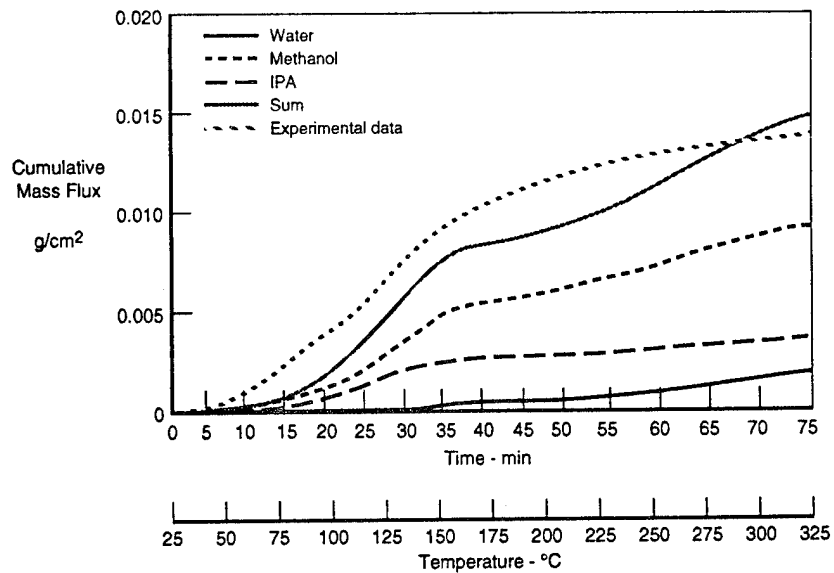


FIGURE 4.23: Experimental and Calculated Results for Cumulative Mass Fluxes from a 3-Ply, Unidirectional AFR-700B/S-2 Laminate as a Function of Time (Temperature) at 4°C/min. Heating Rate and 50 Torr Pressure.

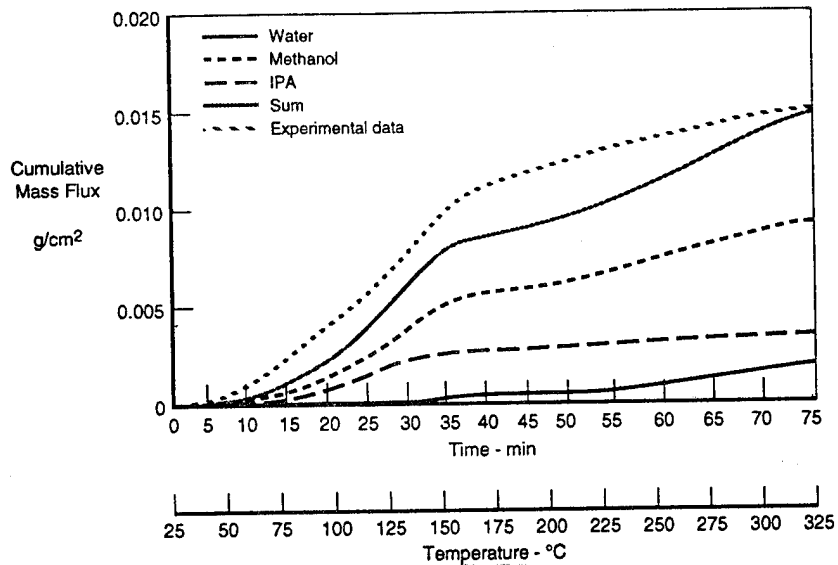


FIGURE 4.24: Experimental and Calculated Results for Cumulative Mass Fluxes from a 3-Ply, Unidirectional AFR-700B/S-2 Laminate as a Function of Time at 2°C/min. Heating Rate, 50 Torr Pressure and Steel Wool Bleeder on the Top.

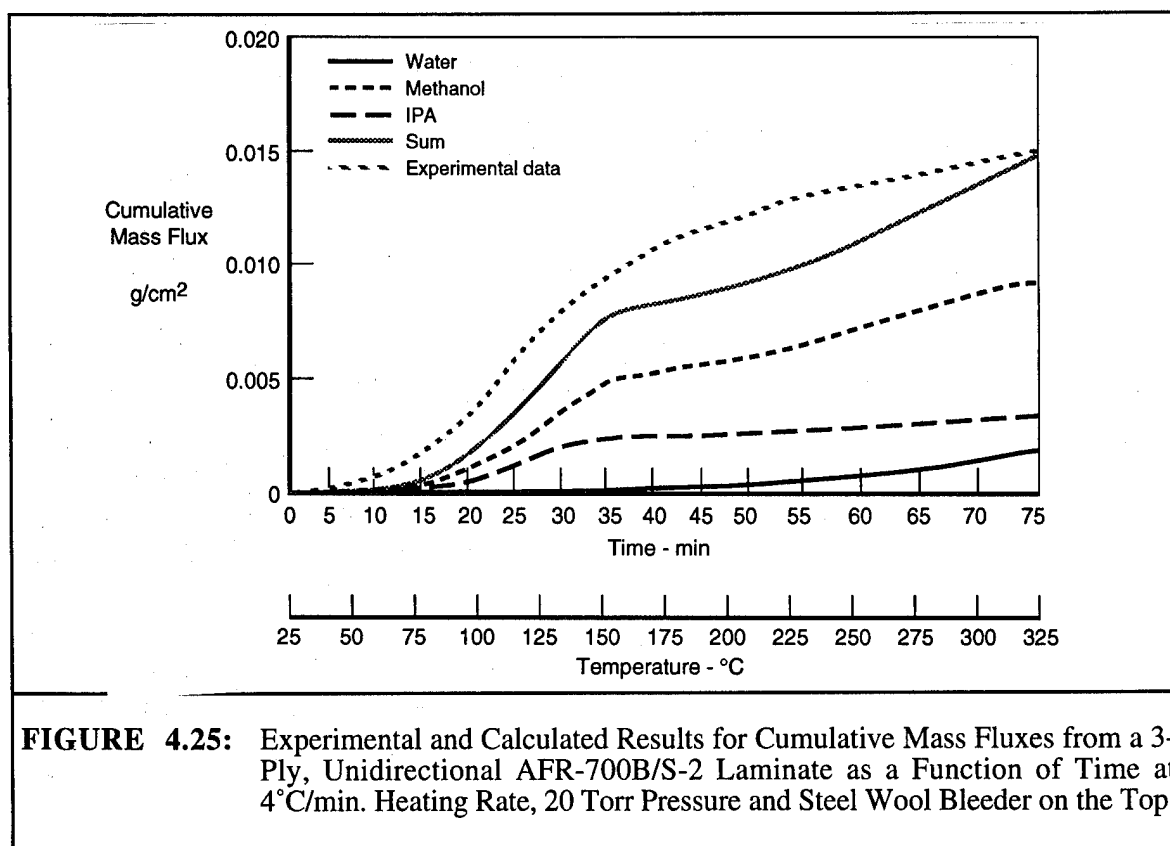


FIGURE 4.25: Experimental and Calculated Results for Cumulative Mass Fluxes from a 3-Ply, Unidirectional AFR-700B/S-2 Laminate as a Function of Time at 4°C/min. Heating Rate, 20 Torr Pressure and Steel Wool Bleeder on the Top.

4.4 Gas Phase Permeability Characterization

As described earlier, an improved devolatilization submodel has been proposed, which yields the pressure distribution inside the composite [32]. Simulations based on this model show that the gas phase permeability, K_g , has little effect on the cumulative mass fluxes, but strongly affects the pressure at the tool side of the laminate [34]. With increasing thickness of the laminate the pressure at the tool side of the laminate increases. The maximum pressure reached at the tool side of the laminate is also shifted to higher temperatures as the heating rate and thickness of the laminate increase.

More so than the kinetics model and the mass transfer coefficient, the gas phase permeability significantly affects the pressure profile through the laminate. Since the permeability has little effect on the cumulative mass fluxes, its value can be determined by fitting the experimental pressure distributions to those predicted by the model. Pressure as a function of temperature (time) was monitored at a point midway between the tool surface and the laminate thickness midpoint. The 15 individual prepreg plies (10 x 10 cm in lateral dimension) were laid up unidirectionally on

the smooth tool surface and covered with two layers of bleeder fabric and a caul plate. The constant thickness of the laminate during the pressure measurements was assured by using four adjustable screws fitted between the aluminum caul plate and the top plate of the miniclave (See Figure 4.26). The prepreg lay-up during the experiments was fixed with aluminum clamps which acted as a frame. One-dimensional devolatilization was accommodated by blocking horizontal vapor flow on the side of the laminate with a high temperature silicone sealant (Permatex Ultra Copper Silicone Gasket). The pressure sensor (Kulite High Temperature Miniature Pressure Transducer) was connected to the data acquisition system through the autoclave wall by a vacuum feedthrough connector (Figure 4.26). The pressure sensor was calibrated over the required pressure and temperature range using a standard pressure gauge. For data collection, the Analog Device data acquisition system (Signal Conditioning Modules, A/D Converter, Data Acquisition Board) driven by a personal computer was used. Pressure measurements were reproducible to ± 0.005 atm in the temperature range 22°C to 170°C. The piezoelectric nature of the pressure sensor is suspected to be the cause of disagreement between measured and calculated pressure profiles in the high temperature range (170°C-230°C). Figures 4.27, 4.28 and 4.29 display the result of pressure measurements which were taken at three different heating rates (0.5, 1, and 2°C/min) and at two different pressure levels (20 and 50 Torr). Figures 4.30, 4.31 and 4.32 represent the pressure profiles calculated by the devolatilization model at identical processing conditions. By matching the maximum values of the pressure profiles calculated by the devolatilization model (Figures 4.30, 4.31 and 4.32) with the measured maximum values of the pressure profiles (Figures 4.27, 4.28 and 4.29), the optimal value of gas phase permeability was found to be $K_{\gamma} = 1.1 \times 10^{-5} \left(\frac{\text{dyne}}{\text{atm}} \right)$. The maximum pressure at the tool side of the laminate heated at a 1°C/min heating rate and a pressure of 20 Torr increases from 0.15 atm to 0.165 atm as the gas phase permeability value is decreased to the above new value from the previously used value of $K_{\gamma} = 1.3 \times 10^{-5} \left(\frac{\text{dyne}}{\text{atm}} \right)$.

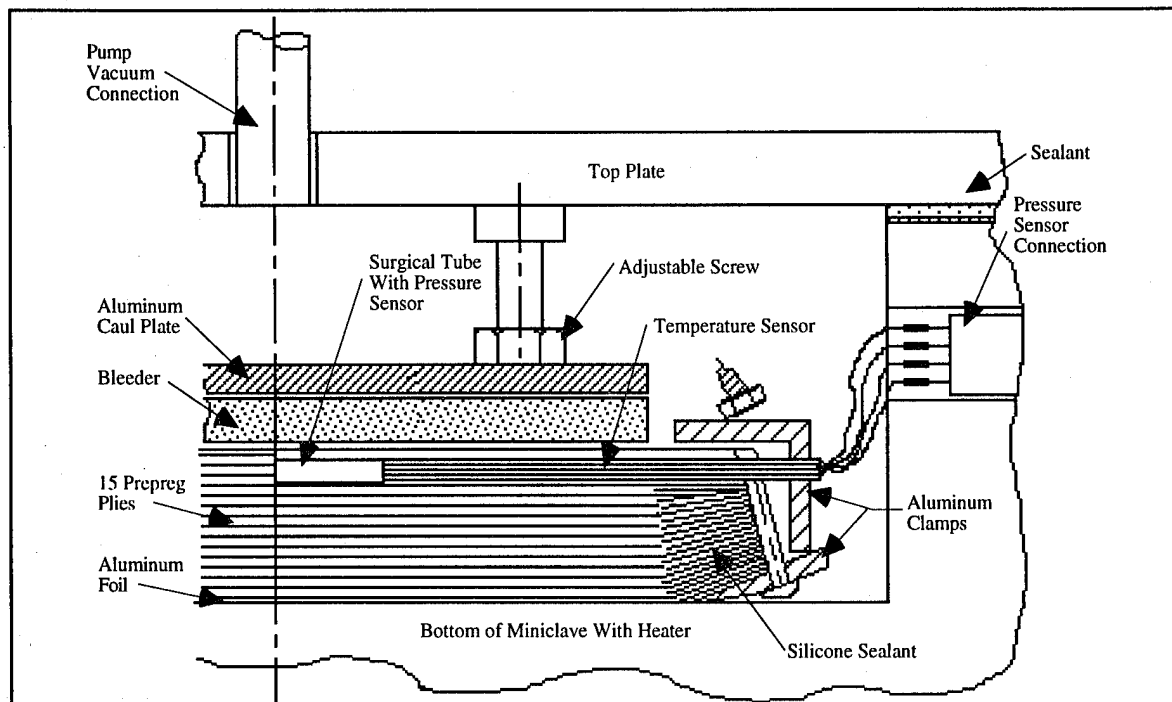


FIGURE 4.26: Schematic of the Mounting of Pressure Sensor and Laminate in Miniclave. Pressure Sensor is Shown Mounted at the Bleeder Side (Top) of the Laminate.

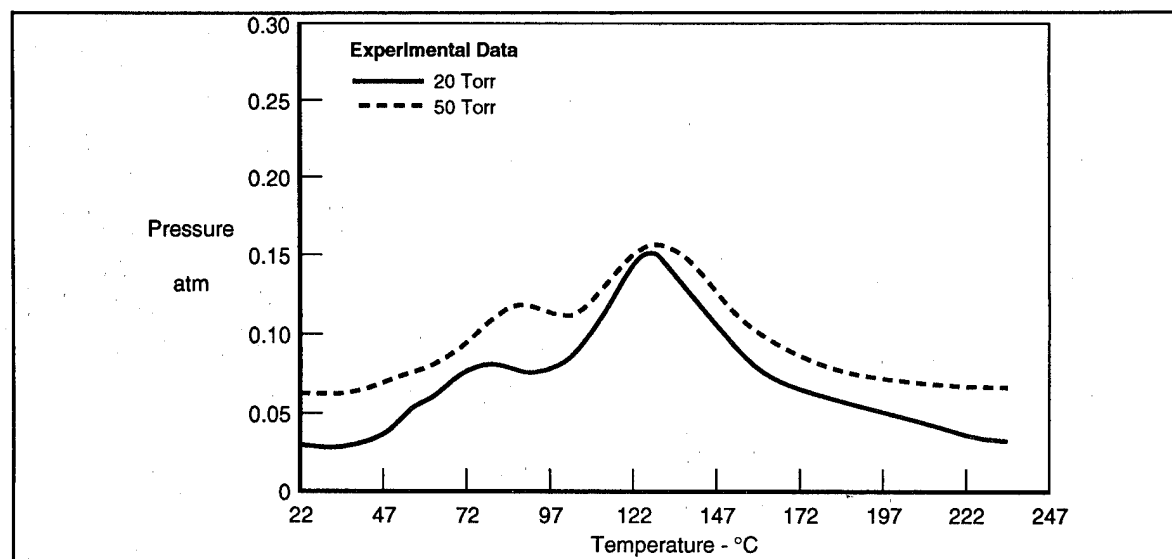


FIGURE 4.27: Measured Pressure Profiles as a Function of Temperature at a Point Midway Between the Tool Surface and the Laminate Thickness Midpoint at the Laminate Center for a 15-Ply, Unidirectional AFR-700B/S-2 Laminate at 0.5°C/min. Heating Rate and Pressures of 20 and 50 Torr.

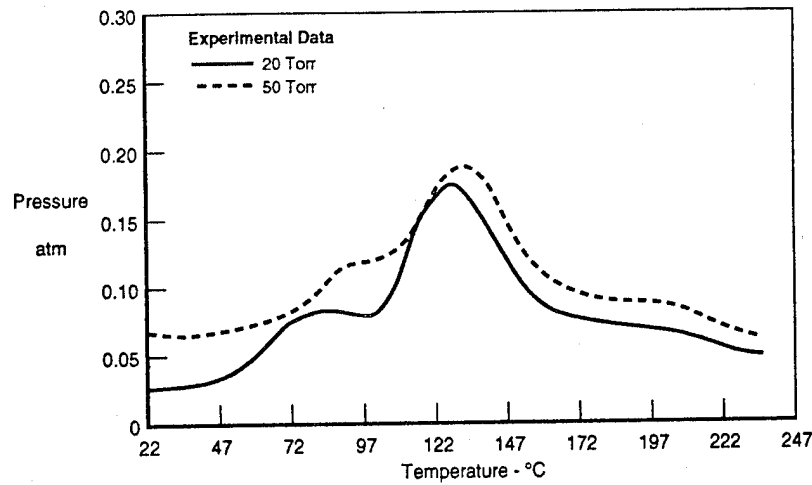


FIGURE 4.28: Measured Pressure Profiles as a Function of Temperature at a Point Midway Between the Tool Surface and the Laminate Thickness Midpoint at the Laminate Center for a 15-Ply, Unidirectional AFR-700B/S-2 Laminate at 1°C/min. Heating Rate and Pressures of 20 and 50 Torr.

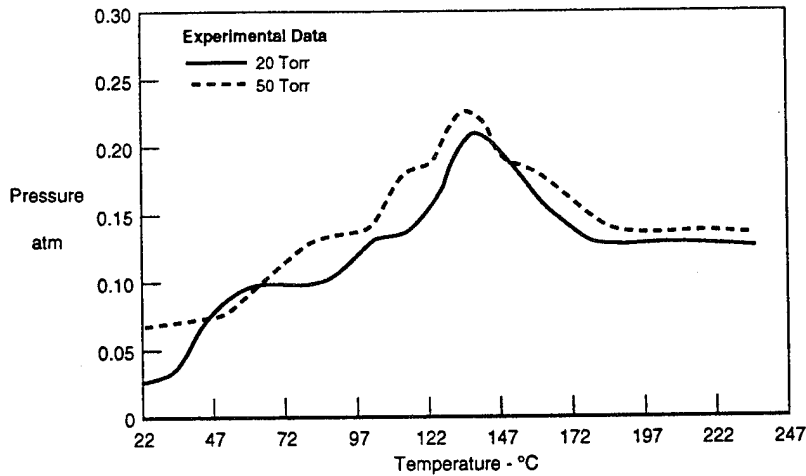


FIGURE 4.29: Measured Pressure Profiles as a Function of Temperature (Time) at a Point Midway Between the Tool Surface and the Laminate Thickness Midpoint at the Laminate Center for a 15-Ply, Unidirectional AFR-700B/S-2 Laminate at 2°C/min. Heating Rate and Pressures of 20 and 50 Torr.

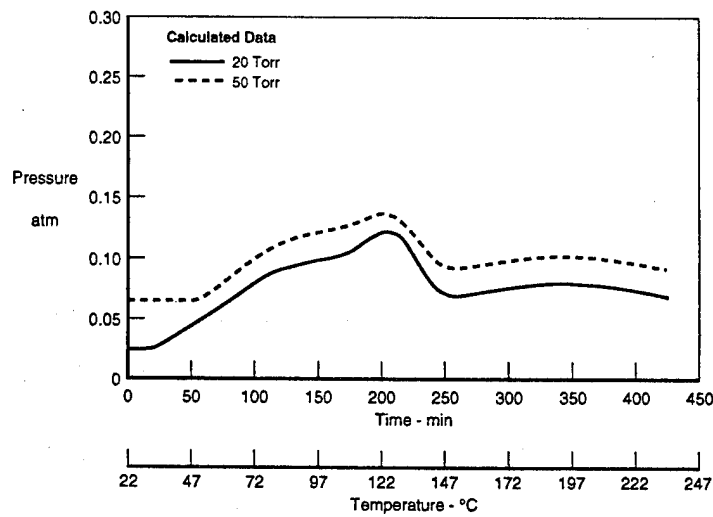


FIGURE 4.30: Calculated Pressure Profiles as a Function of Temperature (Time) at a Point Midway Between the Tool Surface and the Laminate Thickness Midpoint for a 15-Ply, Unidirectional AFR-700B/S-2 Laminate at 0.5°C/min. Heating Rate and Pressures of 20 and 50 Torr.

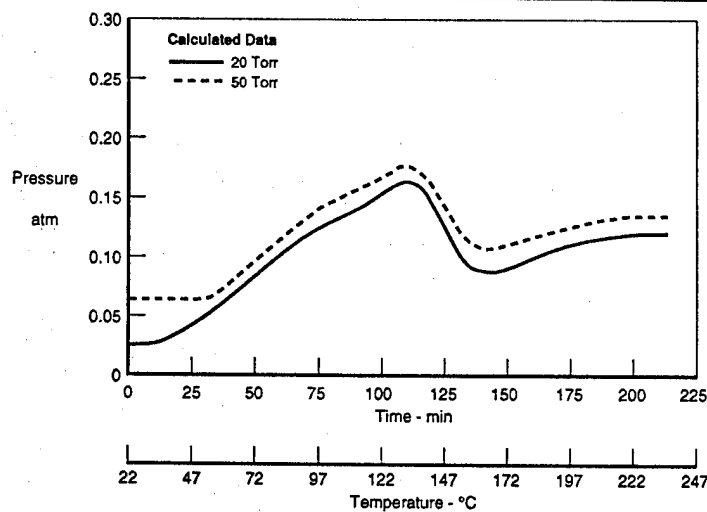


FIGURE 4.31: Calculated Pressure Profiles as a Function of Temperature (Time) at a Point Midway Between the Tool Surface and the Laminate Thickness Midpoint for a 15-Ply, Unidirectional AFR-700B/S-2 Laminate at 1°C/min. Heating Rate and Pressures of 20 and 50 Torr.

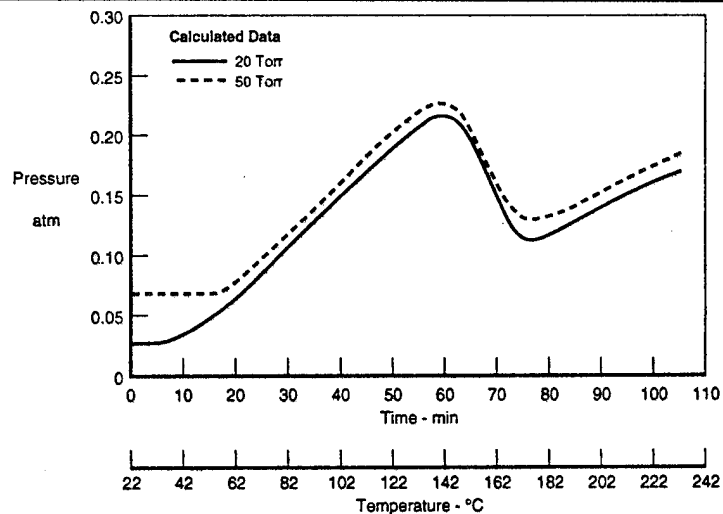


FIGURE 4.32: Calculated Pressure Profiles as a Function of Temperature (Time) for a 15-Ply, Unidirectional AFR-700B/S-2 Laminate at a Point Midway Between the Tool Surface and the Laminate Thickness Midpoint at 2°C/min. Heating Rate and Pressures of 20 and 50 Torr.

5.0 MODEL VERIFICATION

Summarizing the devolatilization model described earlier, equations have been developed for the energy balance, liquid phase mass balance, gas phase mass balance, and mass balances for solvent, by-products, and active groups in the monomer and polymer chains, together with the gas molar fraction equation. To these ten coupled partial differential equations have been added expressions for the evaporation rate of each volatile component and for gas phase velocity. Additional inputs were obtained for physical properties including density, heat capacity and thermal conductivity. Lacking any good fundamental data on the AFR-700B system, necessary critical inputs for the kinetics and mass transfer coefficient were developed by empirically fitting a variety of independent calorimetric and weight loss experimental results to the simulations of the cure cycle that includes polymerization kinetics and evolution of volatiles. The pressure variation with time was measured on the tool side at the center of the laminate. By matching these measured pressure profiles with profiles calculated by the devolatilization model for identical process conditions, the gas phase permeability was estimated.

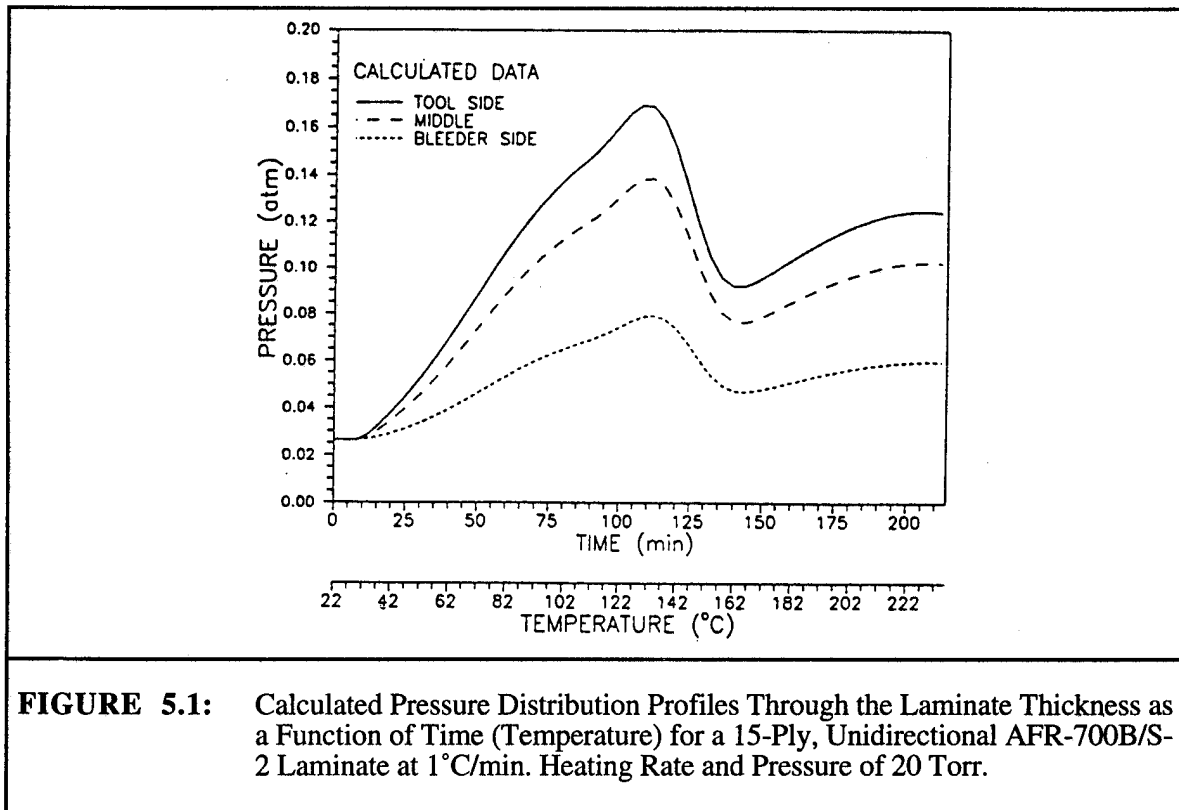
The simulation results of the devolatilization submodel have been partially reported elsewhere [34]. The model predicts the total and individual volatile mass fluxes, as well as the temperature and pressure profiles through the laminate as a function of the initial laminate thickness and the temperature and pressure cycles employed during autoclave processing.

5.1 Gas Pressure Measurements

The devolatilization model was verified by comparing model simulations for the maximum magnitudes of the pressure distribution through the laminate thickness with the maximum magnitudes of the pressure profiles measured. The pressure sensors were located at the vertical center line along the laminate thickness (tool side, middle, and bleeder side of the laminate).

Figures 5.1, 5.2, 5.3 and 5.4 present the model calculations of pressure distribution through the laminate thickness as a function of time at a bleeder pressure of 20 Torr for two different heating rates (1°C and 2°C/min.) and two laminate thicknesses (15 plies and 29 plies). Figures 5.5, 5.6, 5.7, and 5.8 show measured pressure distributions along the laminate thickness for the identical processing parameters (heating rate, vacuum level, thickness of laminate). Good agreement between measured and predicted maxima in pressure profiles was obtained for low heating rates and for the thinner laminate (15 plies). The agreement for the highest heating rate and thickest laminate (29 plies) is not as good, but is reasonable.

By increasing heating rates from 1°C/min. to 2°C/min. at identical system pressures for a 15-ply laminate, the average measured maximum in the pressure profile through the laminate is increased by 38 Torr in magnitude and is shifted by 7°C to a higher temperature. More volatiles are developed in the laminate with increasing heating rate, and the fast temperature increase leaves insufficient time for the volatiles to leave the laminate. The same increase in heating rates for a 29-ply laminate causes the shift in the measured maximum of the pressure peak and the increase in value to be more pronounced (an average 11°C temperature shift and 53 Torr pressure increase). With increasing thickness more volatiles are developed and they have longer and more tortuous escape paths to reach the laminate surface. The presented comparison between the model prediction and measured values of pressures indicates that the model can quantitatively predict maxima in pressure profiles for different laminate thicknesses and heating rates.



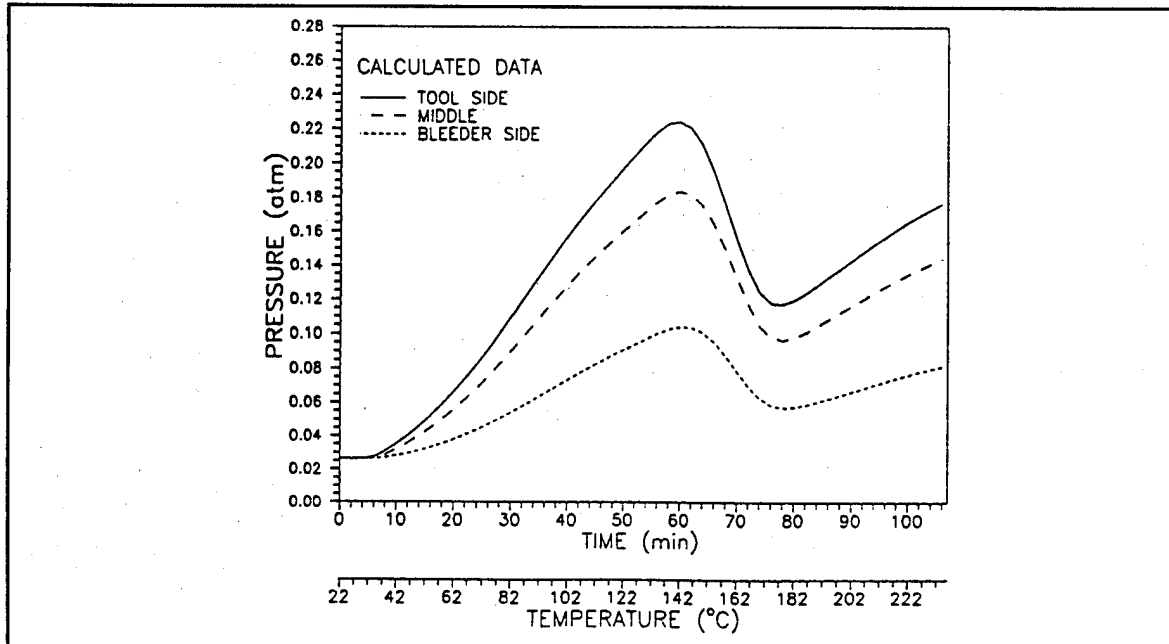


FIGURE 5.2: Calculated Pressure Distribution Profiles Through the Laminate Thickness as a Function of Time (Temperature) for a 15-Ply, Unidirectional AFR-700B/S-2 Laminate at 2°C/min. Heating Rate and Pressure of 20 Torr.

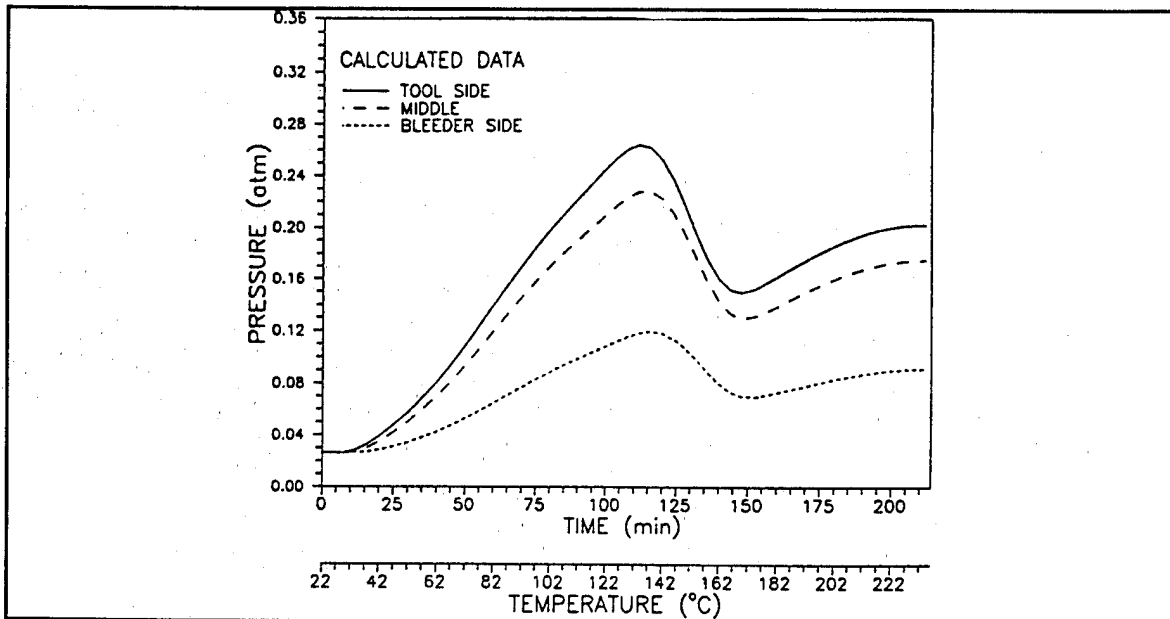


FIGURE 5.3: Calculated Pressure Distribution Profiles Through the Laminate Thickness as a Function of Time (Temperature) for a 29-Ply, Unidirectional AFR-700B/S-2 Laminate at 1°C/min. Heating Rate and Pressure of 20 Torr.

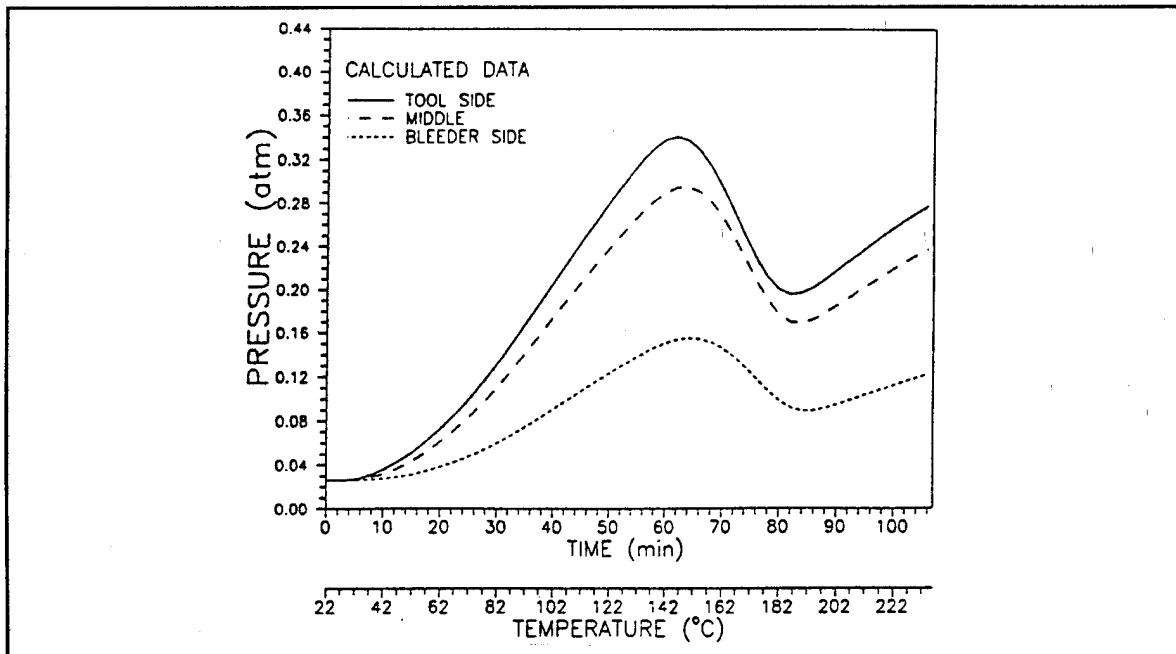


FIGURE 5.4: Calculated Pressure Distribution Profiles Through the Laminate Thickness as a Function of Time (Temperature) for a 29-Ply, Unidirectional AFR-700B/S-2 Laminate at 2°C/min. Heating Rate and Pressure of 20 Torr.

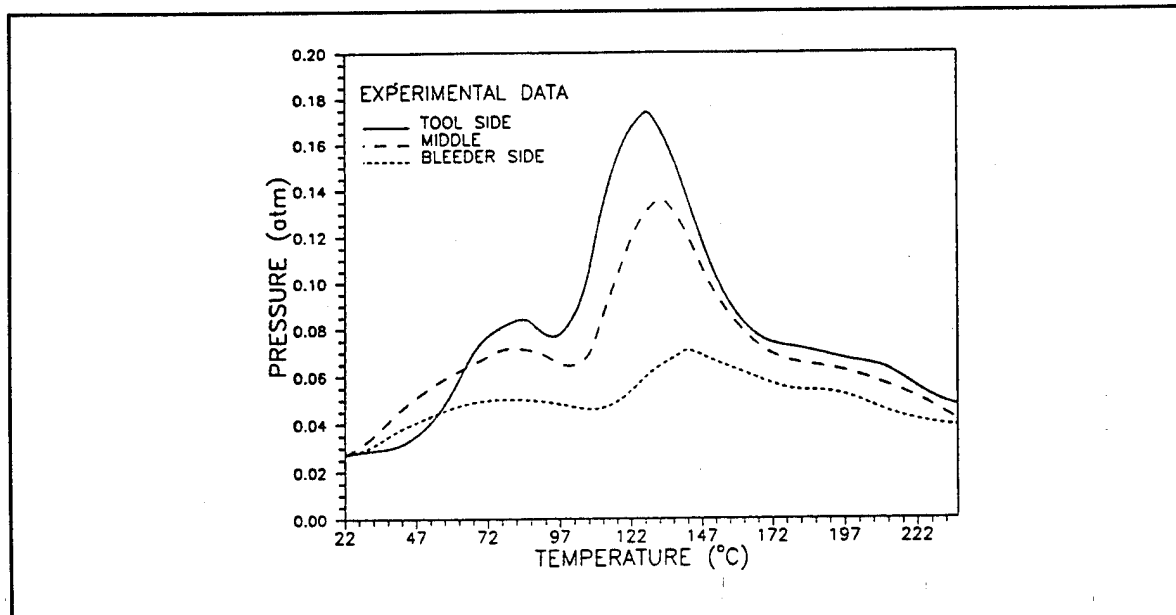


FIGURE 5.5: Measured Pressure Distribution Profiles Through the Laminate Thickness as a Function of Temperature for a 15-Ply, Unidirectional AFR-700B/S-2 Laminate at 1°C/min. Heating Rate and Pressure of 20 Torr.

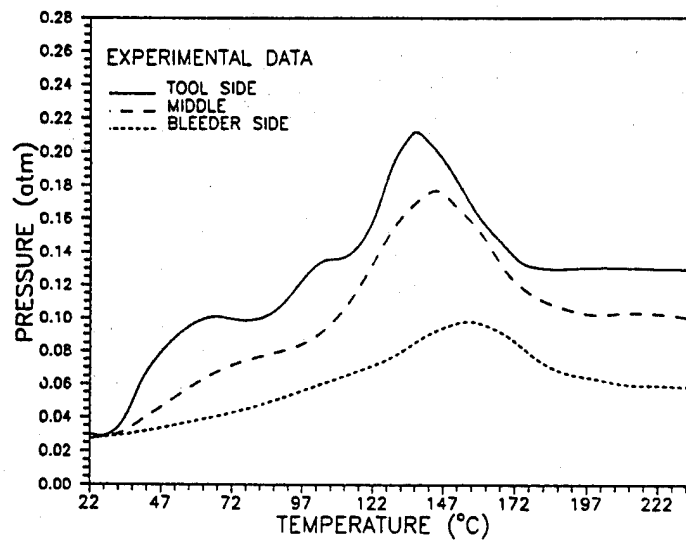


FIGURE 5.6: Measured Pressure Distribution Profiles Through the Laminate Thickness as a Function of Temperature for a 15-Ply, Unidirectional AFR-700B/S-2 Laminate at 2°C/min. Heating Rate and Pressure of 20 Torr.

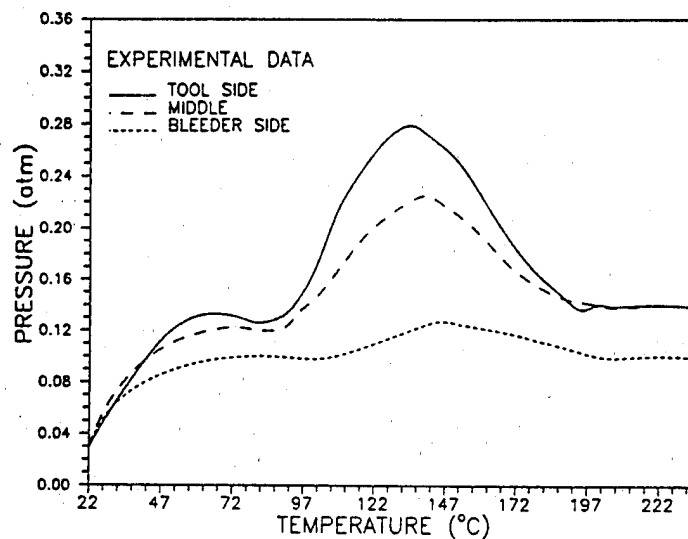
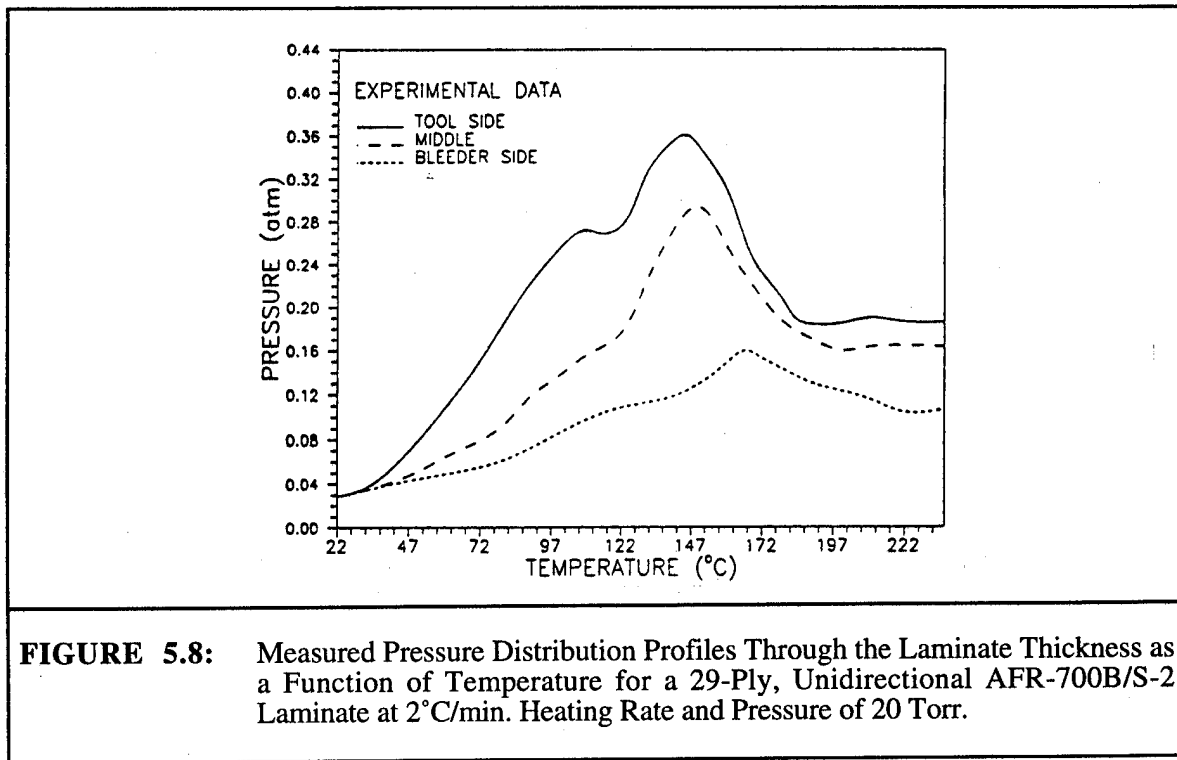


FIGURE 5.7: Measured Pressure Distribution Profiles Through the Laminate Thickness as a Function of Temperature for a 29-Ply, Unidirectional AFR-700B/S-2 Laminate at 1°C/min. Heating Rate and Pressure of 20 Torr.

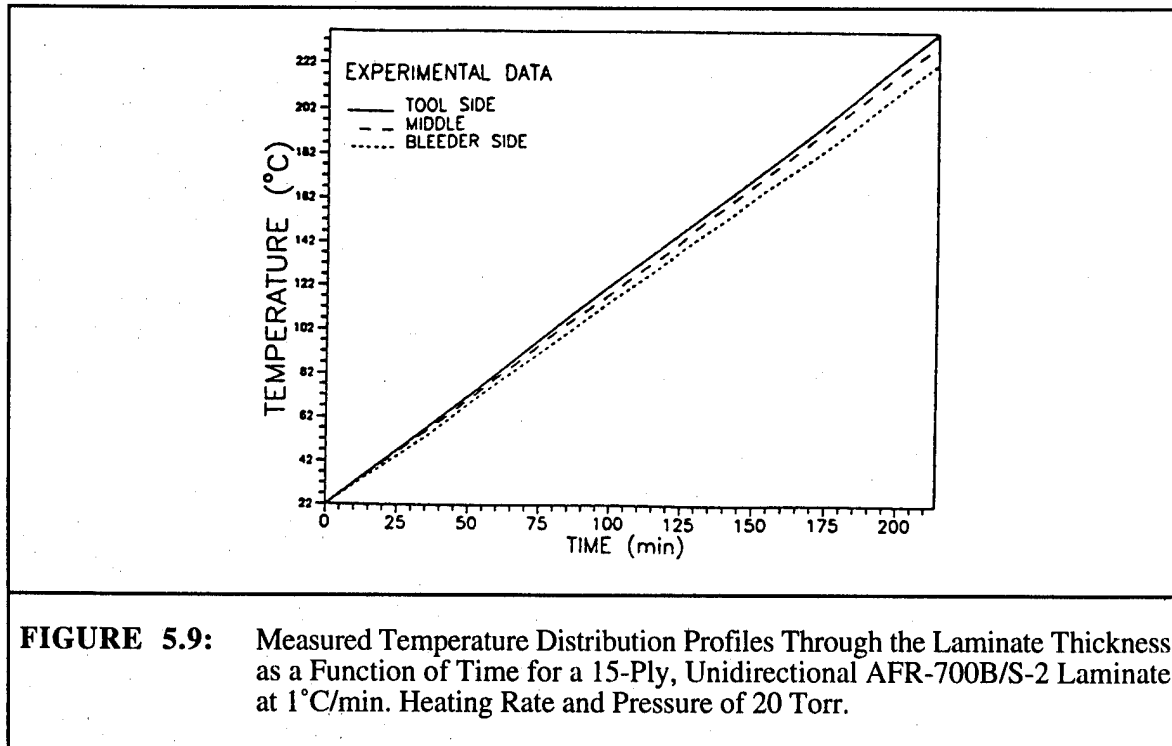


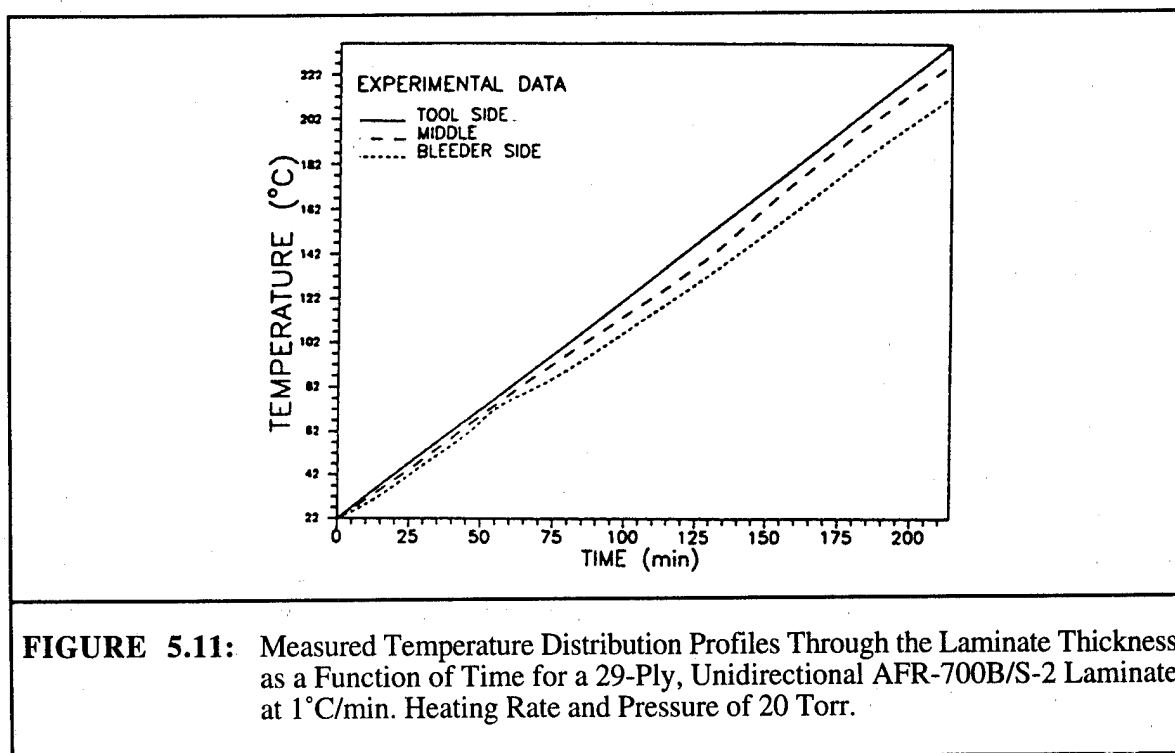
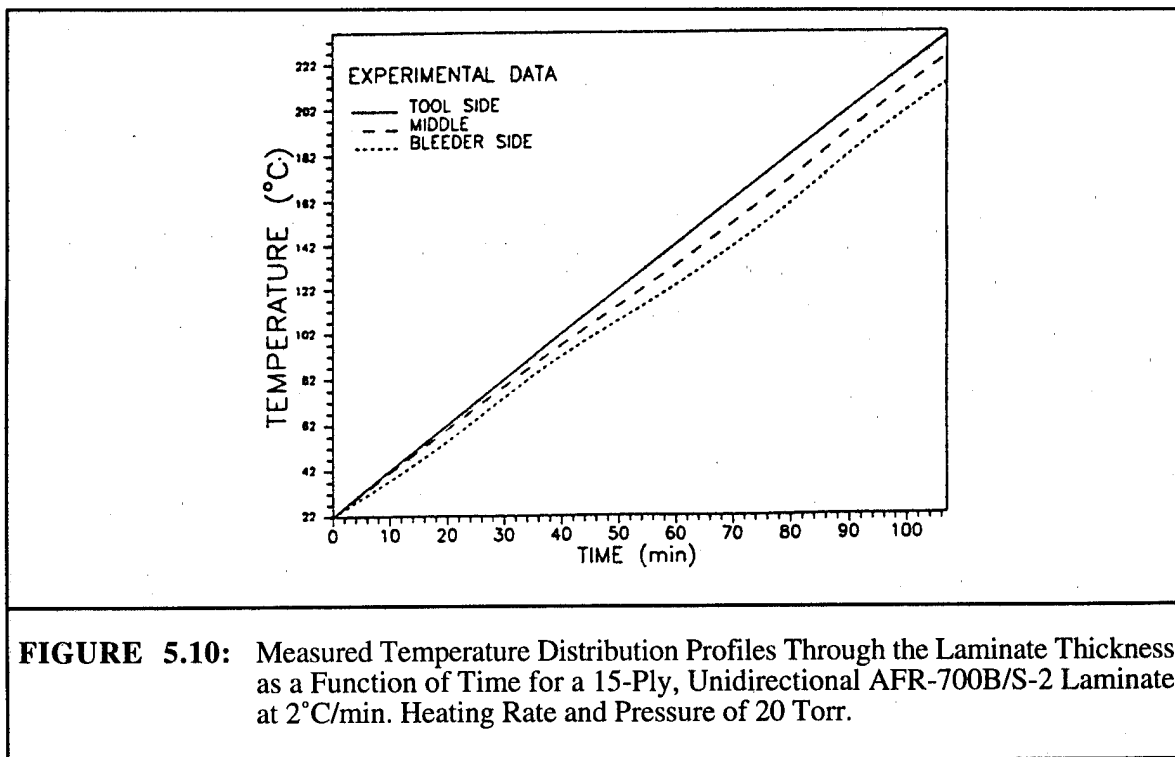
5.2 Temperature Measurements

The temperature as a function of time was measured at three points (tool side, middle, and bleeder side) through the laminate thickness (Figures 5.9, 5.10, 5.11 and 5.12) at a system pressure of 20 Torr for two different heating rates (1°C and 2°C/min.) and two laminate thicknesses (15 plies and 29 plies).

The model was then used to fit all experimental data for identical processing conditions (heating rate, system pressure, laminate thickness) to determine a value of the topological parameter r in the laminate volume-averaged thermal conductivity equation (equation (2.6)). Figures 5.13, 5.14, 5.15 and 5.16 show model calculations for a value of $r = -0.4$. All model simulations which were presented and discussed previously were performed with this value of the topological parameter, n . Excellent agreement (within 1-2°C) with experimental temperature profiles was obtained for low heating rates (1°C/min.) and small laminate thicknesses (15 plies) at the end of the cure process. The highest heating rate (2°C/min.) and the thickest laminate (29 plies) produced agreement within 2-4°C.

The temperature difference between the tool surface and the bleeder side of the laminate at the end of the cure process increases with heating rate and laminate thickness. For a 15-ply laminate heated at 1°C/min. heating rate, the maximum measured temperature difference between the tool surface and the bleeder side of laminate at the end of the cure process was 14°C compared to a predicted value of 13°C. For a 29-ply laminate heated at 2°C/min. heating rate, the maximum measured temperature difference was 36°C compared to a predicted value of 39°C. The model can quantitatively predict the temperature profiles through the laminate for different laminate thicknesses and heating rates.





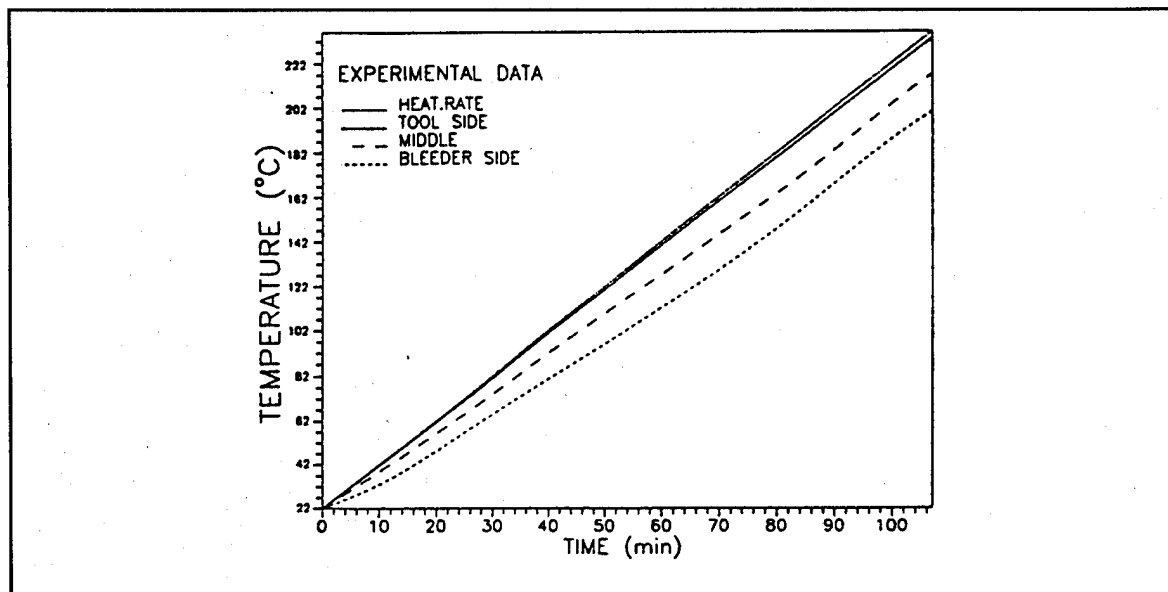


FIGURE 5.12: Measured Temperature Distribution Profiles Through the Laminate Thickness as a Function of Time for a 29-Ply, Unidirectional AFR-700B/S-2 Laminate at 2°C/min. Heating Rate and Pressure of 20 Torr.

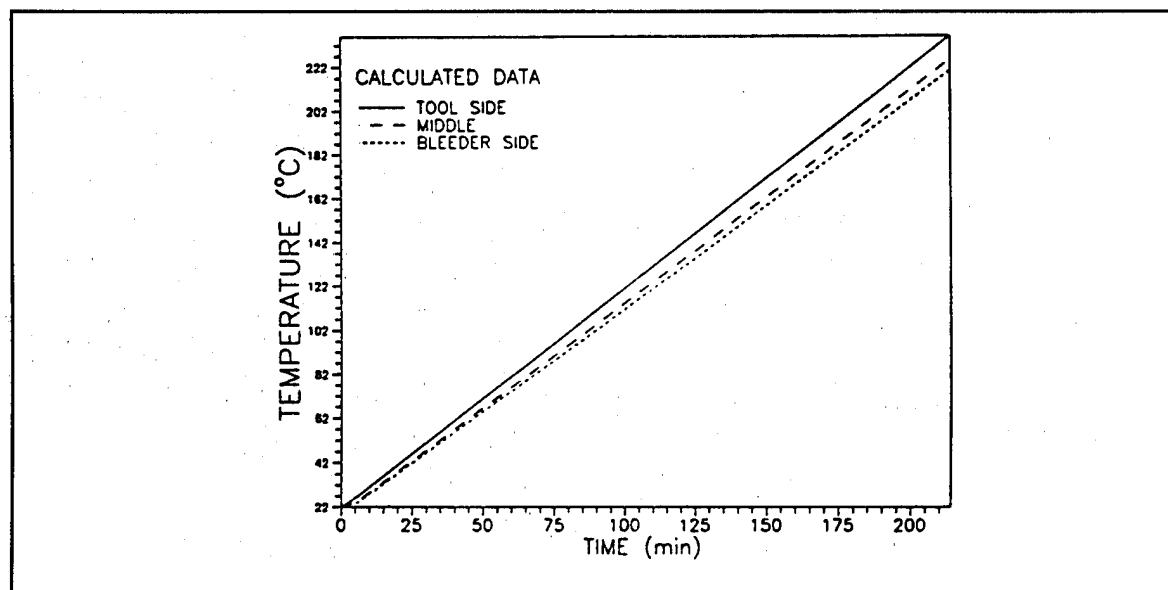
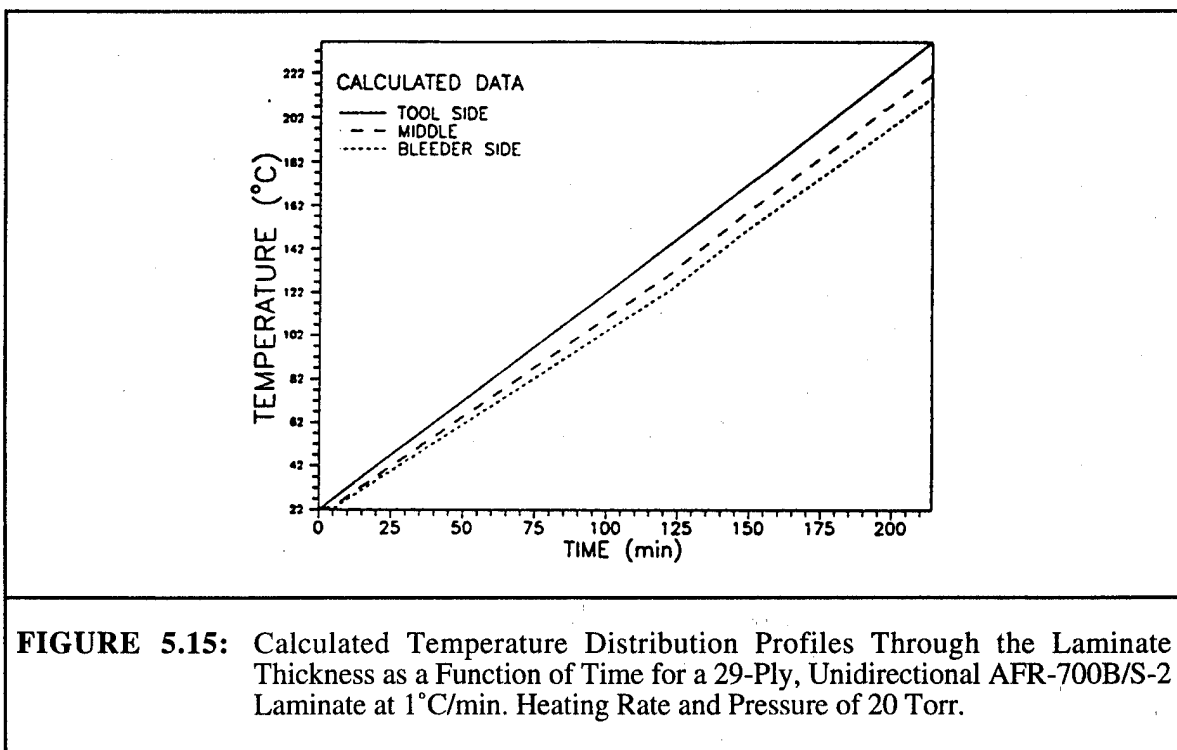
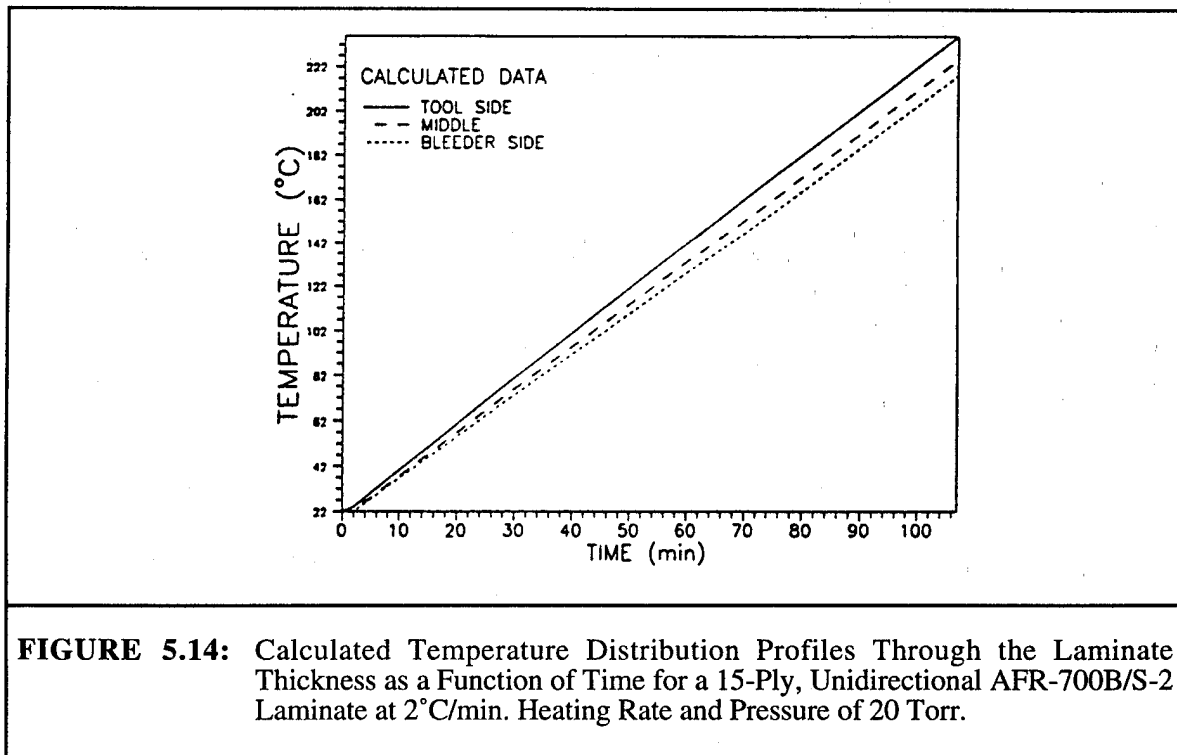


FIGURE 5.13: Calculated Temperature Distribution Profiles Through the Laminate Thickness as a Function of Time for a 15-Ply, Unidirectional AFR-700B/S-2 Laminate at 1°C/min. Heating Rate and Pressure of 20 Torr.



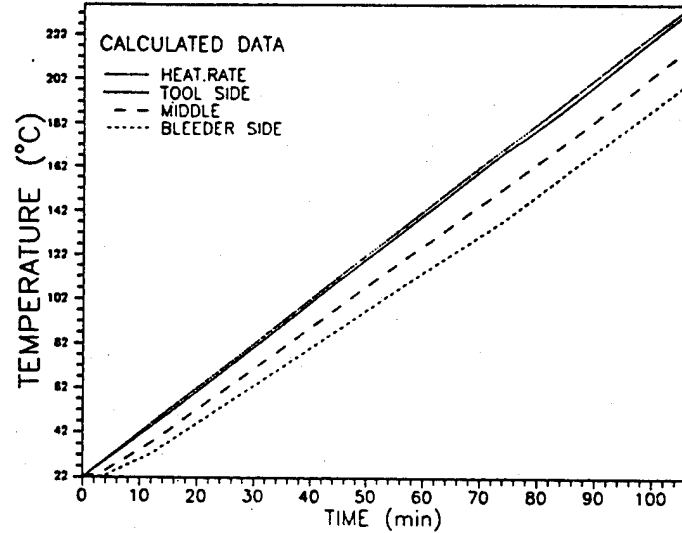


FIGURE 5.16: Calculated Temperature Distribution Profiles Through the Laminate Thickness as a Function of Time for a 29-Ply, Unidirectional AFR-700B/S-2 Laminate at 2°C/min. Heating Rate and Pressure of 20 Torr.

6.0 EFFECT OF PROCESS VARIABLES ON DEVOLATILIZATION

6.1 Ionic Viscosity as a Measure of Devolatilization

Figure 6.1 shows the effect of pressure (20, 50, and 760 Torr) on the ionic viscosity versus time profiles for a heating rate of 1°C/min. and composite thickness of 2 mm. Figures 6.2 and 6.3 represent model simulations for the volatile species concentrations in the liquid phase and for the individual instantaneous volatile mass fluxes computed for the identical processing conditions at which dielectric measurements were made.

During the initial heating at atmospheric pressure, the decrease in the ionic viscosity (Figure 6.1) reflects the decrease in the resin viscosity due to dissolving of the monomer into the original prepreg solvent (methanol and isopropanol). At about 80°C, reaction starts within the liquid phase of aromatic dianhydrides, aromatic diamines and solvents, causing the ionic viscosity to stabilize. With rising temperature, a steep increase in the ionic viscosity is associated with increasing molecular weight through amidization and attendant imidization. During this time a relatively large volume of original solvent and products of polycondensation reaction (methanol and water) vaporize (Figure 6.3). The gas bubbles which are generated rupture on the surface of the prepreg plies. The ionic viscosity rises until about 140°C where it reaches a maximum value and where the gas bubbles in the resin are likely to become immobilized. The bubbles trapped between the prepreg plies cause the thickness of the laminate to increase, a process called "lofting." After this point the resin dries to a powder consistency and the ionic viscosity decreases slightly. The oscillation of the ionic viscosity curve around its slightly decreasing value at this temperature indicates bad sensor contact with dry prepreg resin at this stage of the reaction. Relatively large amounts of residual solvent and polycondensation reaction by-products still vaporize at this final stage of the imidization reaction because the resin is in a dry powder form, making volatile removal still possible. With heating up to 300°C devolatilization is essentially completed and the ionic viscosity starts to drop as the increasing resin temperature passes its glass transition point. This improves sensor contact with the resin as indicated by a return to smooth ionic viscosity curves. Further heating causes the ionic viscosity to decrease further and leads to the occurrence of a softening region in the processing cycle. High pressure applied during this time tends to rupture trapped bubbles and squeeze the resin out in order to minimize void content, thereby causing the laminate thickness to decrease.

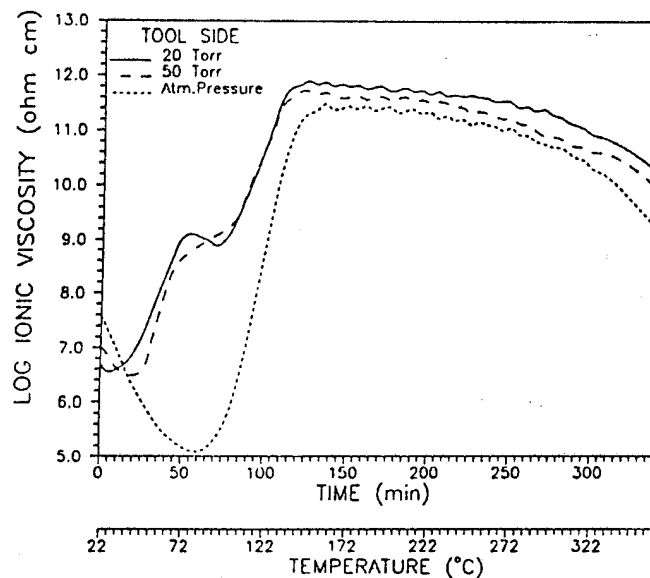


FIGURE 6.1: Measured Effect of Pressure (20, 50, and 760 Torr) on the Ionic Viscosity-Time (Temperature) Profiles for a 6-Ply, Unidirectional AFR-700B/S-2 Laminate at 1°C/min Heating Rate.

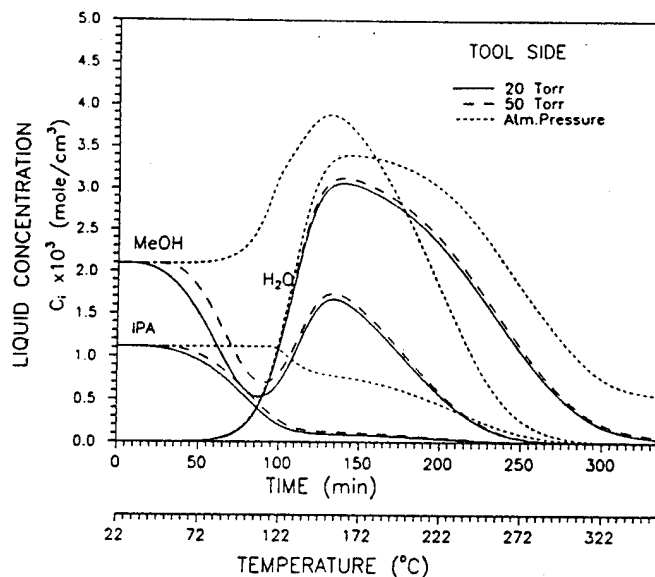
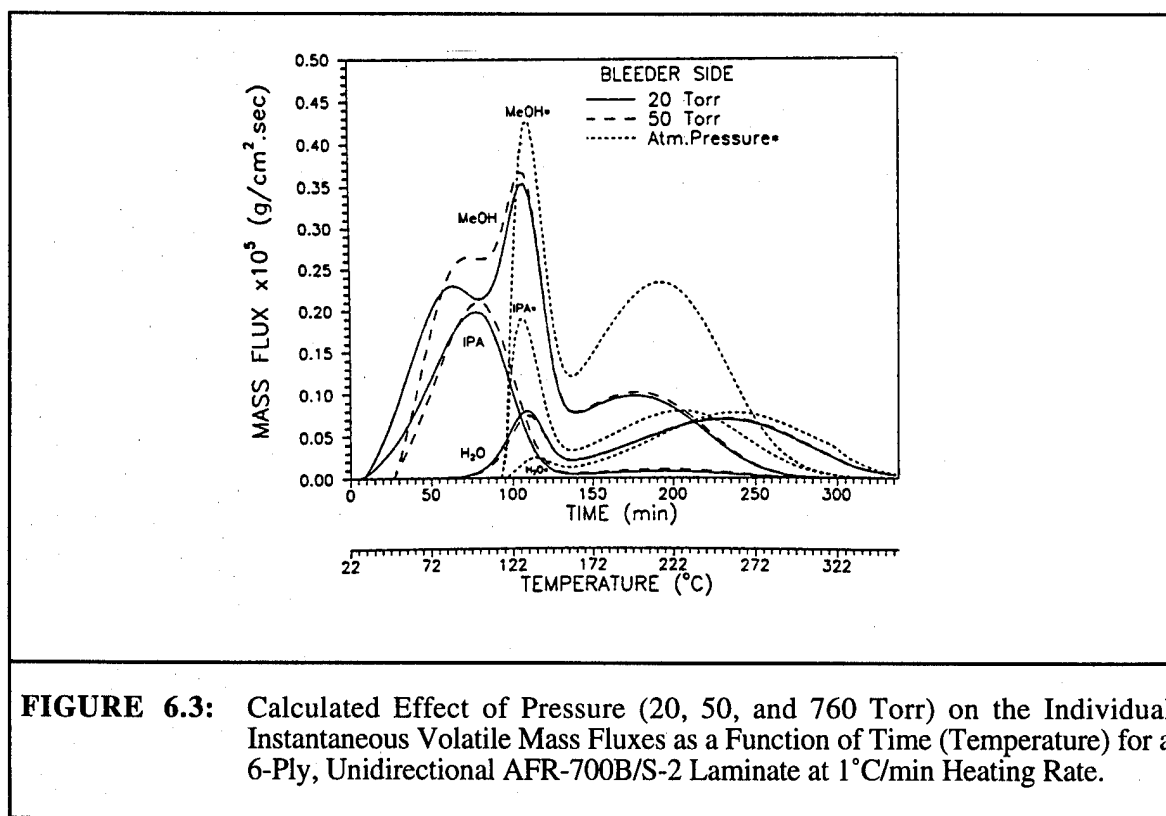


FIGURE 6.2: Calculated Effect of Pressure (20, 50, and 760 Torr) on the Concentrations of Volatile Species in the Liquid Phase as a Function of Time (Temperature) for a 6-Ply, Unidirectional AFR-700B/S-2 Laminate at 1°C/min Heating Rate.



Experiments performed at reduced pressures (20 and 50 Torr) revealed two minima in the measured ionic viscosity (Figure 6.1). With decreasing pressure the first minimum occurs at a lower temperature, but the absolute value of the ionic viscosity increases. This happens because the volatiles from the original prepreg solvent (methanol and isopropanol) are now removed more quickly from the prepreg resin because the driving force for volatiles removal increases with decreasing pressure. The amidization reaction thus starts at a lower temperature, causing the molecular weight to build up more quickly. The second minimum of the ionic viscosity (Figure 6.1) reflects the maximum devolatilization of the original prepreg solvent together with the starting devolatilization of the polycondensation reaction by-products (methanol and water) (Figure 6.3). During this time, gas bubbles are generated and rupture on the laminate surface (see Figure 4.13). Model simulation for the individual instantaneous volatile mass fluxes performed at atmospheric pressure (Figure 6.3) indicates that methanol has a double maximum in the differential flux most likely because it is present as a solvent in the initial prepreg and is also produced during the reaction. Water also exhibits two maxima, the second at a temperature close to 240°C. The reason for the first maximum lies in the model calculations for mass flow rate (equation 2.24). The frequency part of the equation, $K_m A_\beta$, (first term on the right side of the equation 2.24) given by

equation 3.6 reduces the mass transfer coefficient dramatically once 140°C is reached. However, the subsequent rise in temperature increases the driving force for devolatilization (second term on the right side of equation 2.24), which overcomes the decreasing frequency factor, leading to increased devolatilization and a second maximum. Two similar maxima for water devolatilization at atmospheric pressure were found in TGA mass spectroscopy data from AFR-700B prepreg resin during curing [35]; the first maximum occurred at 130°C and the second at 230°C. The cumulative mass flux measurements (Figures 3.18 to 3.25) presented earlier do not show two apparent inflection points at first glance. However, careful scrutiny of the data slopes does show two inflection points for the 0.5°C/min. heating rate. At higher heating rates the water devolatilization is probably masked by the vaporization of other volatiles. Sufficient data to prove or disprove this are lacking. In the case of the Qualitative Process Automation (QPA) intelligent sensor feedback cure cycle discussed in section 7.1, we can see a discontinuity in the loss factor curve at a temperature where water devolatilization slow down is predicted by the model simulations (Figure 7.2).

6.1.1 Imidization Reaction Characterization

A study of the imidization reaction using IR spectroscopy [10] indicates that the reaction slows down at high temperature. This is explained by a decrease in entropy as a result of solvent devolatilization [36], a decrease in the concentration of the functional groups [37], and by a change in the molecular mobility [38]. A polymer viscosity study based on the experimentally measured relation between the softening temperature and the degree of cyclization shows that the cyclization rate in polyimides is determined by a change in molecular mobility in the glass transition temperature region [39]. A two-step isothermal weight loss study of condensation reaction in polyimides supports the assumption that free motion of molecular chains is frozen at the polymer glass transition temperature [40].

The ionic viscosity (Figure 6.1) and degree of reaction (Figure 4.17) measurements indicate that the polyimidization reaction slows down very rapidly after a temperature of about 155°C is reached. The motion of the molecular polymer chains is fast in the early stage of imidization, but with progress of imidization the molecular chain rigidity increases, as imide rings are formed, and the glass transition temperature of the reacting polymer shifts towards a higher temperature. The imidization thus slows down because of high molecular chain rigidity. When the polymer glass transition temperature reaches the reaction temperature, polymer molecular motion is frozen and the imidization reaction becomes inactive [40]. At this temperature polyimide prepolymers are formed. A continuing increase in temperature causes the resin to soften as the polyimide passes its

glass transition temperature. In this region the Reverse Diels-Alder crosslinking reaction starts (cyclopentadiene is released prior to further participation in the crosslinking reaction), followed by Michael addition crosslinking reaction with increasing temperature [15].

Processing in a vacuum strongly influences the imidization reaction. The removal of solvent volatiles from the liquid phase containing aromatic anhydrides and aromatic diamines starts at lower temperatures, allowing the amidization reaction to start early. It has been previously shown that the fastest polyimidization reaction occurs during the period of highest solvent loss [28]. The devolatilization of the original solvent is almost completed after the second viscosity minimum, thus exposing remaining anhydrides to amidization reaction and displacing the equilibrium of the reaction equation toward the polyamide. This speeds up the reaction, and the majority of the polycondensation by-products are developed during the viscosity build-up.

The strong influence of the masking solvent removal rate on the beginning of the polyimidization reaction indicates that anhydride intermediates are formed from the acid esters during the initial resin heating. With the removal of the masking solvent, the polyamic acid oligomers are formed, followed by the formation of polyimide oligomers.

6.1.2 Bubble Formation During Devolatilization

The ionic viscosity measurements indicate that the devolatilization proceeds in two parts. The first part is completed when the value of the ionic viscosity passes its maximum value. From this point the resin has the consistency of dry powder. The second part of the devolatilization is completed when the polymer glass transition temperature is reached and the polymer softens. The generated bubbles are frozen when the maximum devolatilization occurs and the ionic viscosity curve reaches its inflection point.

Devolatilization is influenced by processing in a vacuum environment. As the pressure decreases, the amidization reaction starts at a lower temperature because of early removal of the volatile masking solvent. The majority of the polycondensation reaction by-products vaporize from the resin during the viscosity build-up, until the viscosity reaches a maximum and the bubbles are frozen. The times when the resin reaches its minimum and maximum viscosity values drop with higher degrees of vacuum. Furthermore, because a higher degree of reaction is achieved when the ionic viscosity is low, a considerably lower amount of volatiles leaves the prepreg resin during the later stage of the process, when the ionic viscosity is high.

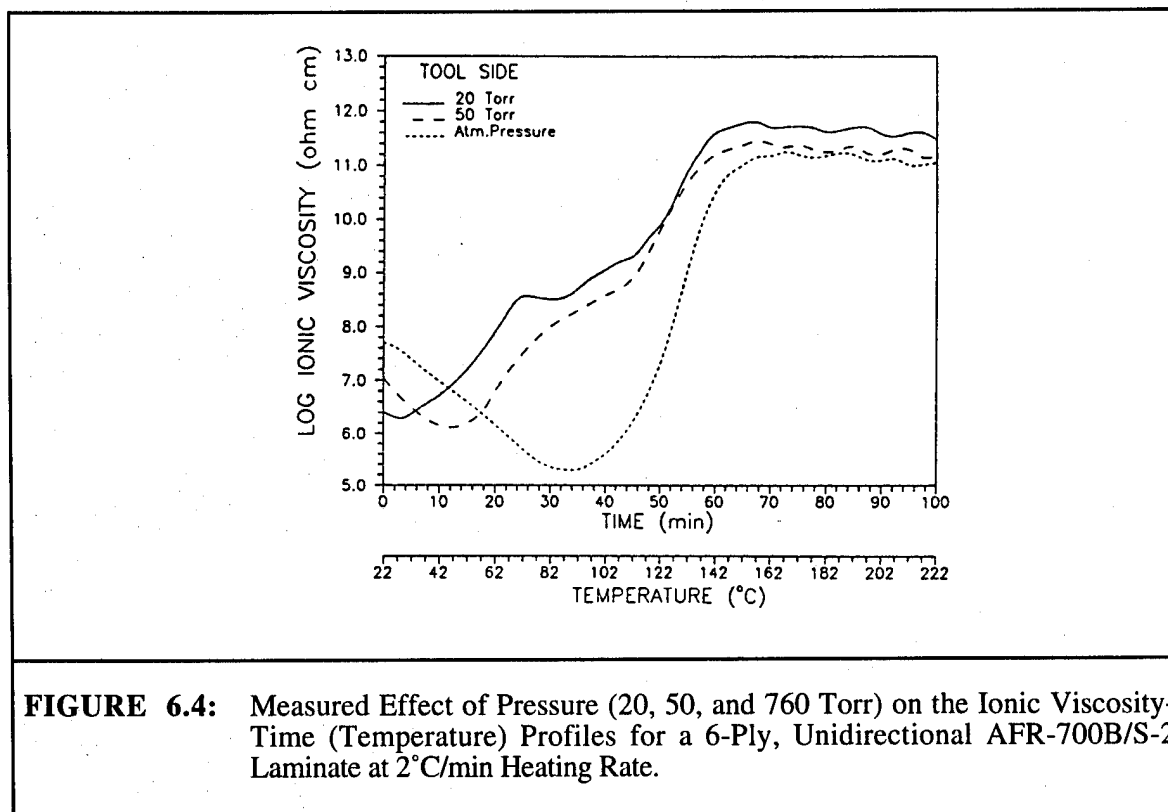
6.2 Effect of Process Parameters on Ionic Viscosity

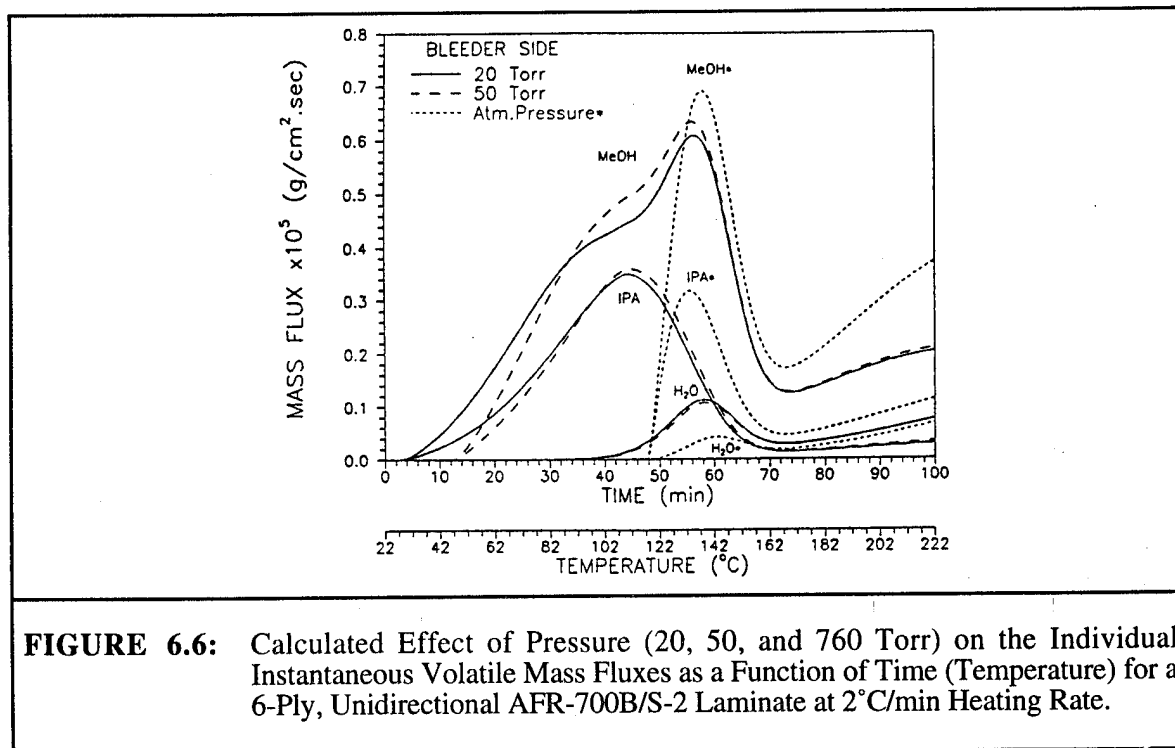
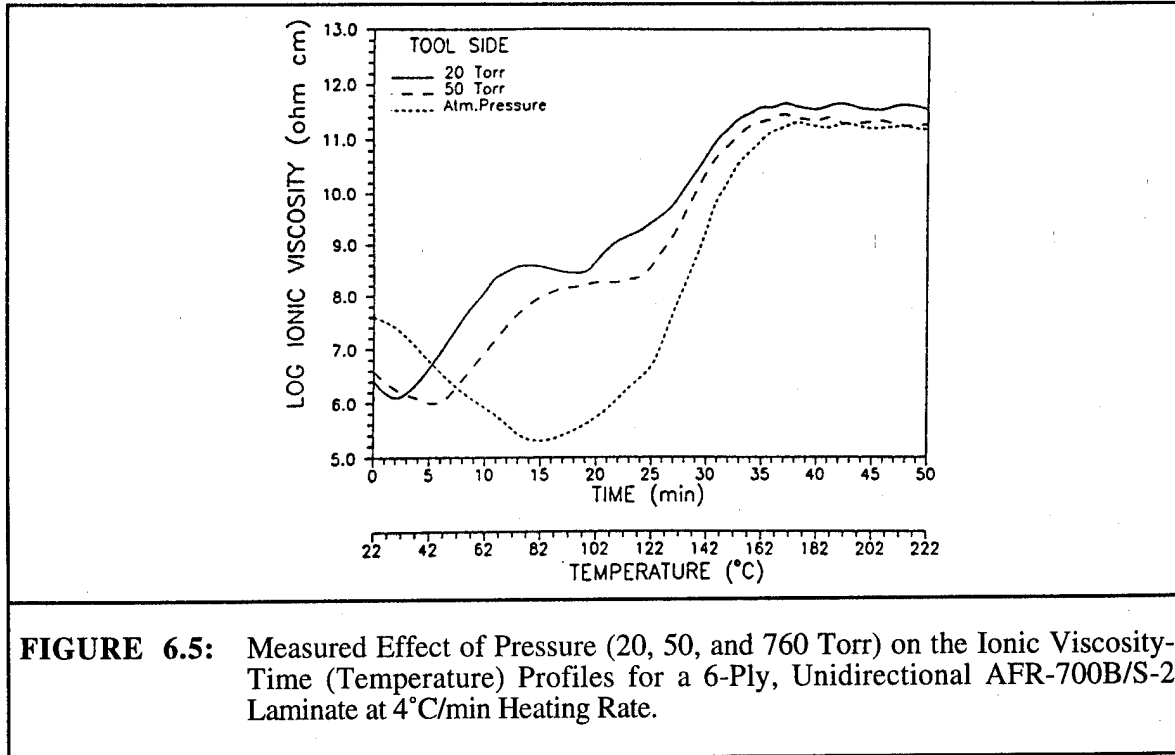
Figures 6.1 to 6.9 provide the basis for explaining the observed changes in the ionic viscosity behavior during the first stage of imidization at different heating rates. These figures provide model simulations of the concentration of volatile species in the liquid phase and individual instantaneous volatile mass fluxes at processing conditions identical to those used for the ionic viscosity measurements (laminate thickness, vacuum level).

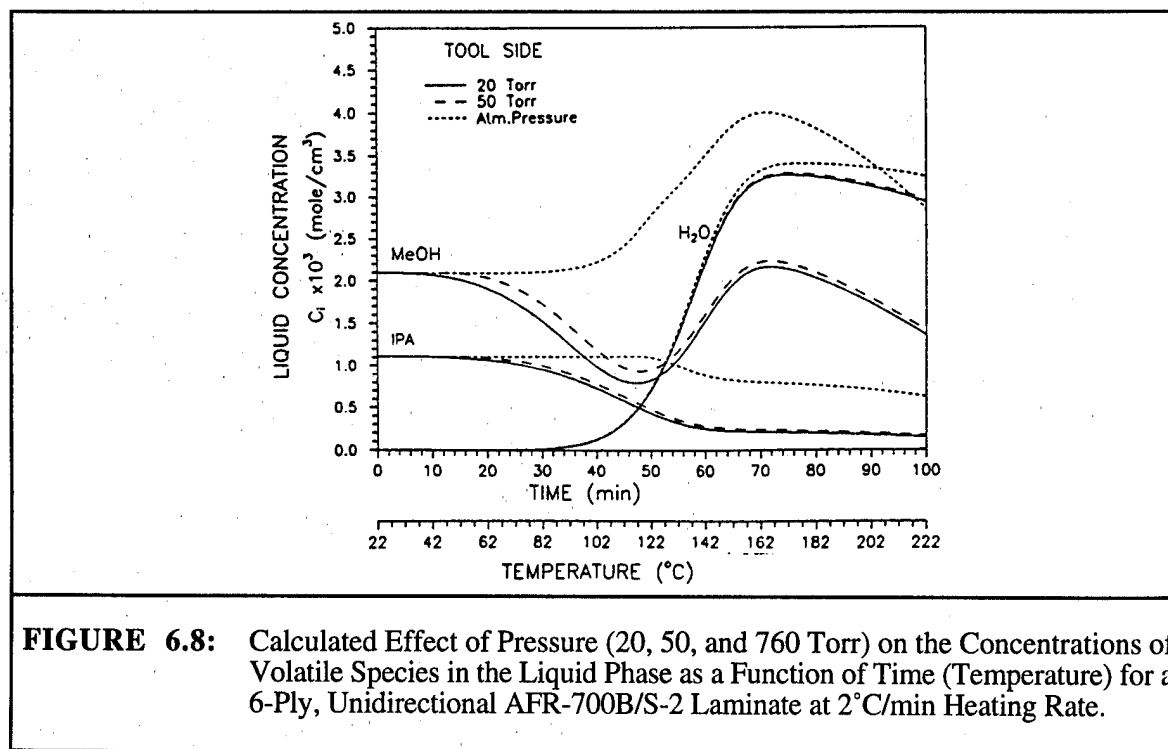
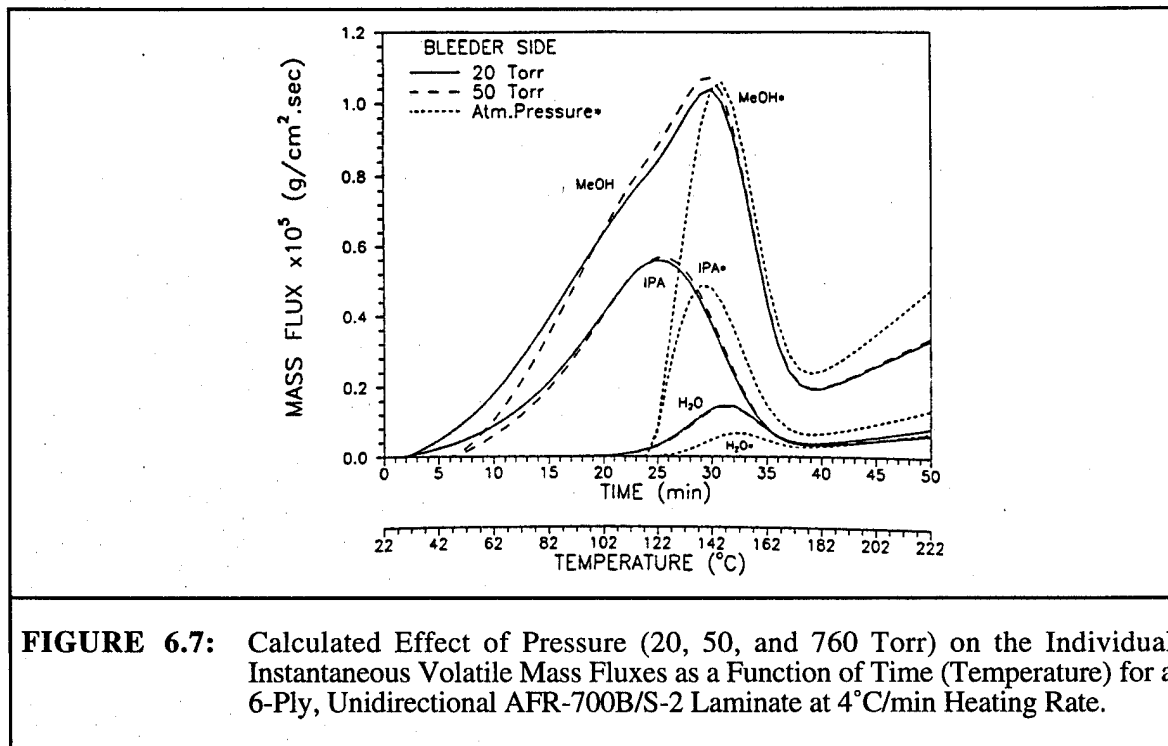
With increasing heating rate, at identical system pressures (20 and 50 Torr) and laminate thickness, the first and second temperature viscosity minima decrease in magnitude, and the low viscosity window at atmospheric pressure expands to higher temperatures (Figures 6.1, 6.4 and 6.5). This occurs because with increasing heating rate more volatiles are developed, and the temperature increase is faster during the time necessary for the original prepreg solvent and by-products of polycondensation reaction to leave the laminate (Figures 6.3, 6.6 and 6.7). The higher heating rates lead to a similar value of ionic viscosity (degree of imidization) although the times at which the minimum and maximum viscosity values are reached drop with increasing heating rate. The retention of the by-products of the polycondensation reaction in the liquid phase increases the molecular chain motion and thus leads to more rapid imidization (Figures 6.2, 6.8 and 6.9).

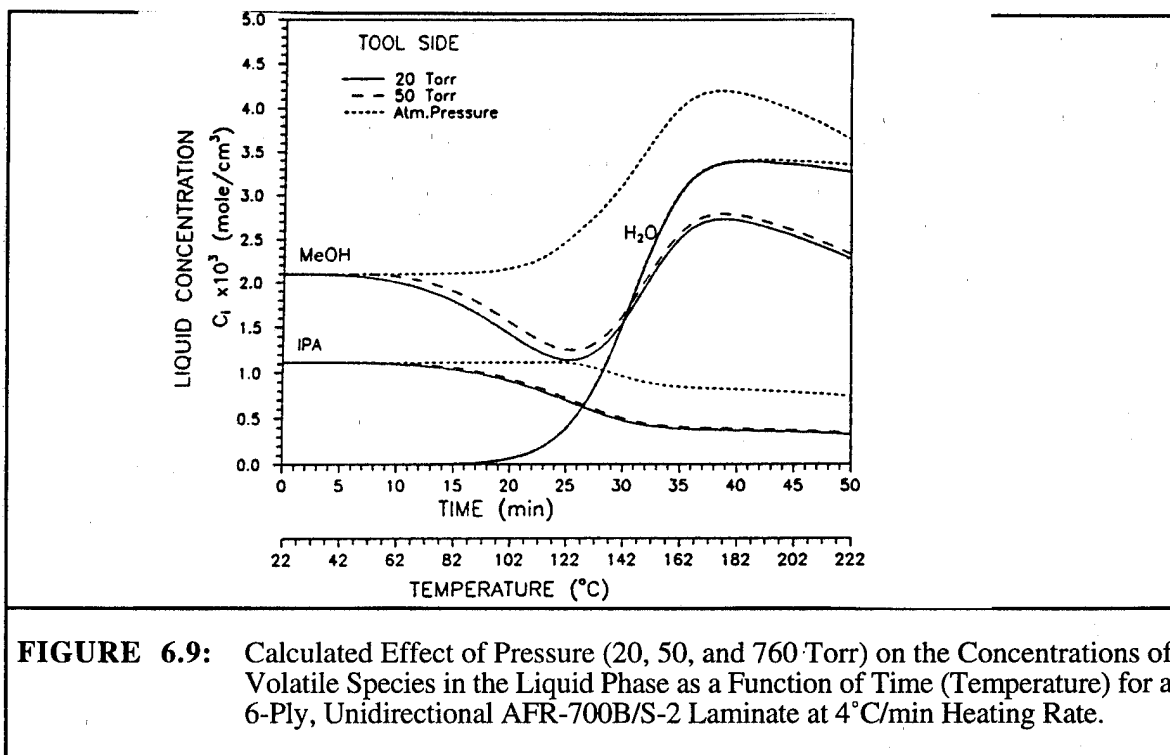
This behavior is consistent with results described for polyimides in the literature. It was found that the level of imidization of polyimide films is directly influenced by the thickness of the polyimide film [41]. A faster loss of solvents and polycondensation products in the thinner polyimide films leads to a lower degree of imidization. Further, it was found that the degree of cure is determined by the rate of imidization which depends on the time it takes for the solvent to diffuse to the surface of the sample and evaporate [42]. At temperatures below 150°C the isothermal imidization is slow, due to low solvent concentration, and only low degrees of imidization are reached. As the isothermal curing temperature increases, the solvent concentration is low which leads to high degree of imidization in a short time. Probably the best consistency with ionic viscosity measurement was reported in the study of the influence of plasticization on the imidization reaction in polyimide films by using dynamic mechanical thermal analysis (DMTA) measurements [43]. The plasticization here implies the formation of water during imidization and the presence of high boiling solvent N-methyl pyrrolidone (NMP) in the resin. The amount of plasticizers generated depends on the rate at which NMP is set free, or water is formed, and the rate at which they diffuse to the surface and evaporate. It was found that at high heating rates the temperature increase is faster than the time necessary for the plasticizers to leave the polyimide film and the plasticization window expands to higher temperatures. The imidization occurs at higher

temperatures where amic acid-imide conversion rates are very high. Thus, high heating rates lead to high degree of imidization although the time the film is in the plasticized region drops with increasing heating rate. All of the above analysis is consistent with the reaction being mass transfer limited.









6.3 Moisture Effects on Ionic Viscosity

In other high performance epoxy/carbon fiber systems moisture originally absorbed by the resin was found to be the main component causing void growth [44]. This growth is possible if the concentration of the dissolved water in the resin (function of relative humidity to which resin was exposed and equilibrated) exceeds the water concentration at the void-resin interface [45]. The influence of this environmentally absorbed water on the dielectric properties during the epoxy resin cure has been studied [46].

Additional work is needed to identify the most important mechanism contributing to conductivity during the entire curing process for polyimide resin containing absorbed moisture. As moisture diffuses into a thermosetting resin, the concentration of the ionic species increases with the concentration of the water, and thus increases conductivity of the resin. The ionic species were found to be the main source of conductivity in polyimide films in the frequency range 1-100 kHz [47]. At low temperatures and in a moist environment (40°C, 32% RH), there are strong ionic impurities-water interactions [48].

It was mentioned previously (section 2.1), that during the cure of high temperature polyimides based on classic PMR-15 chemistry, competing reactions occur, which lead to formation of an anhydride intermediate. The presence of water in the resin solvent solution can complicate the polyimidization reaction even more by forming acid-ester impurities [49-50]. The formation of the acids occurs in the presence of water and the ester impurities formation is a function of solvent content. With solvent devolatilization, the chance for the ester impurities formation decreases and solvent is replaced by water as the "solvent molecule." The acid impurities were reported to increase the polyimidization rate, as opposed to the ester impurities. ^{13}C - NMR analysis of the chemical changes for a 50 wt% methanol solution of the PMR-15 neat resin indicate that within only 24 hours of the resin exposure to 90% relative humidity (RH), significant chemical changes occur. Dielectric analysis of identical samples with and without absorbed water at atmospheric pressure revealed considerable decrease in the value of ionic viscosity during the period of the low viscosity processing window [51]. The influence of freezer storage on the fabrication of PMR-15 polyimide prepreg samples was studied using dynamic dielectric analysis (DDA) [52]. Data indicate that the prepreg resin absorbed a significant amount of moisture during a 7-month freezer storage time, and that absorbed moisture expands the length of time of the low viscosity region during laminate curing.

In this study the AFR-700B/S-2 glass fiber polyimide prepreg plies (5 x 5 cm lateral dimension), containing 11.4 wt% of solvent solution (5.7 wt% methanol and 5.7 wt% isopropanol) were measured after 6 months under freezer storage conditions. Figure 6.10 shows the effect of pressure (20 and 760 Torr) and absorbed water on the ionic viscosity versus time profiles for a heating rate of $1^\circ\text{C}/\text{min}$. and composite thickness of 2 mm (5 plies). Figures 6.11 and 6.12 display model simulations for volatile species concentrations in the liquid phase and for the individual instantaneous volatile mass fluxes at processing conditions identical to the ionic viscosity measurements (laminate thickness, system pressure). It was assumed that the amount of absorbed water was 0.5 wt%.

Ionic viscosity measurements at 20 and 760 Torr with no water present are identical for those described previously in section 6.1. During the initial heating of the sample with absorbed water at atmospheric pressure, the steep decrease in the ionic viscosity (Figure 6.10) reflects the decrease in the resin viscosity due to dissolving of the monomer into the original prepreg solvent (methanol and isopropanol) and environmentally absorbed water. The absorbed water lowered the resin viscosity, compared to that for the sample without the absorbed water. With rising temperature, the amidization and attendant imidization reaction proceeds, which is associated with the increasing

value of ionic viscosity. During this time a relatively large volume of original solvent, absorbed moisture and product of polycondensation reaction (methanol and water) vaporize (Figure 6.12). The gas bubbles rupture on the surface of the prepreg plies. The ionic viscosity rises until 140°C where it reaches a maximum value and where the gas bubbles in the resin are likely to be immobilized. A large amount of residual solvent, absorbed water, and by-products of polycondensation reaction still vaporizes at this final stage of the imidization reaction because the resin still has the consistency of dry powder, making volatile removal still possible.

Experiments performed under vacuum (20 Torr) on a sample with water absorbed during the 6 months freezer storage revealed two minima in the measured ionic viscosity as was observed in samples without the absorbed water (Figure 6.10). With increasing temperature, the steep increase in the ionic viscosity curve is due to the increasing resin viscosity. The removal of solvent volatiles, particularly methanol, increases the rate of the amidization reaction because the removal of methanol displaces the equilibrium of Figure 2.1 toward the polyamide. The second minimum of the ionic viscosity (Figure 6.10) reflects the disappearance of the original prepreg solvents and absorbed moisture together with the continued rise in temperature. Devolatilization of polycondensation by-products then begins (Figure 6.12), along with polyamidization, and the viscosity once again rises. During this time, gas bubbles are generated and eventually rupture on the laminate surface. From this point, the rising value of ionic viscosity indicates increasing molecular weight of the polymer as polyimidization proceeds. Ionic viscosity rises until 140°C where generated bubbles are frozen. Beyond this temperature, the value of ionic viscosity decreases slightly and a relatively small amount of volatile polycondensation reaction by-products still vaporizes.

With increasing heating rate at identical system pressures (20 Torr) and laminate thickness, the first and second ionic viscosity temperature minimums of samples with absorbed water again decrease in magnitude (Figures 6.10, 6.13, and 6.14), because with increasing heating rate the temperature increase is faster than the time necessary for the original prepreg solvent, absorbed water, and polycondensation by-products to leave the laminate (Figures 6.12, 6.15, and 6.16). The maximum magnitude of ionic viscosity in samples with absorbed water at the system pressure is similar to that without the absorbed water. For the 20 Torr results, increasing the heating rate causes a difference between the water-containing and dry samples, when one looks at the time (temperature) at which the viscosity maximum is achieved. This difference is insignificant when one goes from 1°C to 2°C/min, but it appears to be real in going from 2°C to 4°C/min.

It appears that absorbed water accelerates the progress of the polyimidization reaction at low pressures. The removal of the original prepreg masking solvent under vacuum starts at a lower temperature. This exposes anhydrides to amidization reaction and to formation of acid impurities due to absorbed water at lower resin viscosity. The amidization reaction rate is increased because of the formed acid impurities. The final stage of the polyimidization reaction, when the resin reaches a maximum value of ionic viscosity, is not influenced, because the absorbed water is already removed.

At atmospheric pressure, the absorbed water in the laminate sample adds considerably to the decrease in the minimum of the ionic viscosity during the low viscosity processing window and slightly expands the end of the window to higher temperatures. Compared to the 20 Torr data, the masking solvent is not removed from the resin at atmospheric pressure until higher temperatures are reached. The experiments at atmospheric pressure with water-containing and dry samples lead to similar maximum values of ionic viscosity, because the amidization and subsequent imidization reactions proceed very quickly at higher temperatures.

As mentioned above, the absorbed water retards the devolatilization process more at atmospheric pressure than at 20 Torr. The removal of the original masking solvent and by-products of the polycondensation reaction proceeds only at high temperatures concurrently with the removal of the absorbed water. The monomer active groups are not open to the amidization reaction during the duration of the entire low viscosity processing window, as they were in the 20 Torr situation. The absorbed water is not entirely removed from the laminate during the viscosity build-up; thus the absorbed water, the original prepreg solvent, and the polycondensation by-products are still vaporizing as the resin viscosity reaches its maximum. This means that more volatiles must be removed at later stages of the process cycle, when the viscosity is high, leading to an increased risk of void formation.

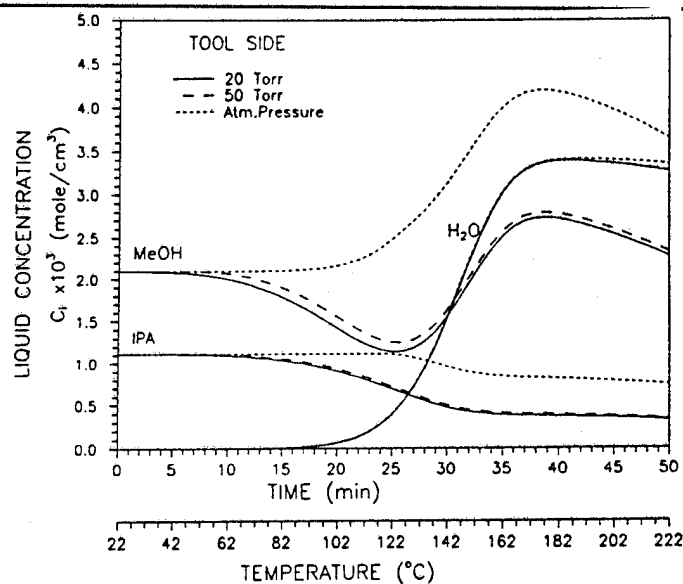


FIGURE 6.10: Measured Effect of Pressure (20 and 760 Torr) and Absorbed Water on the Ionic Viscosity-Time (Temperature) Profiles for a 6-Ply, Unidirectional AFR-700B/S-2 Laminate at 1°C/min Heating Rate.

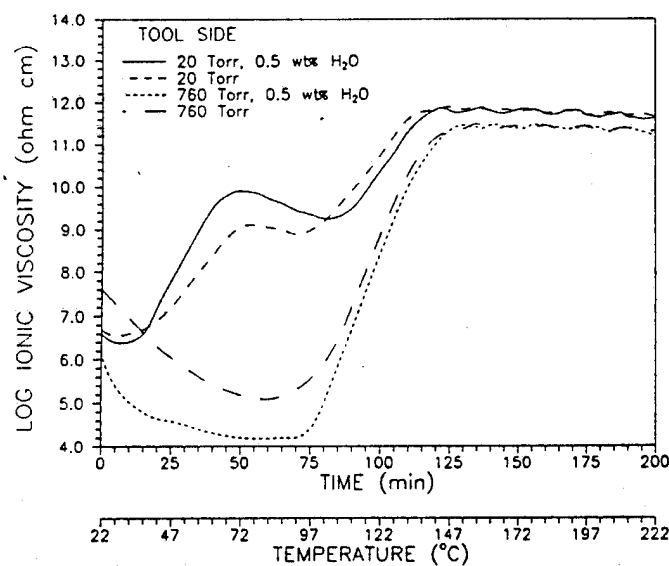


FIGURE 6.11: Calculated Effect of 0.5 wt% of Absorbed Water on the Concentration of Volatile Species in the Liquid Phase as a Function of Time (Temperature) for a 6-Ply, Unidirectional AFR-700B/S-2 Laminate at 1°C/min Heating Rate and Pressures of 20 and 760 Torr.

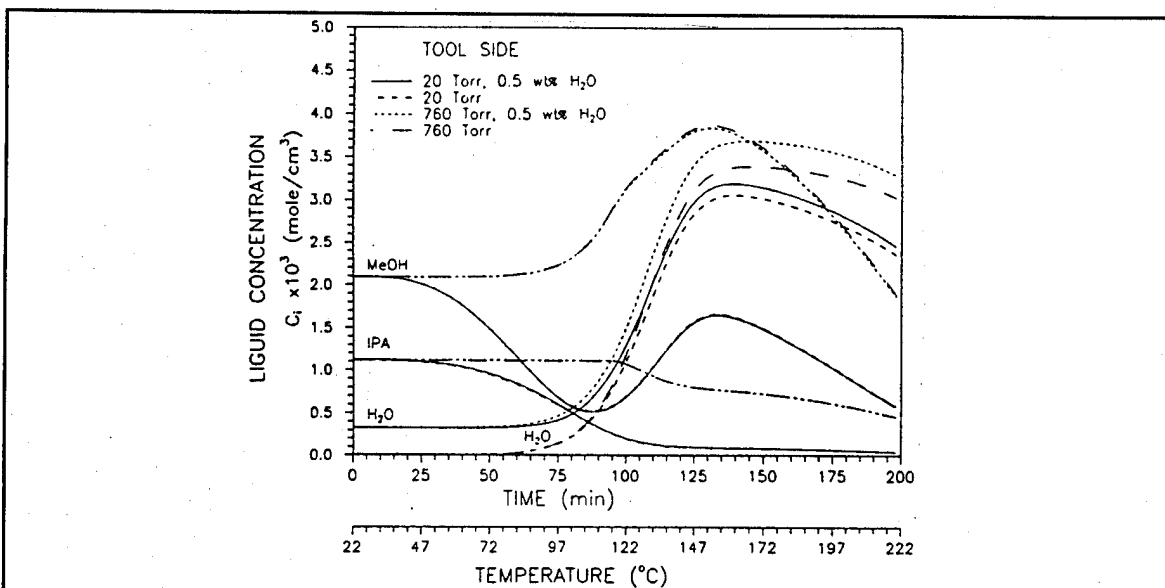


FIGURE 6.12: Calculated Effect of 0.5 wt% of Absorbed Water on the Individual Volatile Mass Fluxes as a Function of Time (Temperature) for a 6-Ply, Unidirectional AFR-700B/S-2 Laminate at 1°C/min Heating Rate and Pressures of 20 and 760 Torr.

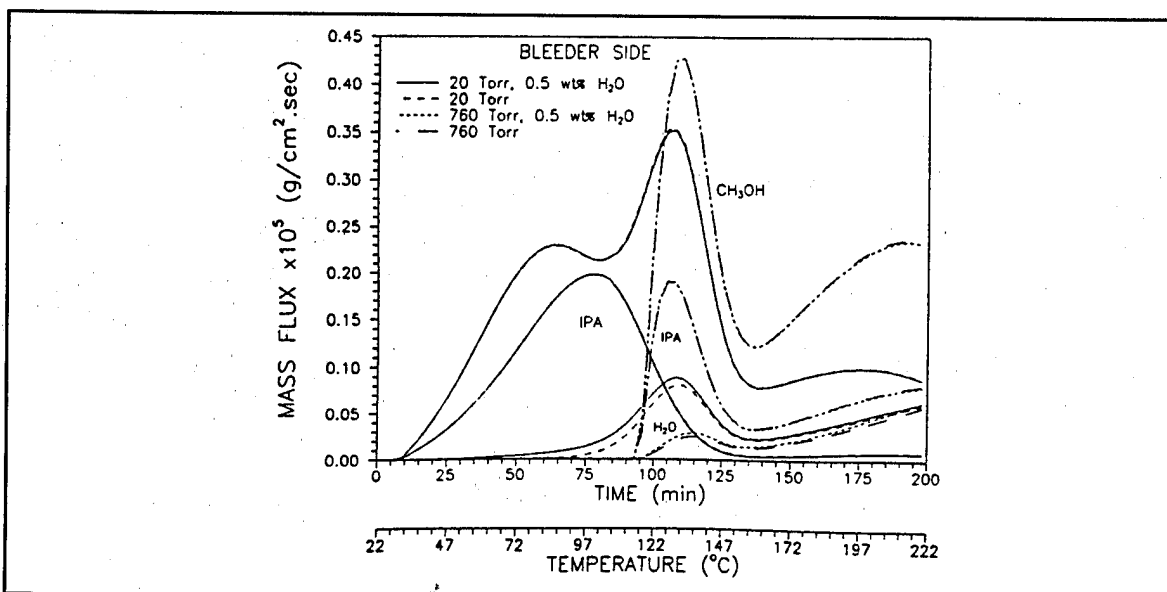


FIGURE 6.13: Measured Effect of Pressure (20 and 760 Torr) and Absorbed Water on the Ionic Viscosity-Time (Temperature) Profiles for a 6-Ply, Unidirectional AFR-700B/S-2 Laminate at 2°C/min Heating Rate.

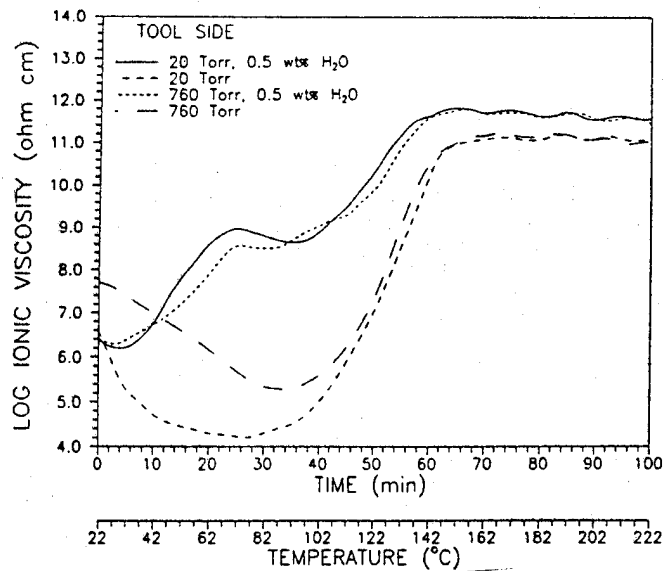


FIGURE 6.14: Measured Effect of Pressure (20 and 760 Torr) and Absorbed Water on the Ionic Viscosity-Time (Temperature) Profiles for a 6-Ply, Unidirectional AFR-700B/S-2 Laminate at 4°C/min Heating Rate.

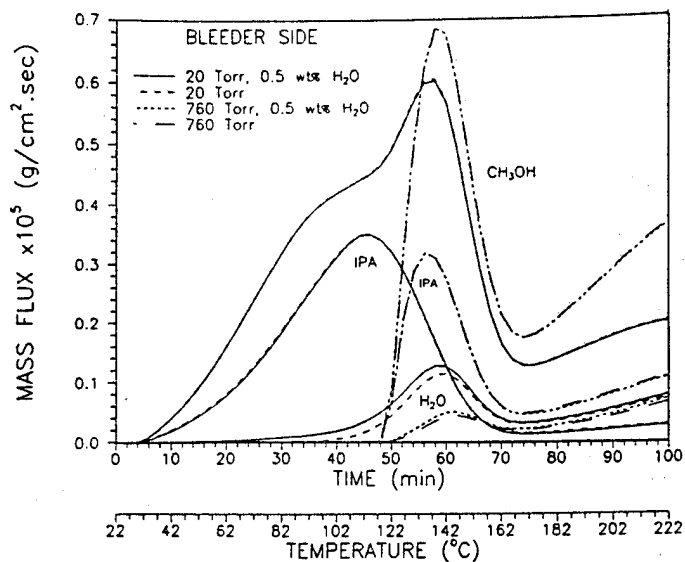


FIGURE 6.15: Calculated Effect of 0.5 wt% of Absorbed Water on the Individual Instantaneous Volatile Mass Fluxes as a Function of Time (Temperature) for a 6-Ply, Unidirectional AFR-700B/S-2 Laminate at 2°C/min Heating Rate and Pressures of 20 and 760 Torr.

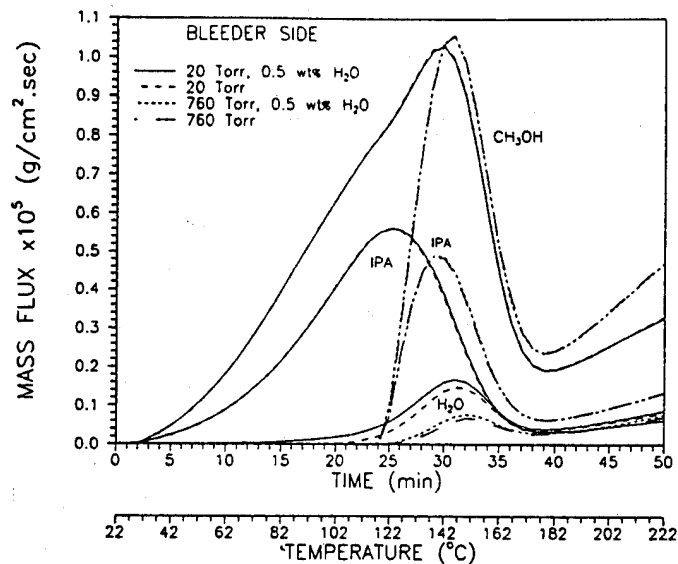


FIGURE 6.16: Calculated Effect of 0.5 wt% of Absorbed Water on the Individual Instantaneous Volatile Mass Fluxes as a Function of Time (Temperature) for a 6-Ply, Unidirectional AFR-700B/S-2 Laminate at 4°C/min Heating Rate and Pressures of 20 and 760 Torr.

7.0 SIMULATION OF PROPOSED INDUSTRIAL CYCLES

The devolatilization model was used to simulate the volatile evolution process for the current standard Air Force Extended cure cycle [53] and the Qualitative Process Automation (QPA) intelligent sensor feedback controlled cure cycle as employed by S. Ferer at Hughes [53]. QPA controls the autoclave temperature and pressure in response to sensor data input rather than responding to a fixed cure cycle. The DekDyne Frequency Dependent Electromagnetic Sensing (FDEMS) dielectric sensor was used at Hughes for measurements of the AFR-700B/T650-42 carbon prepreg resin. The FDEMS dielectric sensor data feeds back information about the flow of AFR-700B prepreg resin to the QPA expert system to control the processing of the laminate. The neat resin was manufactured by Dexter Corp. The prepreg was prepared by YLA Inc. and contained 10 wt% of methanol as prepreg solvent and 54.3 wt% of T650-42 carbon fiber (YLA hot melt batch FB1K204) [15]. The sensor was mounted on top of the measured sample and protected from shorting electrically against conductive carbon fibers by wrapping it with 2 plies of 120 style fiberglass. Two Marlin high-temperature type *J* thermocouples were used during the cure measurements, one above and one below the sample at the edges of the sample [15].

7.1 Comparison of Process Simulations and Real-Time Dielectric Sensor Data

Figure 7.1 shows the loss factor versus time profile for a laminate cured by the current standard Air Force extended cure cycle under full vacuum, with a laminate thickness of 0.318 cm (8 plies, 28 x 54 cm lateral dimension). The cured panel had a high void content from 5.3% to 11.2%, and a glass transition temperature (T_g) of 400°C [53].

Figure 7.2 represents the loss factor versus time profile for a laminate cured by a developed QPA knowledge base and sensor feedback controlled cure cycle, under full vacuum, with a laminate thickness of 0.584 cm (16 plies, 28 x 18 cm lateral dimension). The cured panel had a void content from 3.9% to 4.4%, and a T_g of 412°C [53]. The first cured panel had an average void content much higher than the 4% allowed by Advanced Material Processing Control (AMPC) success criteria [54]. The dielectric sensor response at the beginning of both measurements is not accurate due to the need for the resin to impregnate and wet the glass cloth protecting the dielectric sensor from the conductive T650-42 carbon fibers [15].

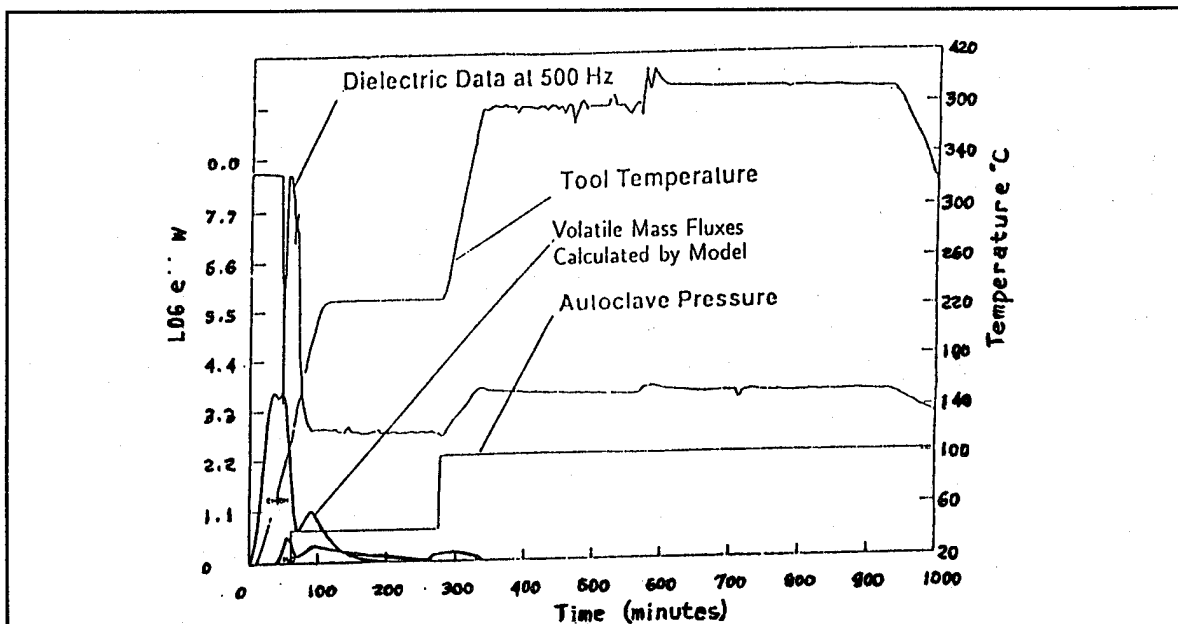


FIGURE 7.1: Measured Dielectric, Temperature and Pressure Sensor Responses Together with Model Calculations for Individual Volatile Mass Fluxes for an 8-Ply, Unidirectional AFR-700B/T650-42 Carbon Laminate Cured by Air Force Extended Cure Cycle [53].

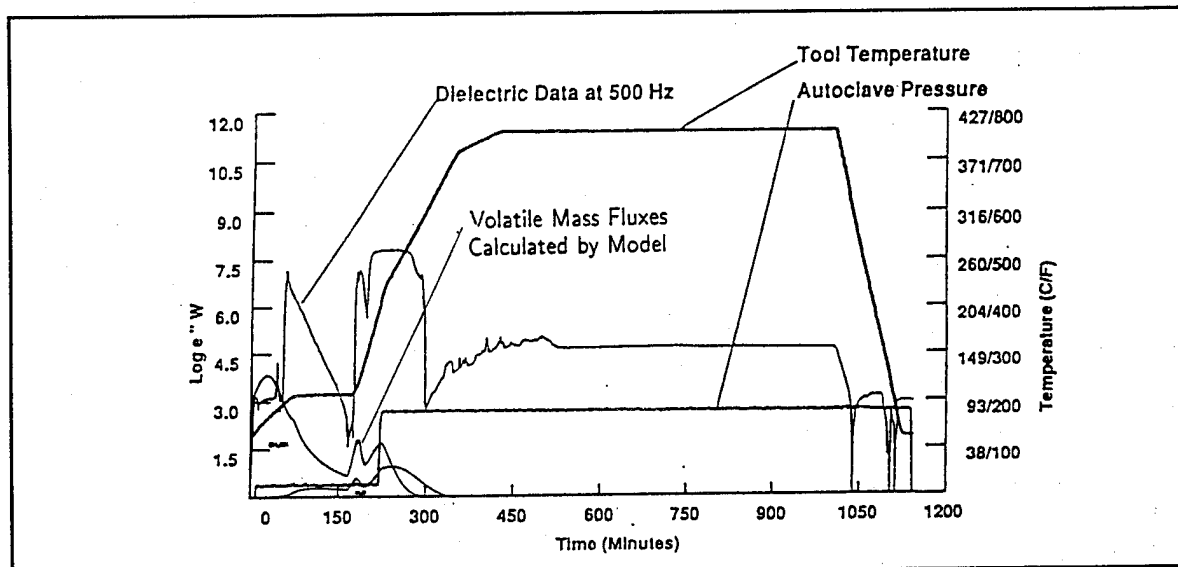


FIGURE 7.2: Measured Dielectric, Temperature and Pressure Sensor Responses Together with Model Calculations for Individual Volatile Mass Fluxes for a 16-ply, Unidirectional AFR/T650-42 Carbon Laminate Cured by QPA Controlled Cure Cycle [52].

Figures 7.1 and 7.2 also contain devolatilization model calculations for the individual instantaneous volatile mass fluxes computed for identical processing conditions at which the dielectric loss factor measurements were made (20 Torr pressure, heating and holding time, laminate thickness). The tool temperature data measured for both cure cycles (Figures 7.1 and 7.2) were used for the devolatilization model simulations. The model simulations were performed up to the softening period during the polyimide processing. The crosslinking reaction initiated via the reverse Diels-Alder reaction is believed to start at beginning of this softening region (300°C) [55].

During the initial heating of the laminate cured by the Air Force extended cure cycle under full vacuum (Figure 7.1), the steep decrease in the loss factor reflects the decrease in the resin viscosity due to redissolving of the monomer into the original prepreg solvent (methanol). The maximum value of the loss factor indicates the minimum resin viscosity and time when the amidization reaction starts. With increasing temperature the maximum devolatilization of the original prepreg solvent occurs together with starting devolatilization of the by-products of the polycondensation reaction (methanol and water). The steep decrease in the loss factor is due to the imidization reaction which greatly increases the molecular weight of the oligomer. During this time the maximum devolatilization of the polycondensation by-products proceeds. The decrease in the loss factor value stops at 190°C where generated bubbles are frozen. After this point the resin dries to a powder consistency and only a small amount of polycondensation by-products vaporizes. With heating to 240°C the loss factor starts to increase again as the prepreg resin passes its glass transition point and softens. During this time, the remaining small amount of polycondensation by-product (water) vaporizes. The devolatilization process is essentially completed during the softening region. It is notable that the model simulation exhibits three peaks in the water volatile flux. The third high temperature peak is a result of the temperature profile used in this processing cycle. Unlike the earlier experimental results of this study, the Air Force cycle has a temperature hold, followed by a fast temperature ramp. What the model is telling us is that this particular cycle does not allow complete water devolatilization until the resin softening region is attained. This presents the risk of water voids in the final part, particularly for thick laminates.

The devolatilization process for the laminate cured by the QPA intelligent sensor feedback controlled cure cycle is separated into two parts (Figure 7.2). The first part (devolatilization of original prepreg solvent and starting devolatilization of the polycondensation by-products) is completed when the value of the loss factor reaches its first minimum. The second part of the devolatilization (removal of by-products of the polycondensation reaction and remaining free solvent) is completed during the softening region.

The different curing cycles employed (heating rate during amidization and imidization, and temperature at which and time for which the temperature was held constant) influence the devolatilization of the original prepreg solvent and polycondensation by-products. The QPA knowledge base controls the processing of a material using the physical and chemical condition of the laminate at a specified event in the cure, rather than by an elapsed time. Special episodes are also written to control the autoclave if abnormal conditions arise, such as too great a thermal gradient between the tool and the top of the laminate [53].

In both previously discussed examples, devolatilization model calculations of the individual mass fluxes indicate that a small amount of polycondensation by-product (water) is still evolved in the softening region. The devolatilization process is completed before the prepreg resin reaches the end of the softening region. It is speculated that if the prepreg resin viscosity at the end of the softening region is increased by an already proceeding reverse Diels-Alder crosslinking reaction, a remaining small amount of condensation by-product (water) can be trapped inside the laminate and voids and porosity will be created at this stage of the cure process. The model simulations indicate that slightly more water volatiles are developed at this stage of the cure cycle in the laminate processed by the Air Force extended cure cycle. The application of the QPA feedback control during the autoclave processing clearly decreases the amount of voids and porosity in the final laminate.

8.0 CONTROL RULES AND STRATEGIES

The original task statement called for a rule-based strategy for control to be developed using the process simulator for the AFR-700B system. As the prior section shows, some specific rules can be enunciated and utilized in the QPA system. In the spirit of advancing the control strategies beyond the current QPA status, we have attempted to build artificial intelligence concepts and methods into a more advanced strategy. Because the AFR-700B data base and simulator were not yet ready, we employed a version of the carbon/epoxy cure simulator to illustrate the concept. We present that material in this report for completeness and with the understanding that some of what is reported here was funded by the National Science Foundation under NSF grant DDM-9123861 from the Division of Design and Manufacturing Systems.

8.1 Model-Based Control of Voids and Laminate Thickness During Autoclave Curing of Carbon/Epoxy Composite Laminates

Automation of the composite manufacturing process has been stimulated by recent developments in computer technology (artificial intelligence, neural networks, etc.), process control theory (model predictive control, control using secondary measurements) and new sensor technology (new sensors for monitoring the extent of cure, viscosity of the resin, etc.). Combined synergism of these technologies provides an opportunity to develop a highly automated environment for composite manufacturing, thus making it more affordable for large volume commercial applications.

In this section, we present a methodology for improved control of thickness and void size during the autoclave curing of carbon/epoxy or carbon/polyimide composite laminates. A strategy that utilizes a *data driven* processing model and intermediate secondary measurements (taken during the cure cycle) is suggested. An Artificial Neural Network (ANN) is used as a modeling tool. This model is employed in a model predictive control scheme to provide on-line feedback correction to the cure cycle used. Hence, the strategy is referred to as "On-line Neurocontrol."

8.1.1 Background

To select such an operational plan for an autoclave cure cycle, Loos and Springer [56] suggested the following criteria:

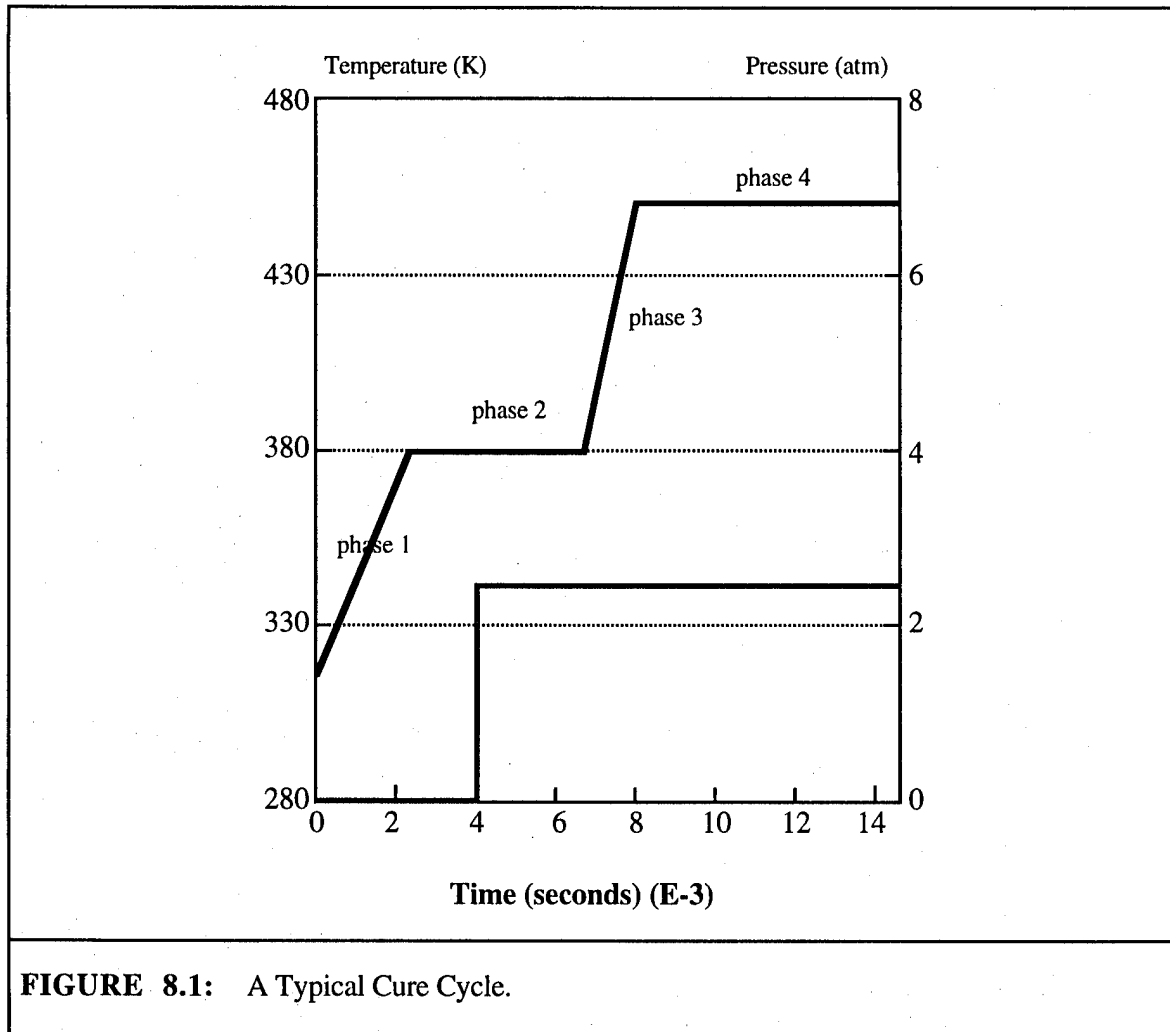
- a. The temperature at any position inside the laminate should not exceed a prescribed limit during the curing process.
- b. The magnitude of the cure pressure should be sufficiently high so that all of the excess resin is squeezed out from every ply of the composite before the resin gels at any point inside the composite.
- c. The pressure should be applied before the viscosity of the resin in the prepreg ply adjacent to the bleeder becomes low enough to flow.
- d. The resin should be cured uniformly and the degree of cure should be above a specified limit throughout the composite at the end of cure.
- e. The cured composite must have a low void content.
- f. The composite should be cured in the shortest time possible subject to the above criteria being fulfilled.

Another critical finding by Kardos [57] is:

- g. A resin pressure higher than the saturated pressure inside the void should be applied before the gel point is reached in order to collapse any vapor bubbles.

Industrial practice is to generate a cure cycle through trial and error combined with past experience. [58,59]. Figure 8.1 shows one such standard cure cycle employed for epoxy/carbon fiber composites. The key decision variables here (called *manipulated inputs* from a control system point of view) include:

- the time to apply the pressure
- the pressure applied
- the first hold temperature
- the second hold temperature



There are numerous other variables (e.g., the ramp rate of temperature) which can also influence the product quality.

Variations in the properties of the raw materials and the geometry of the part being manufactured will require modifications to the standard cure cycle. Hence a flexible operation plan is desirable. Servais et al. [60] and Lee [61] discuss different approaches that can be employed including trial and error, mathematical simulation and rule-based expert systems. Roberts [62] also described the components of a hypothetical automated cure cycle system for composite manufacturing.

The possible control strategies for autoclave curing can be classified as follows:

Standard cure cycle - This type of control is based on a predetermined plan of operation and is based on previous successful runs. The objective of control is to force the cure cycle to follow a prescribed path.

Knowledge-based expert system control - This type of control, also referred to as Qualitative Process Automation (QPA) is based on modifying the cure cycle based on past experience expressed in the form of control rules. Such an approach was employed by Lee [61] and LeClair et al. [63]. Wu and Joseph [64] later extended this architecture to incorporate an on-line process model. The bottleneck associated with this "rule-based" approach is in the acquisition of control knowledge. Another drawback is that there is no adaptation to changing processing requirements which may invalidate some of the knowledge contained in the control rules.

8.1.2 Data Driven Models for Process Control

For process control purposes, a model must have the following properties:

- It must relate the product quality to the manipulated input variables.
- It must take into account the effect of measured input disturbances.
- It must utilize the intermediate secondary measurements available while the cure cycle is in progress to correct for unmeasured disturbances and modeling errors.

Quantitative models for predicting quality can be classified into two categories:

- (i) Fundamental processing models based on physical and chemical events taking place in the autoclave.
- (ii) Regression-type models which are comprised of a fit of the observed product quality to the input raw material properties and the processing conditions used.

When available, fundamental processing models are preferred for control. Unfortunately for many complex processing operations, such as the autoclave curing process, these models, because of long computing times, are not yet in a form suitable for on-line implementation.

For batch processes, like autoclaving, linear input/output models cannot be used because of the time-dependent nature of the process and the extreme variations in states that occur during the processing. Hence one must employ a nonlinear process model. Such a nonlinear model will have

to be obtained by fitting the data collected from many batch runs through some type of nonlinear regression technique.

Regression models rely upon data collected from test runs and routine data collected while production is in progress. Because regression models represent a fit, they can predict the product quality accurately only over a small operating window. Deviations outside the window require new data to be collected for updating the model. In the past, linear and quadratic regression have been used to fit the data. This further limits the range of applicability of the model because additional constraints are imposed on the nature of the non-linearity present in the system. Recently a new paradigm called *Artificial Neural Network* (ANN) has emerged for modeling of arbitrary non-linear input/output mapping. A brief description of ANN is given here. Details are given in many books (see for example, Rummelhart et al. [65]).

ANNs were inspired by the research done on biological nervous systems. Numerous structures have been proposed in the literature for building ANN models. Among these the multilayer perceptron [65] has emerged as a model suitable for non-linear regression modeling. This model, sometimes referred to as a feed forward network, is made up of individual perceptrons as illustrated in Figure 8.2.

$$y = f\left(\sum_{i=0}^N w_i x_i - \theta\right) \quad (8.1)$$

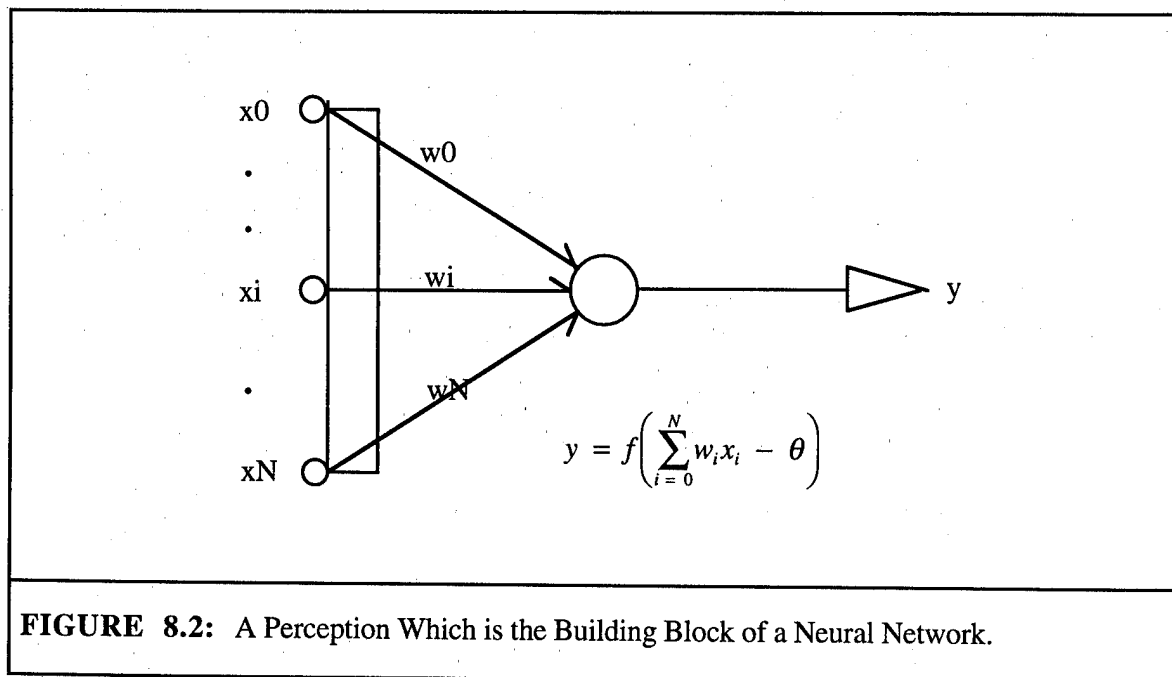


FIGURE 8.2: A Perceptron Which is the Building Block of a Neural Network.

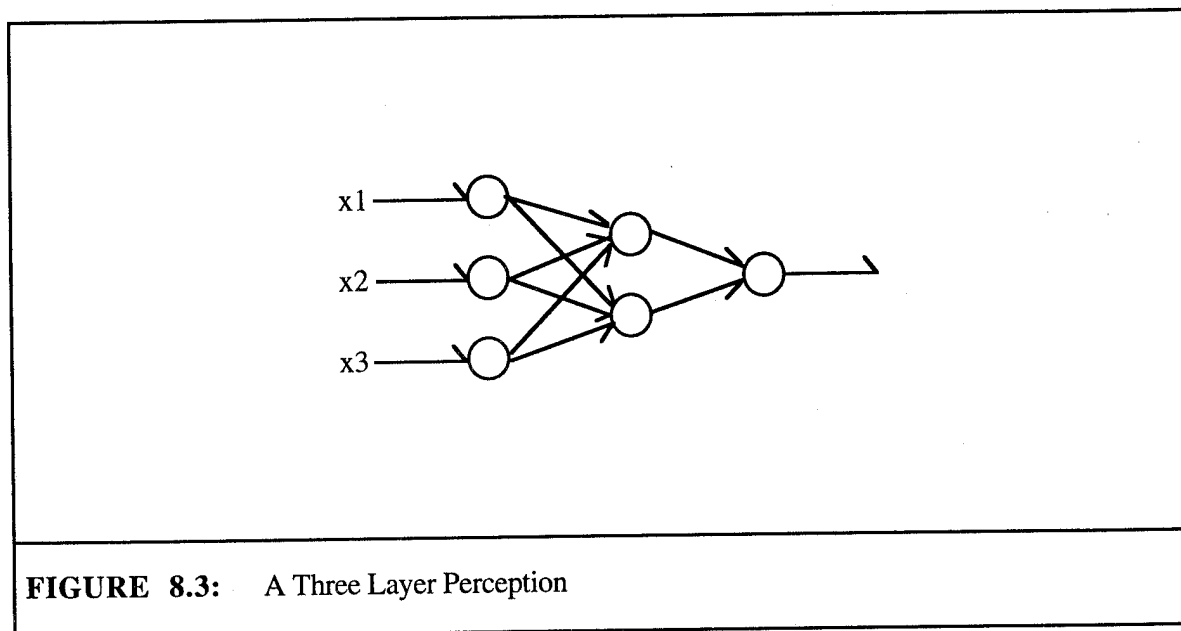
Each perceptron has many inputs and the output is a weighted sum passing through a non-linear function, f ; usually a sigmoid function is employed:

$$f(a) = \frac{1}{1 + e^{-(a \cdot \Theta)}} \quad (8.2)$$

where Θ is a threshold value associated with each node. An ANN is made up of multiple perceptrons arranged in the form of input nodes, one or two hidden layer of nodes and output nodes. Figure 8.3 shows a three-layer perceptron.

$$y = g(x_1, x_2, x_3) \quad (8.3)$$

The weights associated with each link are adjustable. These weights are typically adjusted so that the network can fit a training set of data in the form of quadruplets (x_1, x_2, x_3, y) .



Neural networks with a sufficient number of nodes and hidden layers have been shown to be capable of learning to map arbitrary functions. There are two phases to the use of an ANN:

Training phase: Data sets $(x_1, x_2, \dots, x_n, y)$ are repeatedly presented to the network. The weights are adjusted so that error between the value of y predicted by the ANN and the value in the training set is minimized in a least-square sense.

Production phase: In this phase, given new input data sets (x_1, \dots, x_n) the network is used to predict the value of y .

Batch processes, such as the autoclave curing of composites, are inherently dynamic systems and are nonlinear. From the point of view of quality control, the issue is to be able to have a model that will predict the outcome of the batch (i.e., product quality) in terms of the input and processing variables. The variables associated with the process can be categorized as follows:

- (1) Input Disturbances, $d(t)$: Uncontrollable variations in the properties of the feed materials and variations in environmental variables such as resin water content, resin/curing agent ratio, prepreg storage humidity, etc.
- (2) Manipulated Inputs, $m(t)$: These are variables such as operating temperature, pressure, changes in set points of regulatory controllers with time, time sequence of events and other corrective actions that can be taken while the cure cycle is in progress.
- (3) Intermediate measurements, $y(t)$: These are dependent variables, and are generated by sensors on the process. They are indirect indicators of final product quality. This means that they should be useful in predicting the outcome of the cure cycle.
- (4) Output variables, q : These are measures of quality of the product laminate. Some of these variables are functions of time, e.g., the changes in the setpoint of a temperature controller as a cure cycle is in progress. Recipes for cure cycles typically specify the set points of these low level controllers as a function of time.

We conducted a study to see the effectiveness of ANN in predicting quality outcome of the autoclave process as a function of the processing conditions. Our objective was to see if there was a significant advantage in using ANN instead of the traditional regression methods. Data for this study were generated using an autoclave simulation model developed by Wu [66]. The input disturbance variables of interest are:

- (i) Initial weight fraction of resin in the prepreg, wt.
- (ii) Impurity in the feed, im.
- (iii) Initial size of voids present in the pepreg, initb.
- (iv) Initial temperature of the pepreg, initt.

The manipulated input variables of interest are (see Fig 8.1):

- (i) The autoclave pressure, p_r .
- (ii) The first holding temperature, t_1 .
- (iii) The second holding temperature, t_2 .

The objective is to build a model capable of predicting the following output quality variables:

- (i) The product laminate thickness, th .
- (ii) The maximum void size in the product, V_s .

The study was conducted as follows: A "Training Set" of data consisting of 198 records as illustrated in Table 8.1 was generated using the simulator. A second "Test Set" of 99 records was also generated to test the validity of the models generated. First, a quadratic regression was used to fit the two output quality variables to the independent variables, x_i shown in Table 8.1. Next the accuracy of this model was computed by comparing its predictions against the observed values in the Test Set. The same exercise was repeated using an ANN model. The results are compared in Table 8.2.

TABLE 8.1: Typical Data Record Used in Regression			
Variable and Description	Batch #1	Batch #2	Batch #198
Product Quality: Dependent Variables, q			
1. Thickness of Laminate, cm: th	1.689	1.695	1.820
2. Max Void size, cm: V_s	0.005	0.012	0.080
Independent Variables, x_i			
1. weight fraction resin: wt	0.380	0.418	0.436
2. impurity in feed: im	0.072	0.060	0.081
3. initial void size, cm: $initb$	0.0653	0.0520	0.0997
4. initial temp of prepreg, K: $initt$	296.8	290.2	299.0
5. autoclave pressure, atm: pr	3.8	3.2	2.5
6. first holding temperature, K: $t1$	382.3	378.1	384.2
7. Second holding temperature, K: $t2$	444.2	437.2	448 0

TABLE 8.2: Results of the Regression Study			
Independent Variable	Measure of Fit	Quadratic Regression	ANN Model
Product Thickness	R^2	0.9186	0.9999
	\bar{E}	0.0168	0.0105
Void Size	R^2	0.4962	0.6567
	\bar{E}	0.0119	0.0077

The results are presented in terms of the accuracy of output prediction in the test data set. Two criteria were used for ascertaining the accuracy. The first is the R^2 criteria defined as:

$$R^2 = 1 - \frac{E(q_i - \hat{q})^2}{E(q_i - \bar{q})^2} \quad (8.4)$$

where q_i is the actual output (thickness or void size) and \hat{q}_i is the predicted output.

\bar{q}_i is the mean of q_i . A value of R^2 close to 1.00 implies good prediction. R^2 can be distorted by a few large values of error in prediction due to the quadratic nature of the expression. Hence another measure of the accuracy of prediction, the mean error, is also reported. This quantity is calculated as follows:

$$E_i = |q_i - \hat{q}_i| \quad (8.5)$$

$$\bar{E} = \frac{\sum E_i}{n}$$

where the summation is over all the data points in the test data set.

Table 8.2 shows that while both Quadratic Regression and ANN are capable of accurately predicting the thickness, ANN does a much better job. Void size is more difficult to predict probably because of its nonlinear relationship with the independent variables. But here also ANN

does a much better job. The accuracy of the ANN predictions can be improved by varying the number of hidden layers and nodes. In this exercise we have used 7 input nodes , 1 hidden layer with 4 nodes and 2 output nodes corresponding to the two quality control variables. We have not attempted to optimize network configuration parameters. A more detailed study of the capabilities of ANN to model the void size is reported by Shieh et al. [67]. They showed that the ANN outperformed quadratic regression methods in terms of accuracy of prediction and robustness to measurement noise. For these reasons, we have chosen to use ANN models for the design of the control system.

8.1.3 On-Line ANN Models

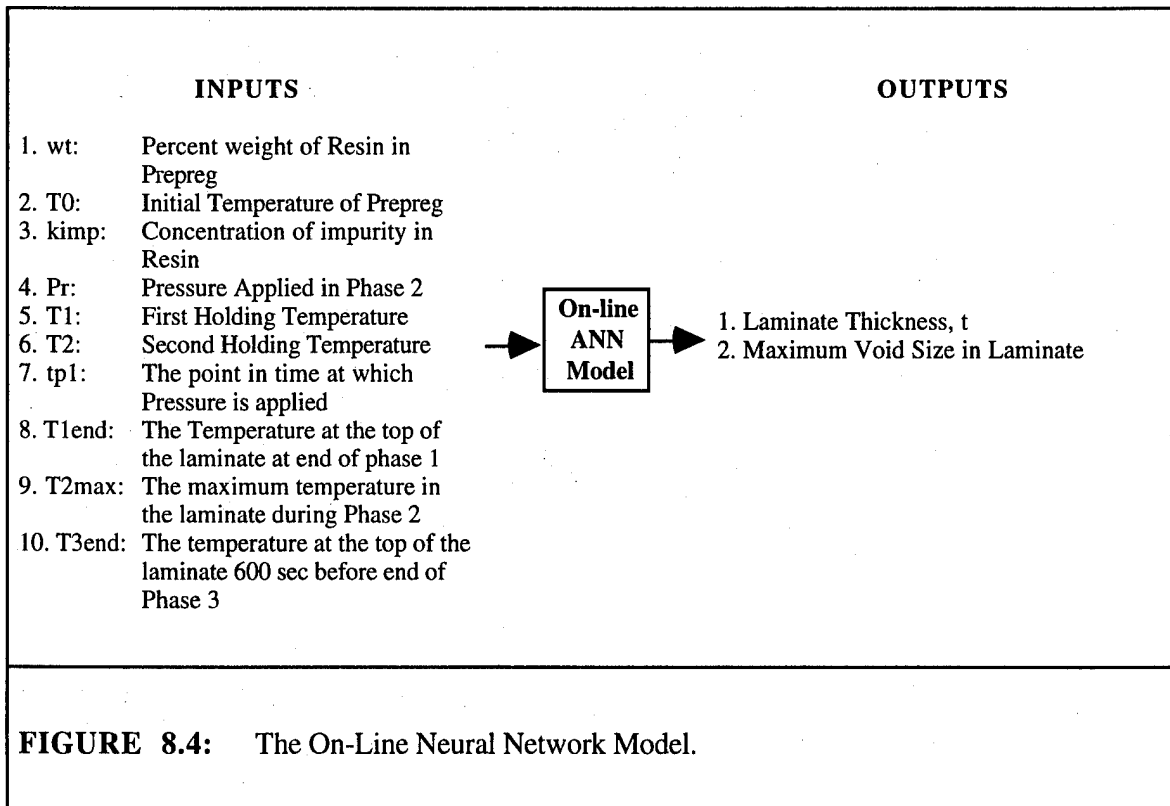
We now consider the problem of *unmeasured disturbances and modeling errors*. These two factors will introduce errors in the prediction of product quality and can adversely affect the performance of the control system. A strategy for partially overcoming this problem is presented next.

We want to take advantage of the fact that other on-line secondary measurements such as laminate temperature and pressure are generally available to monitor the status of the process. These measurements are influenced by any disturbances entering the process and hence can serve as indirect indicators of such unmonitored disturbances. Any deviations in these secondary measurements would indicate the presence of unmeasured disturbances and imply a change in final product quality as well. Through an analysis of past operating data and our understanding of the process itself, we can identify which of the secondary measurements are most useful in predicting the quality.

For the autoclave simulator such a study was conducted, and the following intermediate secondary measurements were found to be highly correlated with product thickness and void size:

- (i) T1end: the temperature at the top of the laminate at the end of phase 1 (see Figure 8.1) of the cure cycle.
- (ii) T2max: the maximum laminate temperature during phase 2 of the cure cycle.
- (iii) T3end: The temperature at the top of the laminate just before (~10 minutes) the end of phase 3.

An on-line ANN model was built by adding these three variables as additional input nodes to the network. This ANN model is schematically shown in Figure 8.4.



We have deliberately limited the choice of manipulated variables to the following set:

- (1) Pr: the applied pressure (y_1)
- (2) tp1: the time at which pressure is applied (y_2)
- (3) T1: the first hold temperature (y_3)
- (4) T2: the second hold temperature (y_4)

Although there are other possible defining parameters, such as the duration of each phase, which were not included in this study, these parameters were selected because they were most influential on the product quality.

There is one additional issue that must be addressed. Let us say that we start production of a new laminate in the autoclave. Some intermediate measurements which are used as inputs to the ANN model will not be available initially. So, in order to use this model, one must use estimated values. Such estimates may be taken from the last run made or one may use an average of the last few runs. In any case, use of such estimates will reduce the prediction accuracy.

As the batch progresses, more of these intermediate measurements will become available and hence, we will be able to make more accurate predictions of the product quality. Such revised estimates of the quality are used to provide on-line feedback correction to the cure cycle. Only some of the variables listed as manipulated inputs can be changed after the cycle has started. As the cycle progresses we will have better estimates of the quality, but fewer variables to manipulate.

The ANN model is obtained by regressing data from prior runs on the autoclave. For discussion here we will denote the ANN model as follows:

$$[th, Vs] = H(wt, T0, T1, T2, Pr, tp_1, T1_{end}, T2_{max}, Te_{end}) \quad (8.5)$$

where th is the thickness and Vs is the maximum void size in the laminate. In the implementation, H is stored as a vector of weights associated with a network.

8.1.4 Control Using ANN Models: Neurocontrol

In this section we present the architecture of a control system that uses the ANN model to predict and hence control the product quality by altering the cure cycle while the run is in progress. We call it on-line neurocontrol. It is based on the concepts of nonlinear model-based control described in Joseph et al. [68].

The control problem is broken up into four different sub problems, one for each phase of the cure cycle. At the start of the cycle, the control problem can be stated as follows:

Minimize $(th - 1.68 \text{ cm})^2$ by varying $T1, T2, Pr, tp1$

Subject to:

$$0 \leq Vx \leq 0.001 \text{ cm (Vs: void)}$$

$$0 \leq Pr \leq 6 \text{ atm}$$

$$2000 \leq tp1 \leq 6000 \text{ sec}$$

$$360 \leq T1 \leq 410 \text{ }^\circ\text{K}$$

$$420 \leq T2 \leq 460 \text{ }^\circ\text{K}$$

$$[th, Vs] = H(wt, kimp, T0, T1, T2, Pr, tp1, T1_{end}, T2_{max}, T3_{end})$$

Since $T1_{end}$, $T2_{max}$, and $T3_{end}$ are not yet available, we will use estimated values of these measurements in this phase of the cure cycle development. This problem was solved using a standard, off-the-shelf optimization package to determine the initial cure cycle. Figure 8.5 shows the schematic structure of the on-line neurocontroller. At the end of phase 1, a new measurement ($T1_{end}$) is available. One of the manipulated variables ($T1$) is already set and is hence removed as an independent variable from the problem definition. The optimization problem is then resolved to determine what, if any, changes are to be made in the previously computed cure cycle. A similar pattern is repeated at the end of each phase.

The algorithm may be stated as follows:

1. At the beginning of the cycle determine the optimum cure cycle to be followed by solving the above optimization problem.
2. At the end of each phase, use the actual measurements from the process to replace the estimated values as inputs to the ANN. Use this revised model and resolve the optimization problem to revise the optimum cure cycle. Use the updated cure cycle to start the next phase.
3. Repeat through all four phases of the cure cycle until the cure is completed.

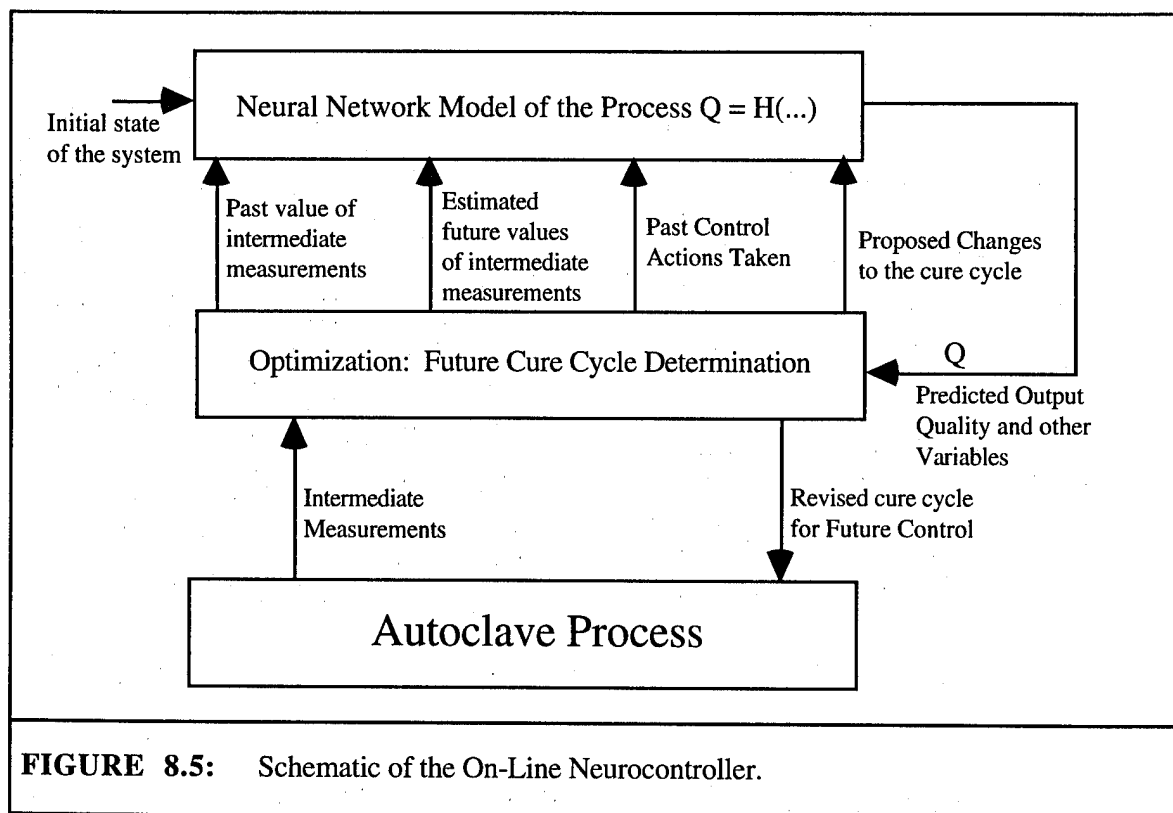


FIGURE 8.5: Schematic of the On-Line Neurocontroller.

8.1.5 Some Results

The current manufacturing procedure of the autoclave curing process is to follow a standard cure cycle, which does not take into account the different disturbances affecting each individual run. The neural network model takes into account some of the disturbances within the model. For example, the network model has the raw material properties as an input, so the neural network can predict the outcome when these properties change. However, the neural network model does not include every possible disturbance. In this section, performance of the neurocontroller will be discussed in situations with both measured and unmeasured disturbances.

The study was conducted as follows:

- (i) First the ANN model was trained using past operational data. The training set consisted of data from test runs made using the standard cure cycle. Details of the modeling results are given in a related publication by Shieh et al [67].
- (ii) New batches were simulated in two modes:
 - 1. Using a standard cure cycle
 - 2. Using a cure cycle that is determined by the on-line neurocontroller. In this case the cure cycle is modified in each phase of the batch operation as identified in Figure 8.1.

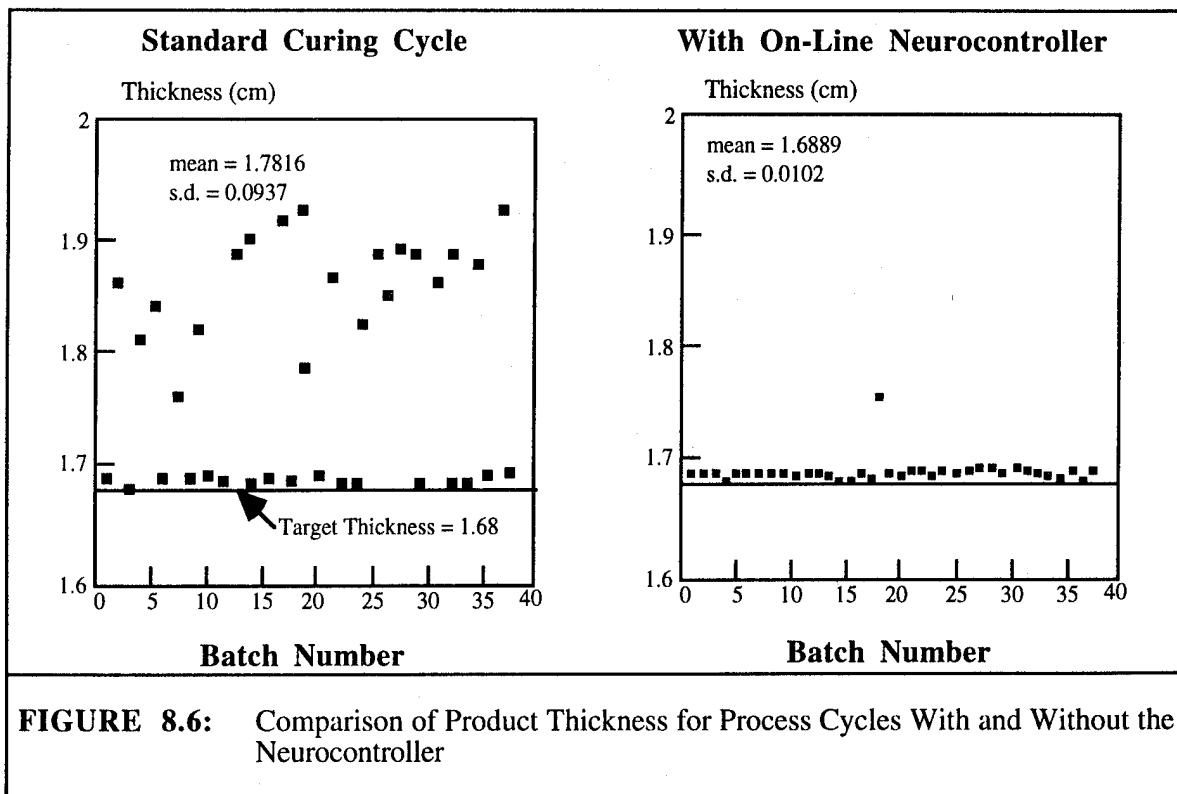
This study utilized a simulation model of the autoclave process as described in Wu and Joseph [64].

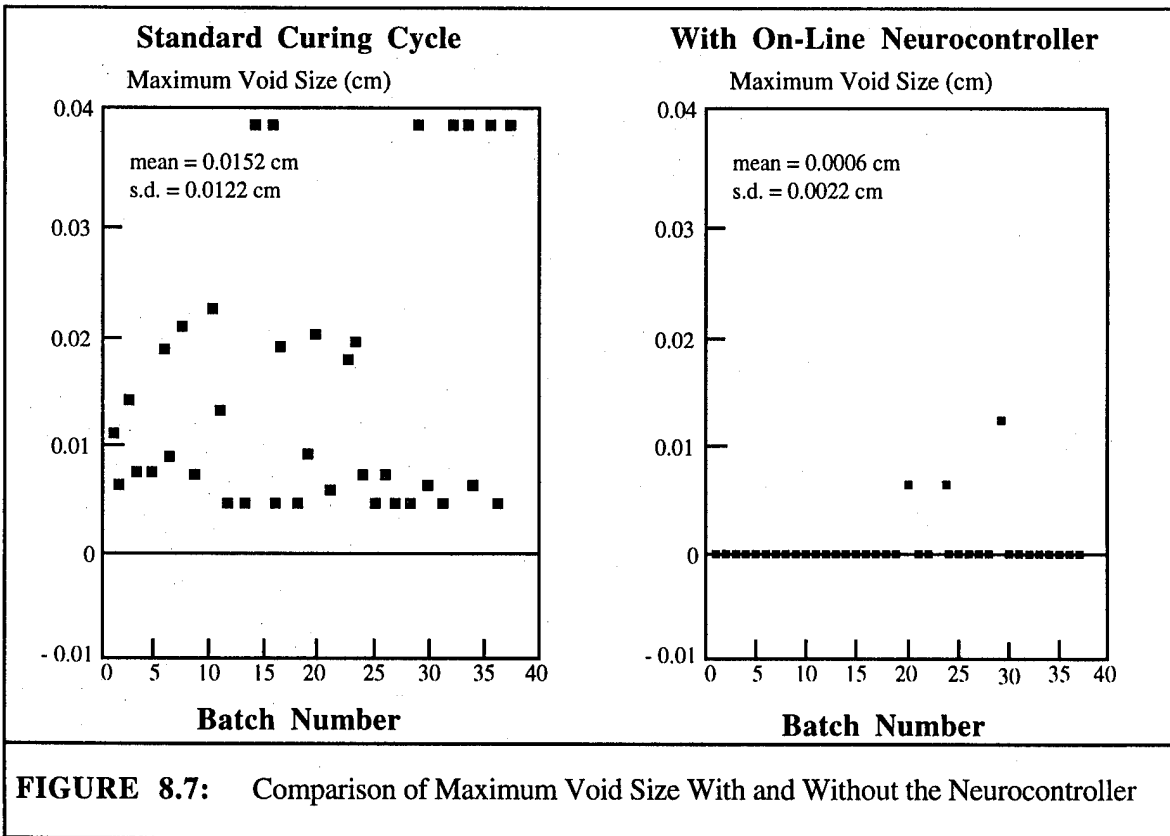
8.1.5.1 Performance with Measured Disturbances

The raw material (prepreg) properties may be affected by a number of elements including the age of the prepreg, the length of time the prepreg was exposed to the atmosphere, the humidity and temperature of the environment where the prepreg has been stored, etc. Therefore, the properties of the prepreg used in one batch run may differ significantly from those in the previous run, even though both prepregs come from the same supplier. According to the feature selection study conducted by Shieh [69], the three most influential prepreg properties are the resin weight percent (wt), the initial temperature (T_0) and the amount of impurity in the prepreg (kimp). The three property values are a part of the input to the neural network model, so they are called measured disturbances. To investigate the performance of the neurocontroller with the presence of measured

disturbances, 37 sets of raw material properties were generated. Each set contains three values, one for each of the three properties. Values for each property are randomly generated within the feasible range for that property. The 37 sets of raw material properties are used as 37 cases to evaluate the performance of the neuro-controller when applied to the simulated autoclave curing process. The performance of the neurocontroller is evaluated by how well it controls the quality of the cured composite laminate. The goal is to keep the thickness of the laminate at 1.68 cm, and the maximum void size in the laminate below 0.001 cm in diameter. The results are shown in Figures 8.6 and 8.7. Figure 8.6 shows a comparison of the product thickness distribution using the standard cure cycle and the on-line neurocontroller. Each point represents the resulting laminate thickness for one set of the raw material properties. The mean and standard deviation of the product thickness for the 37 cases are also reported on the figure for both cases. Figure 8.7 shows a similar comparison for the maximum void size distribution.

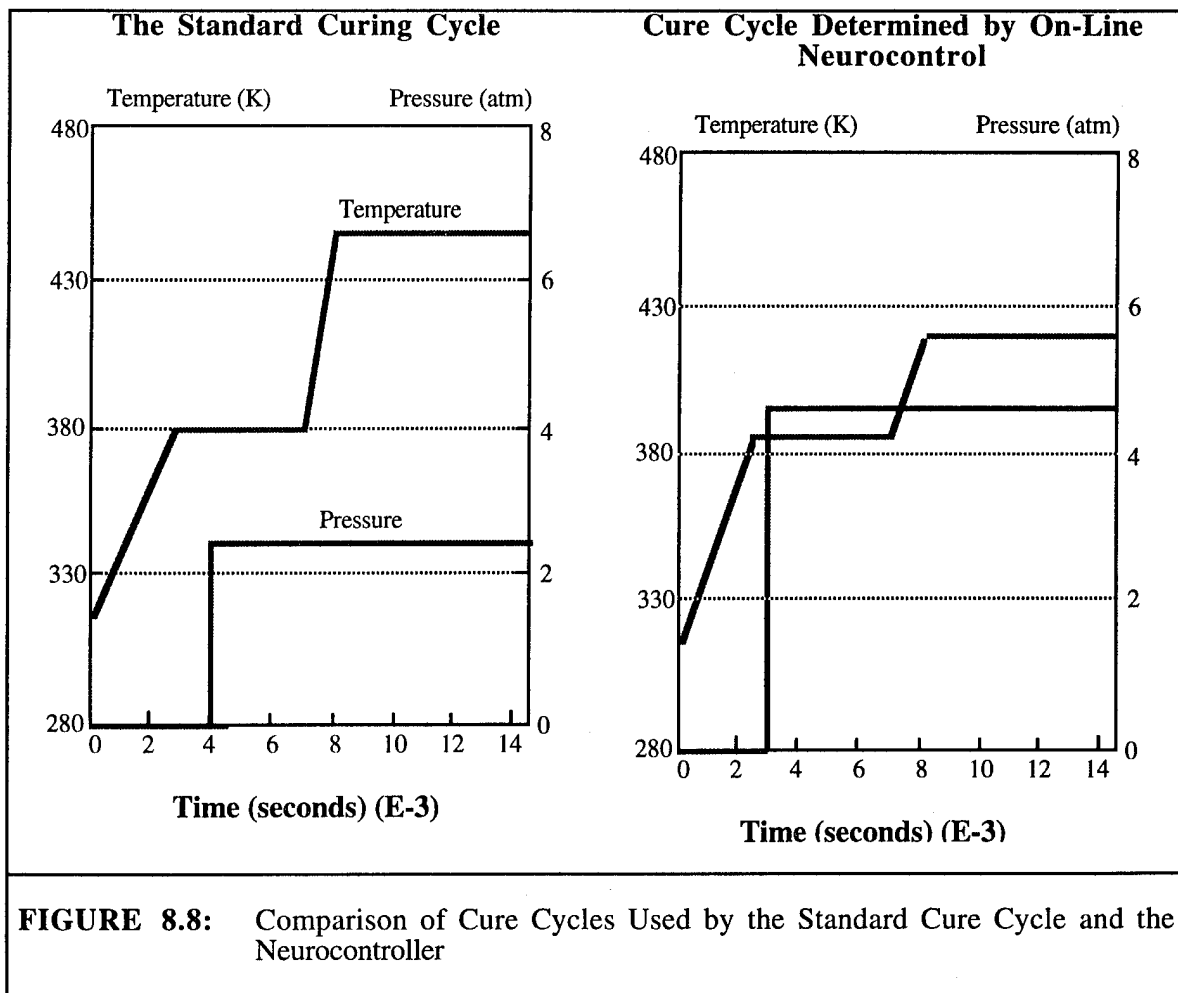
It can be seen from Figure 8.6 that the laminate thickness obtained by using the standard cure cycle can deviate significantly from the target value. The on-line neurocontroller can greatly reduce the deviation. It is interesting to note that the only point which differs significantly from the target value in the graph with the on-line neurocontroller is the thickness for Case 18. This thickness also deviates significantly from the target value with the standard cure cycle. This suggests that with this case of raw material properties, the conditions required to maintain the product thickness are significantly different from those used to obtain the model. Figure 8.7 shows that the maximum void size in the laminate cured by the standard cure cycle can also deviate significantly from the target value. The on-line neurocontroller reduces the deviation significantly.





The error in thickness is always positive because the set point for the thickness is set close to the lowest possible value for this laminate (reached when the fibers are compacted to the point of touching each other). Thus, all disturbances tended to give product thicknesses greater than the set point.

Figure 8.8 shows a comparison of the standard cure cycle and the cycles determined by the neurocontroller for Case 16. The thickness and maximum void size values obtained from these cure cycles are also reported therein. The on-line neurocontroller lowers the two properties by applying a higher pressure earlier during the process and by significantly lowering the cure temperatures used.



8.1.5.2 Performance in the Presence of Unmeasured Disturbances

In addition to the measured disturbances mentioned in the last subsection, there are other disturbances that may also affect the autoclave curing process. These include raw material properties that are not taken into account in the models (for example, resin/curing agent ratio), failed or inaccurate sensors, error in the adjustment of the manipulated variable, heat loss to the environment, etc. These disturbances are not considered in the neural network models, so they are called unmeasured disturbances. The performance of the neurocontroller was investigated in the presence of one type of unmeasured disturbance - additional heat input to the process. This was done by increasing the actual heating rate used by a fixed percentage during the two heating phases of the cure cycle. Two levels of disturbances were considered, but results for only one level are shown here. In the operation of a real process, the additional heat input can be caused by a malfunction of the heating elements or a change in the heat of reaction of the resin used. Ten of the

37 cases of the raw material properties generated above were used to evaluate the performance of the neurocontroller with the presence of additional heat input. The performance was evaluated by how well the controller controls the quality of the product. The goal was again to keep the thickness of the laminate at 1.68 cm, and the maximum void size in the laminate at zero.

Figure 8.9 shows a comparison of the maximum void size distribution for the two different control systems. The product quality obtained by using the standard cure cycle deviates very significantly from the target values when the process is subjected to 20% additional heat input as described above. However, with the on-line neurocontroller, the deviation is greatly reduced. Improvement occurs because the on-line neurocontroller issues new cure cycles throughout each run. A new cycle is issued whenever an intermediate measurement, which reflects the current state of the process, is obtained. Therefore, the neurocontroller can detect any deviation from the desired process state, and take corrective actions immediately.

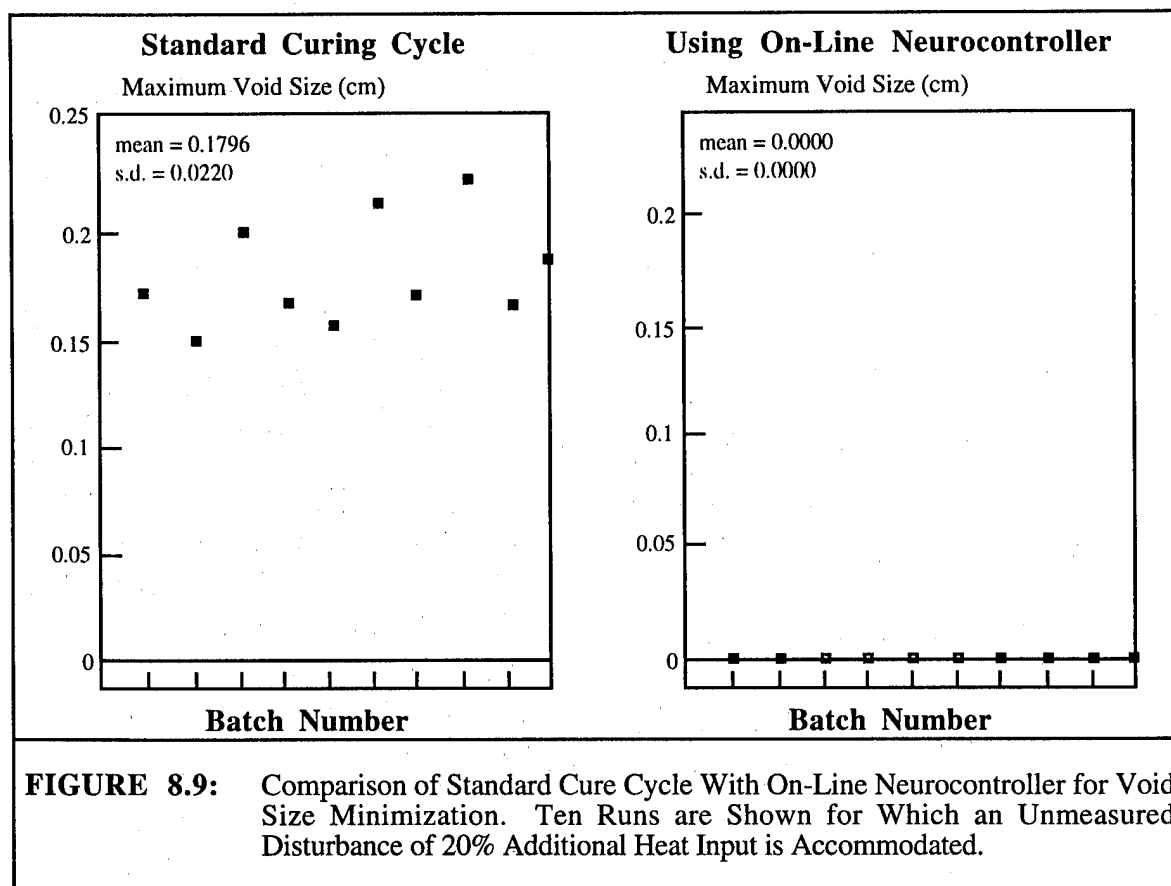
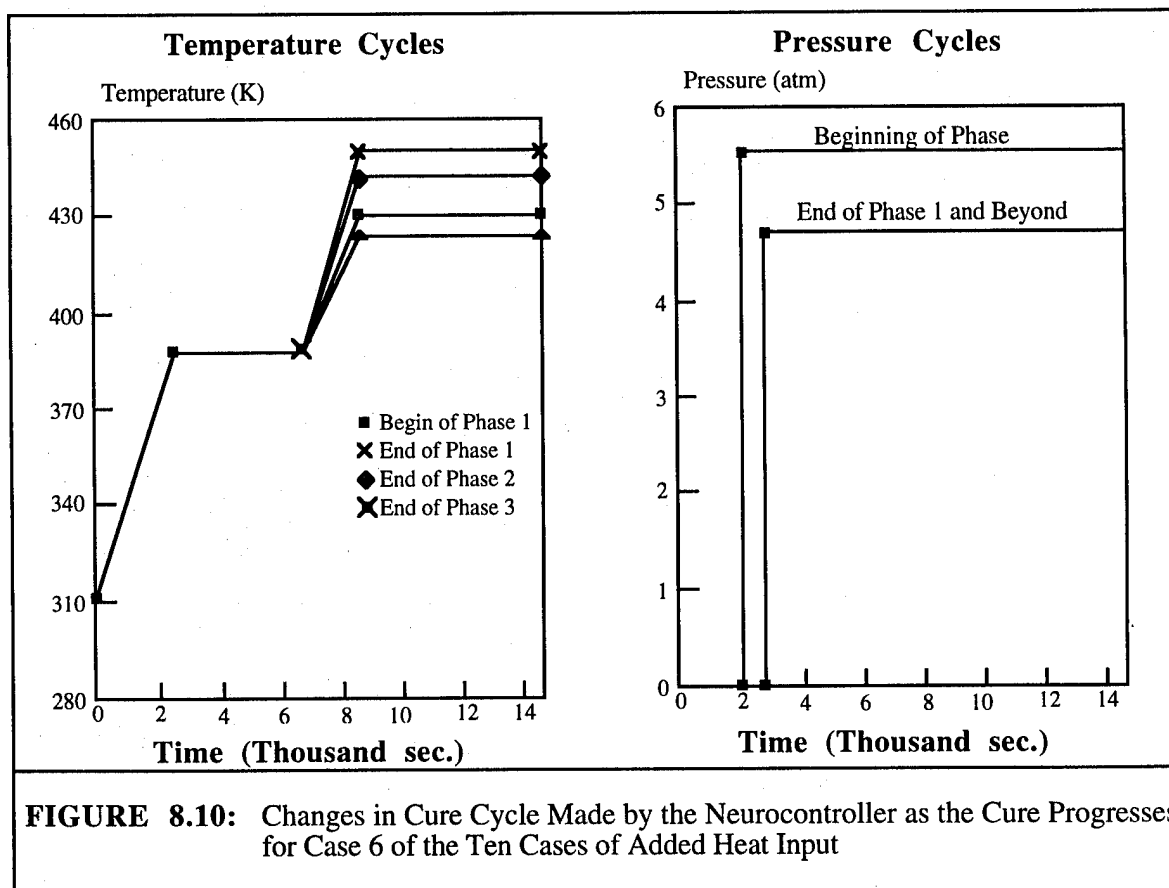


Figure 8.10 shows a series of cure cycles issued by the on-line neurocontroller for Case 6, when it is subjected to 20% additional heat input. It is used as an example to show that the on-line neurocontroller revises the cure strategy at the end of each phase using newly available data. The new optimal cycle may or may not be the same as the one issued previously. In Figure 8.10, the cycle issued at the end of Phase 1 reflects the changes introduced after T_{1end} became available, the cycle issued at the end of Phase 2 reflects the availability of T_{2max} , and the cycle issued at the end of Phase 3 follows the availability of T_{3end} . Here, T_{1end} , T_{2max} and T_{3end} are intermediate measurements. In this example, the optimal cure cycles do change significantly throughout the run as a result of the intermediate measurements.

It can be seen that at the beginning of the run, the issued cure cycle is not much different from the standard cure cycle. However, the cure cycle issued at the end of Phase 1 suggests a much higher autoclave pressure being applied earlier during the run. The changes are issued because the neurocontroller detects a higher than expected process temperature from the available intermediate measurement, so it takes actions to cope with this situation. If the laminate temperature at the end of Phase 1 is higher than expected, the minimum resin viscosity will occur earlier during the run. Therefore, it is reasonable to apply a higher pressure at an earlier time to control the thickness and to keep the void size small. The cure cycle issued at the end of Phase 2 and Phase 3 suggests a lower second holding temperature.

The results show that the on-line neurocontroller can handle both types of disturbances very well. As mentioned earlier, the neurocontroller is activated throughout a run whenever new intermediate measurements are obtained. The intermediate measurements reflect the current state of the process, so the controller can detect any deviation and take corrective actions. These measurements need to be selected carefully so that they correctly represent the process state. In this application, the feature selection conducted by Shieh [69] was used to select the influential raw material properties. Other techniques that may help preprocess the operational data include principal component analysis and canonical analysis.



9.0 SUMMARY AND CONCLUSIONS

The processing of composites containing condensation polyimide resins is difficult because of the complex chemistry and the volatile materials which must be removed during processing. AFR-700B is a newly formulated, high temperature polyimide resin having the advantages of a high glass transition temperature (750°F) and superior thermo-oxidative stability, but the disadvantage of the volatile management problem. Successful, cost-effective processing of AFR-700B composite parts will be greatly aided by proper process simulation models, adequate sensing technology, and new concepts in process control. This study explored all three of these areas in an effort to advance the state of processing science and engineering of composite materials.

A model describing the devolatilization of polyimide composites was generalized and expanded to accommodate additional condensation polyimide systems like AFR-700B. Because of a lack of fundamental data on the AFR-700B system, critical model inputs for the kinetics, mass transfer coefficient, and gas phase permeability were determined.

The devolatilization model has been experimentally verified by comparing its predictions for pressure and temperature distributions through the laminate thickness with experimentally measured pressure and temperature profiles. Good agreement between model predictions and experimental measurements was obtained. As an example, agreement within 1-2°C with experimental temperature profiles and within 3-5 Torr with experimental pressure profiles was obtained for a 15-ply laminate heated at 1°C/min heating rate under a pressure of 20 Torr. The pressure profiles shift upward to higher values with higher heating rates and thicker laminates. The temperature difference between the tool surface and bleeder side of the laminate increases with heating rate and laminate thickness.

The verified model was also used to successfully predict changes in concentration of the volatile species in the resin and their rate of removal via gas phase evacuation during the composite cure for several heating rates and vacuum bag pressures.

The change in resin morphology during the polyimidization reaction and the phenomenon of volatile evolution were examined with thermal analysis methods and optical microscopy. Both indicate that AFR-700B polyimide resin does not crystallize during processing and that devolatilization proceeds in two parts and is markedly influenced by processing conditions.

Model simulations, together with dynamic dielectric measurements, were used to study the polyimidization (polycondensation) reaction and accompanying devolatilization process for unidirectional AFR-700B/S-2 glass laminates. Comparison of measured dielectric ionic viscosity and devolatilization model predictions for instantaneous mass fluxes of volatiles during the processing cycle shows that microdielectrometry can indicate: a) the start of the polycondensation reaction (minimum ionic viscosity of prepreg resin), b) the temperature-time window in which maximum devolatilization occurs and bubbles are developed between laminate plies (momentary retardation in the ionic viscosity rise and inflection point on the ionic viscosity curve), c) the end of the polycondensation reaction (decrease in ionic viscosity), and d) the effects of water absorbed during freezer storage on the polyimidization reaction and devolatilization process.

In an effort to complement the QPA study under this contract, we also examined the potential for on-line feedback control using neural network models. The ANN models proved superior to classical quadratic regression approaches in capturing the non-linear relationship that exists between the product quality and processing variables. Intermediate secondary measurements, taken while the cure cycle is in progress, can be used to detect unmeasured disturbances and hence provide some feedback correction to the on-line model used. Models without this feedback compensation proved to be inferior in the control studies performed.

The ANN models require good training data covering the broad range of expected operating conditions. The existing database of past operational history of an autoclave can be used as a source for this input. However, care should be exercised to ensure that the data is rich enough to reflect the effect of all manipulated control inputs on the product quality. If a more complex, off-line model is available, this can also serve as a means of producing data for training the neural network. Since the AFR-700B data base was not sufficient and since the model was sufficiently verified only toward the end of the study, we utilized a proven model for autoclave processing of carbon/epoxy systems to demonstrate the concept. The methodology for on-line, model based control presented here can be generalized to other batch manufacturing operations and particularly to the AFR-700B system.

10.0 ACKNOWLEDGEMENT

The model-generated data base for the carbon/epoxy system used to demonstrate the ANN control methodology was developed under NSF grant DDM-9123861 from the Division of Design and Manufacturing Systems.

11.0 REFERENCES

1. J. L. Kardos, "Reactive Processing of Composite Materials - Some Pitfalls and Prognostications," Extended Abstract, Proceedings of the European Regional Meeting of the Polymer Processing Society, Palermo, (Sept. 15-18), (1991), p. 21.
2. T. T. Serafini, P. G. Cheng, K. K. Ueda, and W. F. Wright, "Highly Processable 371°C (700°F) Polyimides," Presented at the 22nd Inter. SAMPE Tech. Conference, Boston, MA, (1990).
3. C. A. Pryde, "IR Studies of Polyimides. I. Effects of Chemical and Physical Changes During Cure," Journal of Polymer Science, 27,711 (1989).
4. J. C. Johnston, M. B. Meador and W. B. Alston, "A Mechanistic Study of Polyimide Formation from Diester-Diacids," Journal of Polymer Science, 25, 2175 (1987).
5. D. Garcia, T. T. Serafini, "FTIR Studies of PMR-15 Polyimides," Journal of Polymer Science, 25, 2275 (1987).
6. P. H. Young, A. C. Chang, "Polyimide Analysis Using Reflectance-FTIR," SAMPE Journal, 3, 70 (1986).
7. J. N. Hay, J. D. Boyle, P. G. James and J. R. Walton, "Polymerization Mechanism in PMR-15 Polyimide," Proceedings of the Third Inter. Conf. on Polyimides, Ellenville, New York, November, (1988), p. 305.
8. S. P. Parker, "The Application of Vibrational Spectroscopy to the Study of Polyimides and Their Composites," Vibrational Spectroscopy, 3, 87 (1992).
9. P. J. Dynes, T. T. Liao, C. L. Hammermesh and E. F. Witucki, "The Cure Rheology of PMR Polyimide Resins," Polyimides Synthesis, Characterization, and Application, Vol. 1, K. L. Mittal, Ed., Plenum Press, New York, (1984), p. 311.
10. R. W. Lauver, "Kinetics of Imidiation and Crosslinking in PMR Polyimide Resin," Journal of Polymer Science, 17, 2529 (1979).
11. M. Kantz, "Processing of PMR-15 Prepregs for High Temperature Composites," Plastics Engineering, 1, 29 (1990).

12. P. J. Dynes, R. M. Panos, "Investigation of the Crosslinking Efficiency of Some Additional Curing Polyimides," Journal of Applied Polymer Science, **25**, 1059 (1980).
13. J. N. Hay, J. D. Boyle, and S. F. Parker, "Polymerization of *N*-phenyldiamine: A Model for the Crosslinking of PMR-15 Polyimide," Polymer, **30**, 1037 (1989).
14. F. L. Abrams, "Developing a Cure Strategy for AFR-700B Composites," Presented at the 1st AFR-700B Symposium, Fairborn, OH (1991).
15. S. K. Ferer, A. Castro, and W. A. Price, "Advanced Material Processing Control," Air Force Contract No. F33615-91-C-5615, 3rd Quarterly Technical Report, Materials Directorate, Wright-Patterson AFB, 1 April - 1 July (1992).
16. B. P. Rice, "Postcure Study of AFR-700BB Neat Resin," Presented at the 1st AFR-700B Symposium, Fairborn, OH (1991).
17. R. Dave, J. L. Kardos, and M. P. Dudukovic, "A Model for Resin Flow During Composite Processing: Part 1 - General Mathematical Development," Polymer Composites, **8**, 29 (1987).
18. R. Dave, J. L. Kardos, and M. P. Dudukovic, "A Model for Resin Flow During Composite Processing: Part 2 - Numerical Analysis for Unidirectional Graphite/Epoxy Laminates," Polymer Composites, **8**, 123 (1987).
19. I. S. Yoon, "Experimental Verification of Simulation Models for the Processing of Condensation Polyimide Thermoplastic Composites," D. Sc. Thesis, Department of Chemical Engineering, Washington University, May(1990).
20. J. L. Kardos, Y. Yang, I. S. Yoon, and M. D. Dudukovic, "Processing Science of Thermoplastic Composites: Condensation Reaction Void Modeling," Air Force Contract No. F 33615-85-C-5046, Final Technical Report, December (1988).
21. S. Whitaker, "Simultaneous Heat, Mass and Momentum Transfer in Porous Media: A Theory of Drying," *Advances in Heat Transfer*, vol. 13, Academic Press, New York, 119 (1977).
22. J. L. Kardos, M. P. Dudukovic, Yubo Yang and I. S. Yoon, "Part II: Condensation Research Void Modeling," *Processing Science of Thermoplastic Composites*, J. E. Kurz

and J. L. Kardos, Air Force Contract No. F33615-85-C-5046, Final Technical Report, Air Force Materials Laboratory, Wright-Patterson AFB, 1 January 1987–31 December 1989.

23. D. Kranbuehl, T. Prettyman, K. Robillard, J. Smith, A. Nicoletti and S. Hart, "Characterization of and Sensor - Model Verification and Control of the Properties of PMR-15 During Processing," Proceedings of the Inter. SAMPE Symp., (April 1991), p. 1161.
24. R. B. Prime, "Thermosets," Thermal Characterization of Polymeric Materials, E. A. Turi, Ed., Academic Press, New York, (1981), p. 435.
25. J. A. Thomas, T. J. Golab, B. D. West and J. L. Kardos, "Advanced Composite Processing Technology Development. Part II: Control of Condensation Polyimide Processing," Air Force Contract No. F33615-88-C-5455, Eleventh Quarterly Interim Technical Report, WRDC/ML, Wright-Patterson AFB, OH 45433, Nov. 1991.
26. D. Kranbuehl, D. Eichinger, D. Rice, A. Williamson, R. Clark, T. Prettyman, A. Loos and J. Koury, "In Situ Measurement, Modeling and Control of the Imidization Reaction in PMR-15," Proceedings of the Inter. SAMPE Symp., April, (1990), p. 123.
27. N. Navarre, "Polyimide Thermal Analysis" in Polyimides Synthesis, Characterization, and Application, Vol. 1, K. L. Mittal, Ed., Plenum Press, New York, (1984), p. 429.
28. C. Johnson, J. Mao and S. L. Wunder, "FT-Raman Spectroscopy of the Curing Reactions of Polyimides," Proceedings of the Third Inter. Conf. on Polyimides, Ellenville, New York, November, (1988), p. 347.
29. P. D. Frayer, "The Interplay Between Solvent Loss and Thermal Cyclization in LARC-TPI," Polyimides Synthesis, Characterization, and Application, Vol. 1, K. L. Mittal, Ed., Plenum Press, New York, (1984), p. 273.
30. D. H. Kim, S. C. Kim, "Phase Separation Behavior of the Epoxy-CTBN Mixture During the Curing Process," Polymer Engineering and Science, 5, 289 (1991).
31. D. W. Van Krevelen, P. J. Hoftyzer, "Properties of Polymers-Correlations with Chemical Structure," American Elsevier Publishing Company, Inc., New York, (1972), p. 327.
32. J. L. Kardos, B. D. West, "Part II: Control of Condensation Polyimide Curing Processing" in "Advanced Composite Processing Technology Development," Air Force Contract No.

- 33615-88-C-5455, 14-th Quarterly Technical Report, Materials Laboratory, Wright-Patterson AFB, 1 May - 31 July (1992).
33. J. A. Biesenberger, D. H. Sebastian, "*Polymer Devolatilization*," Principles of Polymerization Engineering, John Wiley & Sons, New York, (1983), p. 573.
 34. J. L. Kardos, B. D. West, "*Part II: Control of Condensation Polyimide Curing Processing*," "*Advanced Composite Processing Technology Development*," Air Force Contract No. 33615-88-C-5455, 16-th Quarterly Technical Report, Materials Laboratory, Wright-Patterson AFB, 1 February - 30 April (1993).
 35. J. Dwyer, "*Structural Composite Materials*," Presented at the 1st AFR-700B Symposium, Fairborn, OH (1991).
 36. J. A. Kreuz, A. L. Endrey, F. P. Gay and C. E. Sroog, "*Studies of Thermal Cyclization of Polyamic Acids and Tertiary Amine Salts*," Journal of Polymer Science, **4**, 2607 (1966).
 37. N. A. Androva, M. I. Bessonov, L. A. Laius and A. P. Rudakov, "*Synthesis and Conversion of Polyimides*," Polyimides: A New Class of Thermally Stable Polymers, M. M. Koton. Ed., Technomic Publishing Co., Stamford, (1970). p. 1.
 38. L. A. Laius, M. I. Tsapovetsky, "*Kinetics and Mechanism of Thermal Cyclization of Polyamic Acids*," Polyimides Synthesis, Characterization, and Application, Vol. 1, K. L. Mittal. Ed., Plenum Press, New York, (1984), p. 295.
 39. M. I. Bessonov, M. M. Koton, V. V. Kudryavtsev and L. A. Laius, "*Synthesis and Chemical Structure of Polyimides*," Polyimides: Thermally Stable Polymers, M. M. Koton, Ed., Consultants Bureau, New York, (1987), p. 1.
 40. S. Numata, K. Fujisaki and N. Kinjo, "*Studies on Thermal Cyclization of Polyamic Acids*," in Polyimides Synthesis, Characterization, and Application, Vol. 1, K. L. Mittal, Ed., Plenum Press, New York, (1984), p. 259.
 41. C. E. Diener, J. R. Susko, "*Etching of Partially Cured Polyimide*," Polyimides Synthesis, Characterization, and Application, Vol. 1, K. L. Mittal, Ed., Plenum Press, New York, (1984), p. 353.
 42. A. I. Baise, "*Optimizing Polyimide Cure Using Infrared Spectroscopy and a Factorial Design*," Journal of Applied Polymer Science, **32**, 4043 (1986).

43. C. Feger, "Curing of Polyimides," Polymer Engineering and Science, **5**, 347 (1989).
44. J. L. Kardos, M. P. Dudukovic, and R. Dave, *Advances in Polymer Science*, 80: Epoxy Resin and Composites, Part IV, Ed. K. Dusek, Springer Verlag, Berlin, (1986), p. 101.
45. R. Dave, J. L. Kardos and M. P. Dudukovic, "Process Modeling of Thermosetting Matrix Composites: A Guide for Autoclave Cure Cycle Selection," Proceedings of the American Society for Composites, First Tech. Conf., Dayton, Ohio, October 7, (1986), p. 137.
46. P. D Aldrich, S. K. Thurow, M. J. McKennon and M. E. Lyssy, "Dielectric Relaxation Due to Absorbed Water in Various Thermosets," Polymer, **12**, 2289 (1987).
47. A. R. Blythe, "Electrical Properties of Polymers," Cambridge University Press, Cambridge, UK (1979), p. 130.
48. H. J. Neuhaus, G. B. Hershokowitz and S. D. Senturia, "Conduction Transient in Polyimide: Effect of Sodium Ions and Water," Proceedings of the Third Inter. Conf. on Polyimides, Ellenville, New York, (1988), p. 529.
49. G. D. Roberts, R. W. Lauver, "Quantitative Analysis of PMR-15 Polyimide Resin by HPLC," Journal of Applied Polymer Science, **33**, 2893 (1987).
50. D. Wilson, "PMR-15 Processing, Properties and Problems – A Review," British Polymer Journal, **5**, 405 (1988).
51. D. E. Kranbuehl, S. E. Delos, E. C. Yi and J. T. Mayer, "Dynamic Dielectric Analysis of the Cure Chemistry of PMR-15," Proceedings of Second Inter. Conf. on Polyimides, Ellenville, New York, October, (1985), p. 469.
52. S. M. Hart, D. E. Kranbuehl, A. Loos, B. Hinds, J. Koury and J. Harvey, "FDEMS/QPALS Intelligent Automated Cure Processing of PMR-15," Proceedings of the 38th Inter. SAMPE Symp., May, (1993), p. 1009.
53. S. K. Ferer, "Advanced Material Processing Control," Air Force Contract No. F33615-91-C-5615, 6-th Quarterly Technical Report, Materials Directorate, Wright-Patterson AFB, 1 January - 1 April (1993).
54. S. K. Ferer, "Advanced Material Processing Control," Air Force Contract No. F33615-91-C-5615, 8-th Quarterly Technical Report, Materials Directorate, Wright-Patterson AFB, 1 July - 1 October (1993).

55. S. K. Ferer, "*Advanced Material Processing Control*," Air Force Contract No. F33615-91-C-5615, 7-th Quarterly Technical Report, Materials Directorate, Wright-Patterson AFB, 1 April - 1 July (1993).
56. A. C. Loos, and G. S. Springer, "*Curing of Epoxy Matrix Composites*," J. of Com. Matls., 17, 135 (1983).
57. J. L. Kardos, M. P. Dudukovic, R. Dave, "*Void Growth and Resin Transport During Processing of Thermosetting Matrix Composites*," Dusek, K. Ed., *Advances in Polymer Science*, 80, 101 (1986).
58. T. E. Saliba, R. A. Servais, J. A. Snide, and C. W. Lee, "*Modeling of the Cure Process of Advanced Composites*," *Advanced Composites Conference Proceedings*, American Society for Metals, 1985.
59. J. E. Sumerak and J. D. Martin, "*Applying Internal Temperature Measurement Data to Pultrusion Process Control*," 41st Annual Conference, Reinforced Plastics/Composites Institute, The Society of Plastics Industry, Inc., Jan. 27-31, 1986.
60. R. A. Servais, C. W. Lee, and C. E. Browning, "*Intelligent Processing of Composite Materials*," SAMPE J., Sep./Oct., 14, 1986.
61. C. W. Lee, "*Composite Cure Process Control By Expert Systems*," *Proceedings of the First Conference on Composite Materials of American Society for Composites*, Dayton, OH, Oct. 7-9, 1986, p. 187.
62. R. W. Roberts, "*Automated Composites Cure Control Implementation: A Cure Modeling Approach to Automation*," 32nd International SAMPE Symposium, April 6-9, 1987 p. 298.
63. S. LeClair, T. Lagnese, and F. Abrams, "*Qualitative Process Automation for Autoclave Curing of Composites*," Report No. AFWAL-TR-87-4083, Wright Patterson Air Force Base, Dayton, OH, 1987.
64. H. T. Wu, and B. Joseph, "*Model Based Control of Autoclave Curing of Composites*," SAMPE J., 26, 6, 39 (1990).

65. D. E. Rumelhart, J. L. McClelland, and the PDP Research Group, . Parallel Distributed Processing- Explorations in the Microstructure of Cognition, Vol 1: Foundations, The MIT Press, Cambridge, MA, 1986.
66. Wu, H. T., "*Knowledge Based Control of Composite Material Manufacturing Processes*," D. Sc. Thesis, Washington University, 1990.
67. D. Shieh, F. Wang, B. Joseph, "*Exploratory Data Analysis: A Comparison of Statistical Methods with Artificial Neural Networks*," Comp. And Chem. Engg. J., 16(4), 413, (1992).
68. B. Joseph, S. S. Jang, and H. Mukai, "*On-line Optimization of Constrained Multivariable Non-linear Processes*," AIChE J., 33, 26 (1987).
69. D. Shieh, "*Knowledge Acquisition From Routine Data*", D.Sc. Thesis, Washington University, St. Louis, MO, 1992.

12. APPENDIX: MODEL INPUT FILE

0.	<< Mesh Contour: 0; normal, 0.1; left, 0.9; right>>
0.0	<< Initial Time, min>>
0.0	<< Initial Time of Output, min>>
1.d-7	<< Time Interval for Calculation, min>>
0.1	<< Laminate Thickness; cm>>
25.	<< Initial Temperature; C>>
1	<< Cure Cycle Unit Number>>
100. 225. 0	<< Heating Time, Shoulder Temp., Holding Time>>
5.0	<< Time Step of Output; min>>
0.01 0.555 0.435	<< Volume Fraction of Gas, Liquid, Solid Phase>>
0.00 0.094 0.00	<< Initial Weight Fractions of Water, MeOH, IPA>>
1.D-5 1.D-4 1.D-5	<< Non-0 Initial Gas Mol. Frac.; Water, MeOH, IPA>>
0.02632	<< Initial Vacuum; atm>>
25.	<< Temperature when Vacuum is Applied; C>>
1.0	<< Full Vacuum/Initial Vacuum>>
1.0	<< Time when Full Vacuum is Achieved; min>>
2.79D-4	<< Heat Transfer Coeff.; J/cm ² .s.K >>
1.1D-5	<< Gas Phase Permeability; dyne/atm >>
1.6D-4	<< Mass Transfer Constant fk; g/cm ³ /atm/s >>
350.	<< Tmaxcc when Mass Transfer is Maximum; C>>
1.4 0.02	<< Mass Transfer Constants; m, d >>
2.52	<< Density of Glass Fiber; g/cm ³ >>
0.7	<< Heat Capacity of Glass Fiber; J/g K >>
0.13	<< Thermal Conduc. of Glass Fiber; J/cm s K >>
1.29D11 12960. 1.3	<< DSC Kinetic Parameters; k'o (1/sec), E/R (K), n >>
647.3 512.6 508.3	<< Critical Temp.; K >>
373. 337.8 355.4	<< Boiling Temp.; K >>
217.6 79.9 47.	<< Critical Pressure; atm >>
4.06D4 3.52D4 3.985D4	<< Coeff. of Heat Evaporation; atm >>
18.3036 3816.44 -46.13	<< Coeff. of Vapor Press. of Water >>
18.5875 3626.55 -34.29	<< Coeff. of Vapor Press. of MeOH >>
18.6929 3640.20 -53.54	<< Coeff. of Vapor Press. of IPA >>
7.70 4.59D-4 2.5D-6 -0.86D-9	<< Cp Coeff. of Water Gas >>
5.05 1.7D-2 6.18D-6 -6.81D-9	<< Cp Coeff. of MeOH Gas >>
7.745 4.5D-2 1.53D-5 -2.212D-8	<< Cp Coeff. of IPA Gas >>
1.75D-5 -2.4D-8 4.3D-10 -2.17D-13	<< Keff Coeff. of Water Gas >>
0.75D-5 -2.4D-8 4.3D-10 -2.17D-13	<< Keff Coeff. of MeOH Gas >>
0.75D-5 -2.4D-8 4.3D-10 -2.17D-13	<< Keff Coeff. of IPA Gas >>
18.32. 60.1 108. 508. 616.	<< Molecular Weight of 1,2,...6; g/mol >>
0.988 0.791 0.786 1.254 1.254 1.31	<< Liquid Density; g/cm ³ >>
5.0 3.064 3.26 2.28 1.735 1.8	<< Cp of Liquid Components; J/g K >>
23.5 14.3 11.5 14.5 14.5 14.5	<< Sol. Parameters of Liq. sq(cal/cm ³) >>
1.36D-3	<< Ther. Cond. of Liquid Mixture; J.cm s K >>
0.0	<< Heat of Reaction; J/mole >>